Dissertation
submitted to the
Combined Faculties of the Natural Sciences and Mathematics
of the Ruperto-Carola University of Heidelberg, Germany
for the degree of
Doctor of Natural Sciences

Put forward by
Armelle Jardin-Blicq
Born in Poissy, France
Oral examination: 12 june 2019

The TeV γ-ray emission of the Galactic Plane

HAWC and H.E.S.S. observations of the Galactic Plane and detailed study of the region surrounding 2HWC J1928+177

Referees : Prof. Dr. Jim Hinton

Prof. Dr. Stefan Wagner

Abstract

TeV γ-ray astronomy is led by two main ground-based facilities: Imaging Atmospheric Cherenkov Telescopes, and Water Cherenkov Detectors. This thesis focuses on H.E.S.S., an array of five Cherenkov telescopes, and HAWC, a wide field of view γ-ray observatory, that are very complementary despite their technical differences.

Part of this thesis is dedicated to the HAWC high energy upgrade with the outrigger array that was developed and deployed in the time frame of this Ph.D. I introduce the calibration for the charge and time reconstruction of the photomultiplier tubes that equip each of the small outrigger tanks.

I present a comparison of the galactic plane as seen by HAWC and H.E.S.S. in the region where they overlap. I highlight the differences which arise from intrinsic properties of the instruments and from their dedicated data analysis, and show that background estimation is a major ingredient. The region of the galactic plane around the source 2HWC J1928+177 is studied in more details. A multi-component fit is performed and the best fit model includes two point sources for 2HWC J1930+188 and the new source HWC J1932+192, one extended source of size $\sigma = 0.17°$ for 2HWC J1928+177 and 2 extra extended sources that account for larger scale emission.

Zusammenfassung

In der TeV Gamma-Astronomie gibt es zwei führende bodengebundenen Techniken: Imaging Atmospheric Cherenkov Teleskope und Water Cherenkov Detektoren. Diese Arbeit konzentriert sich auf H.E.S.S., ein Teleskopfeld aus fünf Cherenkov Teleskopen, und HAWC, ein Weitwinkel-Gammastrahlen-Observatorium, zwei Instrumente, die trotz ihrer instrumentellen Unterschiede sehr komplimentär arbeiten.

Ein Teil dieser Arbeit befasst sich mit dem HAWC Hochenergie-Upgrade durch das Outrigger Array, das während der Zeit dieser Doktorarbeit entwickelt und aufgebaut wurde. Ich stelle die Kalibration für die Energie- und Zeitrekonstruktion der Photomultiplier, mit der jeder der kleinen Outrigger Tanks ausgestattet ist, vor.

Ich präsentiere einen Vergleich der galaktischen Ebene, wie sie von HAWC und H.E.S.S. in der Überlappregion gesehen wird. Dabei weise ich auf die Ähnlichkeiten und Unterschiede hin, die durch die instrumentspezifischen Eigenschaften und ihrer jeweiligen Datenanalysen entstehen, und zeige, dass die Hintergrundabschätzung eine Hauptzutat ist. Die Region der galaktischen Ebene um die Quelle 2HWC J1928+177 wird näher untersucht. Ein Mehrkomponenten-Fit wird durchgeführt. Das beste Fit-Modell enthält zwei Punktquellen für 2HWC J1930+188 und die neue Quelle HWC J1932+192, eine ausgedehnte Quelle mit einer Größe von σ =0.17 ° für 2HWC J1928+177 sowie zwei weitere ausgedehnte Quellen, die für die Emission auf größeren Skalen verantwortlich zu sein schein.

DEDICATION AND ACKNOWLEDGEMENTS

This Ph.D. was for me a unique experience on every aspect. It is of course greatly due to the team I have been working with and all the people I met. I am very grateful to each person who encouraged me and supported me. It started with my physics teachers at school, Mme Bachelier and M. Berry, who gave me the taste for physics. It continued with my Master's internship supervisors in Toulouse, Timo Fleig, Natalie Webb and Pierrick Martin who really gave me the opportunity of discovering the world of research, and were always behind me during my Ph.D. applications. Then comes of course my Ph.D. supervisor Jim Hinton who gave me the chance to do my Ph.D. in this amazing environment which is the MPIK in Heidelberg. The main component of it is the members of the group he leads, our secretary Ruth, the permanent staff, the engineers and technicians from the electronics and mechanics workshop, the post-docs and the other Ph.D. students. In particular, the HAWC team, Ruben, Harm, Vincent, Felix, Vikas, Pooja and Edna who were very nice people to work with and to have fun with. A special acknowledgment goes to Mizzi, who was extremely patient with me and was always available to explain everything I needed, again and again! Thanks to all of you for your help, your ideas, your cross checks, and for reviewing my thesis several times and helping me to make it better. I also want to thank Sabina and Johannes for their German recipes, German book recommendation and for their German training. I want furthermore to thank the members of the HAWC collaboration who were always very kind and helpful. In particular, the outrigger team and the people I have been on the HAWC site with: Michael, Brenda, Scott and Arturo, and all the site crew: Manuel and his team.

Amongst the people who always encouraged me are of course the members of my family. I want to thank my parents for the education they have given me, the curiosity and the love of nature that I like to study and understand, and the freedom I always had in the choices I made. I also want to thank my brother and my sisters for their strong tie and their solidarity in all circumstances. I cannot forget my friends but I can also not cite all of them. In particular, Anthony was a constant support during my Ph.D. I wish that we continue along this path together.

Finally, I want to thank the members of my jury, Jim Hinton, Stefan Wagner, Tilman Plehn and Ulrich Uwer.

TABLE OF CONTENTS

List of Tables

List of Figures

CHAPTER 1

INTRODUCTION

Having access to the multiwavelength information of an object or a region is a huge enrichment for our understanding of this object itself, the material present in its environment, its interaction with its neighborhood and the physical processes taking place. The visible range is only a piece of the puzzle. A more complete picture becomes available when combining all the information from radio wavelengths to γ rays.

The γ-ray domain is at the far end of the electromagnetic spectrum. Gamma ray is the generic denomination of all photons more energetic than X-ray photons, with energies larger than ~100 keV. They are of particular interest because these γ-ray photons are not thermal radiation, meaning that they are not emitted by an object because of its temperature according to Planck's law, and cannot be described by a blackbody spectrum. They are produced by other processes such as synchrotron radiation, bremsstrahlung or inverse Compton scattering. These processes are described in the first section of this chapter.

This part of the spectrum has been accessible only since the 1970s and a lot of efforts have been made to develop the observational techniques and reconstruction methods to allow this domain to complete the global electromagnetic picture. This thesis focuses on γ-ray astronomy[1], more specifically on the Very High Energy (VHE) range between 100 GeV and 100 TeV, and its observations using imaging atmospheric Cherenkov techniques and water Cherenkov detection techniques in particular.

[1] Gamma rays are further divided into High Energy γ rays (HE: 30 MeV - 50 GeV), Very High Energy γ rays (VHE: 50 GeV - 100 TeV), Ultra High Energy γ rays (UHE: 100 TeV - 100 PeV) and Extremely High Energy γ rays (EHE > 100 PeV)

1.1 Production of cosmic rays and γ rays

Some extreme objects in the universe are able to accelerate particles. They were measured for the first time on Earth in 1909 by Theodor Wulf [100] and then in 1912 by Victor Hess[2] [50] using the electrometer developed by Theodor Wulf on board a balloon. He found that the ionisation rate kept increasing with altitude, from ground level to 5000 m, the highest altitude he could reach. He concluded that it was likely due to radiation coming from space penetrating the atmosphere, hence the name **cosmic ray** introduced by Robert Millikan[3] [70]. Arthur Compton claimed that these were actually charged particles [36]: electrons, protons, and helium nuclei. This was confirmed in 1929 in a experiment lead by Walther Bothe and Werner Kohlörster [28].

Since they are charged particles, cosmic rays are actually deflected by any magnetic field on their way, therefore, they do not point back to their origin. To investigate their sources, the neutral product of cosmic-rays collisions, such as γ rays, can be studied. First, acceleration mechanisms that accelerate cosmic rays to the observed high energies in the main galactic sources of cosmic rays are considered. Then, the mechanisms of γ-ray production are described.

1.1.1 Galactic accelerators and acceleration mechanisms

Particle acceleration takes place at the shock produced by an object with the interstellar medium (ISM). For example, massive stars, with masses between 8 and 40 solar masses [49], end their life in an explosion, known as **supernova**. There are in average 1 to 3 supernova explosions per century in our galaxy. They expel their material at velocities higher than the local sound velocity, producing a shock wave in the surrounding interstellar medium ahead of the ejecta. The expanding shock front and the material that has been ejected from the star during the explosion constitute the **Supernova Remnant** (SNR). The shock wave is responsible for compression, ionization and heating of the interstellar gas up to 10^7 - 10^8 K. The gas is mainly hydrogen, but there can also be heavier nuclei since it has been enriched by several generations of stars that exploded before. The protons, electrons and heavier nuclei at the shock front are accelerated by mechanisms such as the **Fermi acceleration**.

These particles will be confined until they have enough energy to escape, or until the shock dies out: after expanding over thousands of years and over tens of parsecs, it will slow down and its velocity will be eventually smaller than the local sound velocity. Because of the limited life time of the shock, SNR are able to accelerate cosmic rays up to a few hundreds of TeV. Particles accelerated at higher energies, above PeV energies, must come from another source, likely extragalactic.

[2] Victor Hess received the Nobel Prize in 1936 "for his discovery of cosmic radiation".

[3] Robert Millikan was awarded the Nobel prize in 1923 "for his work on the elementary charge of electricity and on the photoelectric effect".

The remaining core of the exploded star mentioned above collapses into objects of different nature, depending on the initial mass of the star [49]: if it had a mass between approximately 25 and 40 solar masses, the remaining core becomes a black hole. If its original mass was between 8 and 25 solar masses, a core of mass between 1.44 solar masses, known as the Chandrasekhar limit [34], and ~3 solar masses[4] [63] remains at the center of the SNR called **neutron star**. It is an extremely dense object[5] which rotates extremely fast on its axis because of angular momentum conservation, up to a few hundreds times per second [99]. Due to magnetic flux conservation, neutron stars are highly magnetised objects, with magnetic fields of the order of 10^{14} to 10^{16} G. They emit electromagnetic radiation in a so-called light cone of emission in a wide range of wavelengths from radio waves to VHE γ rays. If its magnetic axis is not aligned with its rotation axis, a pulse of emission can be seen on Earth each time the light cone of emission crosses our line of sight, at each rotation period. Moreover, neutron stars are further classified depending on the primary power source of their emission:

- Magnetars derive their energy from the magnetic field energy
- Isolated Neutron Stars take their energy from the latent heat of the neutron star matter
- Accretion-Powered Neutron Stars (APNSs) are powered by the energy released by matter accretion to the neutron star
- Compact Central Objects (CCOs) only manifest thermal X-ray emission
- Pulsars are neutron star that derive their energy from their rotation.

On the neutron star surface, very strong electric fields induced by the rotation of the pulsar pull electrons from the surface. They are accelerated while propagating along the magnetic field lines and emit photons via curvature radiation. Due to the strong magnetic field, these very energetic photons produce electron-positron pairs that are further accelerated. The process can be repeated multiple times into a cascade. A **pulsar wind** is formed by these particles and the magnetic field. A shock front is created between the pulsar wind and the supernova remnant material, or the interstellar material where particles are further accelerated. The region from the central pulsar to this shock front is known as **Pulsar Wind Nebula** (PWN). The PWN is continuously maintained by the pulsar wind.

1.1.2 Observational properties

Pulsars, PWN and SNRs are the most common galactic sources on the VHE γ-ray sky observed with the current instruments. Traditionally, pulsars are detected thanks to their radio pulsed emission. The Arecibo radio telescope made for example dedicated surveys for this purpose:

[4] The upper limit is not know exactly, it depends on the initial conditions.

[5] A neutron star have a typical diameter of 10 km and a mass of 1.4 $M_\odot$ which implies a density of 10^{15} g cm^{-3}.

the Pulsar Arecibo L-band Feed Array (PALFA), has discovered a total of 185 (as of October 2018) previously unknown pulsars. A lot of pulsars detected in radio have no counterpart in other wavelengths yet. X-ray emission mainly from synchrotron also allows to detect them with instruments like *Chandra*, *XMM-Newton*, *Swift*, *NuSTAR* or *Suzaku*.

The nebula around looks more extended in X-rays and the edges are usually not well defined. Numerous PWNe have also been detected, in γ-ray for example, without detecting their pulsar in any other wavelengths. They tend to look more extended in γ-ray than in X-ray, although this depends on the energy of the electrons producing the emission. PWNe can have a huge variety of shapes and morphologies, depending on their age, the power and the motion of the pulsar in the ISM, and the surrounding environment. They can be found embedded in the shell of SNRs larger than the PWN, but also entangled without the possibility of distinguishing one from the other. There are also several PWNe with no observed SNR. The pulsar and PWN can also have moved away from the center of the SNR with time.

Finally, SNRs are often detectable in radio wavelengths due to synchrotron emission. They also take a variety of shapes. Since the material of the SNR interacts with the ISM, they also emit infrared emission.

1.1.3 Properties of pulsars

Using the pulsar **spin period** P, the **period derivative** $\dot{P} = \mathrm{d}P/\mathrm{d}t$, determined from the observation of the pulsed signal and the **initial period** of the pulsar noted P_0, pulsars are described by the following characteristics [42]:

- The variation of angular velocity is:

$$\dot{\Omega} = -k\Omega^n \qquad \text{with} \qquad \Omega = \frac{2\pi}{P} \tag{1.1}$$

  and n the breaking index which has been measure for a few pulsars only. It is usually assumed that $n \simeq 3$.

- Assuming k constant, the **age** of the system is

$$\tau = \frac{P}{(n-1)\,\dot{P}}\left[1 - \left(\frac{P_0}{P}\right)^{n-1}\right] \tag{1.2}$$

  Using $n \simeq 3$, the **characteristic age** is

$$\tau_c = \frac{P}{2\dot{P}} \tag{1.3}$$

  It is usually an overestimation of the true age of the pulsar. We define the initial spin down time scale:

$$\tau_0 = \tau_c - \tau \tag{1.4}$$

  The pulsar is assumed to release a constant amount of energy until τ_0 beyond which it decreases with time.

- the **rotational energy** E_{ROT} which is the source of most of the observed emission is:

$$E_{\mathrm{ROT}} = \frac{I}{2}\Omega^2 \tag{1.5}$$

The rate at which the rotational energy is dissipated is the **spin-down luminosity**:

$$\dot{E} = \frac{\mathrm{d}E_{\mathrm{ROT}}}{\mathrm{d}t} = 4\pi^2 I \frac{\dot{P}}{P^3} \tag{1.6}$$

where I is the moment of inertia of the pulsar. It has a typical value of 10^{45} g cm^{-2}. For the whole population of pulsars $\dot{E}$ ranges from 10^{28} to 10^{38} erg s^{-1}. However, only pulsars with $\dot{E} \gtrsim 10^{35}$ are powerful enough to produce the PWN that are observed in γ rays. It can also be written as a function of the **initial spin down luminosity** $\dot{E}_0$:

$$\dot{E} = \dot{E_0}\left(1 + \frac{t}{\tau_0}\right)^{-\frac{n+1}{n-1}} \tag{1.7}$$

- Similarly, the spin period can be written:

$$P = P_0\left(1 + \frac{t}{\tau_0}\right)^{\frac{1}{n-1}} \tag{1.8}$$

1.1.4 From cosmic rays to γ rays

The emission mechanisms that are responsible for the emission of γ-ray photons are due to 3 main ingredients: charged particles evolving in a magnetic field with relativistic velocity. They interact in several ways with the environment where they are accelerated, via different non thermal processes described in the following paragraphs. Figure 1.4 is an illustration of the contribution of each emission process to the γ-ray energy spectrum.

Synchrotron radiation

Relativistic charged particles in an external magnetic field orbit around the magnetic field lines, get accelerated under the Lorentz force $\vec{F}$ and emit photons in the X-ray and γ-ray domain perpendicularly to the acceleration. This is called synchrotron radiation and is illustrated in Figure 1.1. This is the case for the electrons extracted from the pulsar surface and orbiting around the open magnetic field lines, but also everywhere in the PWN or the SNR where a magnetic field is present.

The energy loss for electrons producing synchrotron radiation is:

$$\frac{dE}{dt} = \frac{4}{3}\sigma_T\left(\frac{v}{c}\right)^2 c\gamma^2 U_{\mathrm{mag}} \tag{1.9}$$

with $U_{\mathrm{mag}} = \dfrac{B^2}{2\mu_0}$ the magnetic energy density and $\gamma = \dfrac{1}{\sqrt{1-\beta^2}}$ the Lorentz factor with $\beta = \dfrac{v}{c}$

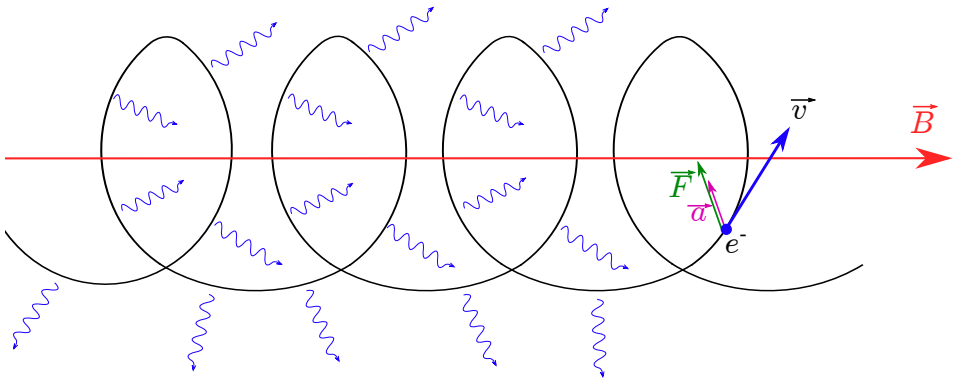

Figure 1.1: Synchrotron radiation for a charged particle (here negative) in a uniform magnetic field.

It can also written in this form:

$$\frac{\mathrm{d}E}{\mathrm{d}t} \simeq 2.6\left(\frac{Zm_e}{m}\right)^4 E^2 B^2 \quad \text{keV s}^{-1} \tag{1.10}$$

with m the mass of the charge particle, Ze its charge, E the energy in keV and B the magnetic field in gauss. Since a proton is ~ 2000 times heavier than an electron, the energy loss is more important for electrons. The cooling time for these electrons is:

$$\tau_s = \frac{E_e}{\mathrm{d}E_e/\mathrm{d}t} = 1.3.10^7 \frac{1}{B^2}\frac{1}{E_e} \quad \text{yr} \tag{1.11}$$

with B the magnetic field in μG and E_e the electron energy in TeV.

Curvature radiation

Relativistic charged particles following magnetic field lines that are curved, such as the closed magnetic field lines around a pulsar, are accelerated perpendicularly to the lines and emit curvature radiation. If they reach relativistic velocities, the emission will be in the X-ray or γ-ray domain.

Inverse Compton scattering

The scattering of photons by relativistic electrons is called inverse Compton scattering. In the process, the electrons lose energy that is transferred to the photons that is boosted. This is illustrated in Figure 1.2. It happens for example in the interstellar medium when a relativistic particles encounters photons from the cosmic microwave background, but also in the pulsar magnetosphere where thermal X-ray photons emitted by the pulsar are scattered by relativistic electrons. The energy loss of electrons up-scattering a radiation field with a radiation energy densities U_{rad} is:

$$\frac{\mathrm{d}E}{\mathrm{d}t} = \frac{4}{3}\sigma_T\left(\frac{v}{c}\right)^2 c\gamma^2 U_{\mathrm{rad}} \tag{1.12}$$

with $U_{\rm rad}$ in eV cm^{-3}. The cooling time of these electrons is:

$$\tau_{\rm IC} = \frac{E_e}{{\rm d}E_e/{\rm d}t} = 3.1.10^5 \frac{1}{U_{\rm rad}\, E_e\, f_{\rm KN}} \qquad {\rm yr} \tag{1.13}$$

with E in TeV, $U_{\rm rad}$ in eV cm^{-3} and $f_{\rm KN} \simeq (1+40E_e k_B T)^{-1.5}$ the Klein Nishina suppression factor, with $k_B T$ in eV.

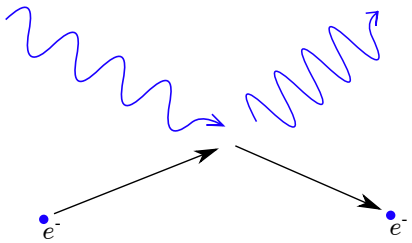

Figure 1.2: Inverse Compton scattering.

Bremsstrahlung

When a charged particle passes by an ion or a nucleus, it is globally decelerated, and produces a photon which energy corresponds to the velocity loss. It is called bremsstrahlung radiation and is illustrated in Figure 1.3. If the particle's velocity is high enough, the emitted photon will be a γ photon.

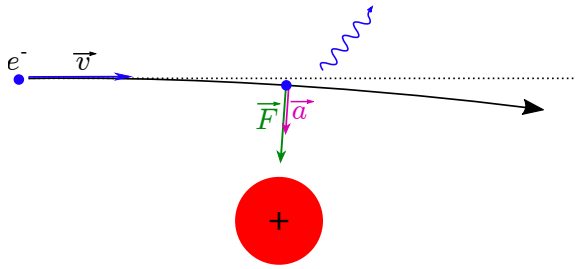

Figure 1.3: Bremsstrahlung emission.

Neutral pion decay

From a hadronique point of view, a proton colliding with another proton or a nucleus produces positive, negative or neutral pions in equal amount. Neutral pions usually decay into two γ photons. This is called **neutral pion decay**. The spectral energy distribution of γ rays produced by neutral pion decay peaks at $m_\pi c^2/2 \simeq 67.5$ MeV.

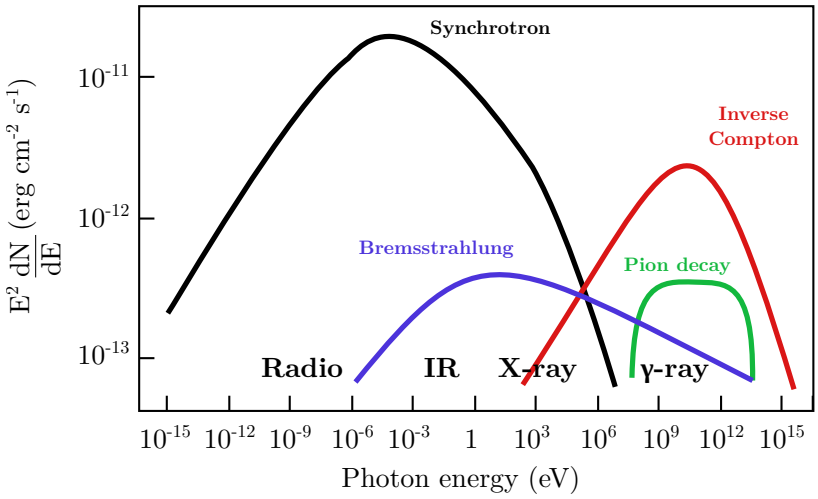

Figure 1.4: Spectral energy distribution of γ-rays produced via synchrotron, inverse Compton scattering, bremsstrahlung and neutral pion decay.

1.2 Gamma-ray astronomy and detection techniques

Gamma-ray astronomy is a rather young field that has been exponentially developing, making huge progress over the last decades. Figure 1.5 shows the evolution of the number of sources detected in X-rays and in γ-rays during the past 70 years. Observation of γ rays became possible for the first time in the 1960s, when γ rays from solar eruptions were observed at a few MeV[6] The atmosphere being opaque to γ rays, the first idea was to send instruments on board satellites to detect them directly from space. These instruments are typically composed of a tracker, which records the trajectory of the particles produced by the interaction of a γ-ray photon with the detector medium, and a calorimeter which measures their energy deposition. Additionally, an anti-coincidence detector is very useful for distinguishing between γ rays and cosmic rays, which is the main source of background. The first two satellites dedicated to γ-ray detection were SAS-2 [39] launched in 1972 and COS-B[7] [24] launched in 1975. SAS-2 reported a few sources with emission above 100 MeV: the Crab and Vela pulsars, Cygnus X-3, Geminga, and the galactic center. It stopped operating after only 7 months because of an electronic failure. COS-B produced the first catalogue of 25 sources at energies above 300 MeV [86] and reported diffuse emission from the galactic plane [25] in about 6 and a half years of operation. EGRET (Energetic Gamma Ray Experiment Telescope) on board the CGRO (Compton Gamma Ray Observatory) satellite was launched in 1991. It completed an all-sky survey [89] [40] and reported 271 sources with γ-ray emission above 100 MeV. It detected 7 pulsars, and γ-ray blazars which were identified as a new class of objects. It also observed γ rays from γ-ray bursts (GRB) at

[6]This was predicted by Philip Morrison in 1956 [71].
[7]COS-B was the first ESA mission

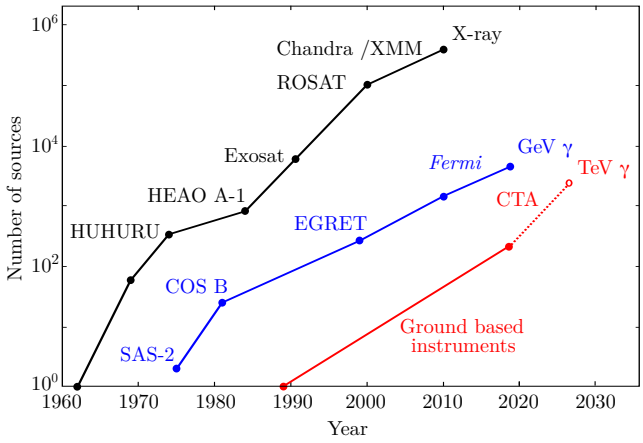

Figure 1.5: The so-called Kifune plot depicts the number of sources detected with time. It includes the 2XMMi-DR3 list of 262902 X-ray sources [95], the 4FGL catalogue of 5098 GeV γ-ray sources [2], and the TeVCat list of 223 TeV gamma-ray sources [94]. Simulations of CTA performance predicts that ~1000 TeV sources will be detected by CTA [92].

GeV energies. Moreover, it detected emission from the large and the small Magellanic clouds. Finally, *Fermi* was launched in 2008 and is currently in operation. It covers an energy range from 20 MeV to 300 GeV. Its latest catalogues, the 4FGL catalogue[8] and the 3FHL catalogue[9] for sources above 10 GeV, are referenced. The galactic plane contains the vast majority of the known γ-ray sources [15]. Supernova Remnants (SNRs) and Pulsar Wind Nebulae (PWNe) represent the majority of the identified VHE γ-ray galactic sources. There are also a few binary systems, composed of a compact object like a neutron star and a companion star, and diffuse emission. Beyond our galaxy, almost all known γ-ray sources are Active Galactic Nuclei (AGNs), most of them falling into the blazar category, the relativistic jet being directed towards the Earth.

However, with increasing energy, the probability to detect γ rays becomes lower. For instance, a 1 m^2 detector would see roughly 1 photon from the Crab[10] of energy between 100 MeV and 5 GeV every minute. Between 50 GeV and 1 TeV, a 1 m^2 detector would see 1 photon per day and above 1 TeV it drops to 7 photons per year. Hence, bigger detectors are needed to get enough events at higher energy. Such big detectors cannot go into space, but have to be installed on the ground. Two main detection techniques have been developed to detect γ rays at ground level,

[8]The 4FGL catalogue contains 5098 sources, using 8 years of data

[9]The 3FHL catalogue contains 1556 sources, using 7 years of data

[10]The Crab has an integral flux between 100 MeV and 5 GeV of $2.2.10^{-6}$ photons per cm^2 per s, and a differential flux that falls as $E^{-2.1}$ [74]. Between 50 GeV and 10 TeV the crab differential energy spectrum is well described by a log parabola function:

$$\frac{dN}{dE\,dA\,dt} = (3.23 \pm 0.03).10^{-11}\left(\frac{E}{\text{TeV}}\right)^{(-2.47\pm0.01)+(-0.24\pm0.01)\log\left(\frac{E}{\text{TeV}}\right)} (\text{TeV}^{-1}\ \text{cm}^{-1}\ \text{s}^{-1}) \tag{1.14}$$

Hence its integral flux is $1.26.10^{-9}$ photons per cm^2 per s between 50 GeV and 1 TeV and $2.14.10^{-11}$ photons per cm^2 per s above 1 TeV [21]

both taking advantage of the Cherenkov light produced by a particle traveling in a medium faster than the speed of light in this medium. The first one, called Imaging Atmospheric Cherenkov Technique (IACT) detects the Cherenkov light produced by the particles of air showers in the atmosphere[11]. The second one, called Water Cherenkov Detection (WCD) technique records the Cherenkov light produced by these particles in water at ground level. Both techniques, illustrated in Figure 1.6, have advantages and disadvantages, but they are quite complementary, as will be discussed in the next sections.

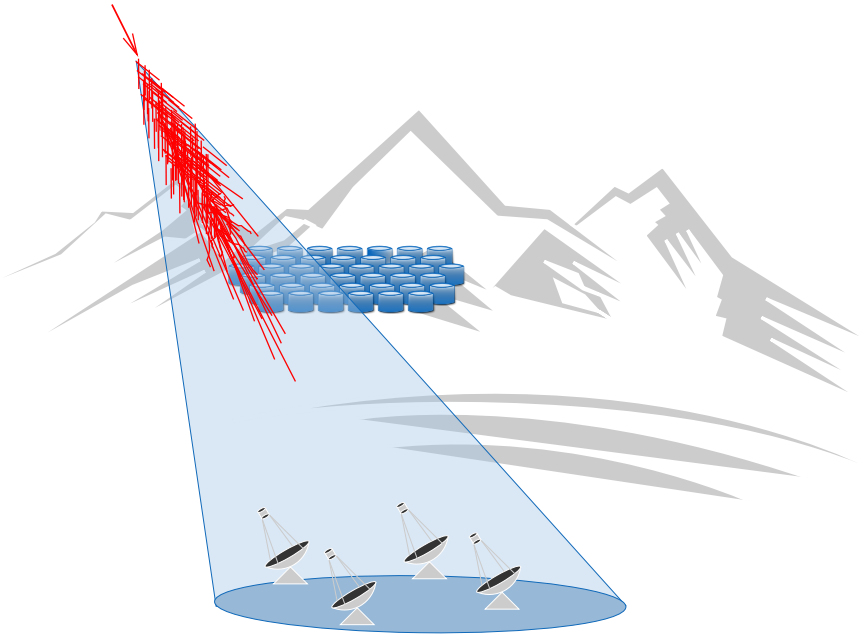

Figure 1.6: A charged particle or a γ ray enters the atmosphere and produces a shower of secondary particles. These particles are detected by the WCD when they produce Cherenkov light in the water. They also produce Cherenkov light in the air, detected by IACTs at lower altitude.

1.2.1 Extensive air shower and Cherenkov light

Ground-based detection techniques use the product of the interaction of cosmic rays or γ rays with the molecules of the atmosphere. Indeed they have relativistic energies and when they reach the Earth, they interact as soon as they enter the upper atmosphere with a molecule and produce showers of secondary particles called Extensive Air Shower (EAS). The nature of the secondary particles in the shower depends on the nature of the primary particle as shown in Figure 1.7. In the case of a γ ray, the EAS will be mainly electromagnetic: the γ ray scatters off an atmospheric nucleus and produces an electron-positron pair, which emits γ rays via bremsstrahlung when passing by a nucleus and will further produce electron-positron pairs. On the other hand, a

[11] Cherenkov light emission induced by a cosmic ray in the atmosphere were first detected in 1952 [43]

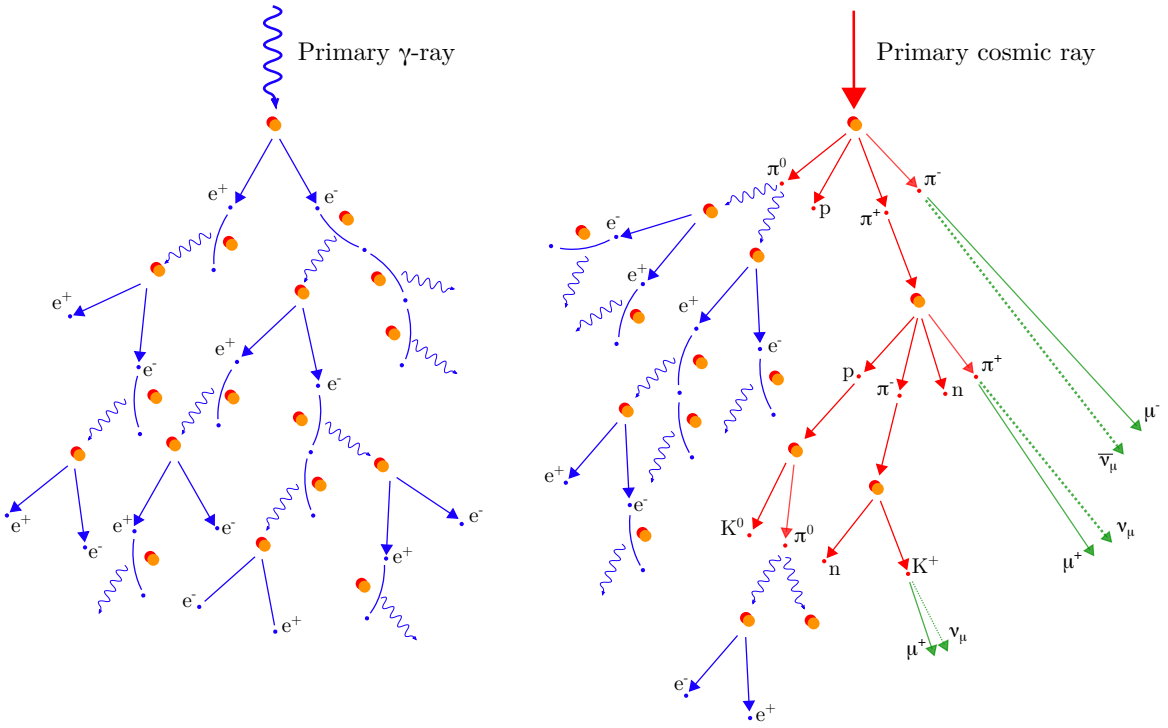

Figure 1.7: Extensive air shower induced by a γ ray and a cosmic ray. Blue represent the electromagnetic part of the shower, clearly dominant for a γ-ray shower. Red is the hadronic part and green the muonic part of a cosmic-ray shower.

hadron colliding with an atmospheric molecule produces mainly pions and kaons that further produce muons. Those which keep colliding with other atoms will produce more of these particles. This is the hadronic component of the shower. Pions and kaons are not stable. The neutral pions decay into two γ rays, originating the electromagnetic component of the cascade. Charged pions decay into muons and neutrinos, and produce the muonic component of the shower. They carry the most of the shower energy and can reach the ground without further interaction. Kaons can decay either into muons and neutrinos or into pions. Of course, the particles lose some of their energy in each interaction. Hence, the shower first grows in size with the increasing number of interactions creating more particles, until it reaches a maximum size referred to as the shower maximum. This happens typically at around 8 km in altitude for a 1 TeV primary particle. Then the shower slowly dies out until the particles do not have enough energy to undergo any more interaction, typically around the altitude ok 1 km for a 1 TeV shower [53]

In both cases, the charged particles are traveling in the atmosphere at a velocity v larger than the speed of light in the medium, that is the ratio of the speed of light in vacuum by the refractive index of air c/n. They emit a cone of blue light, in the visible and ultraviolet domain,

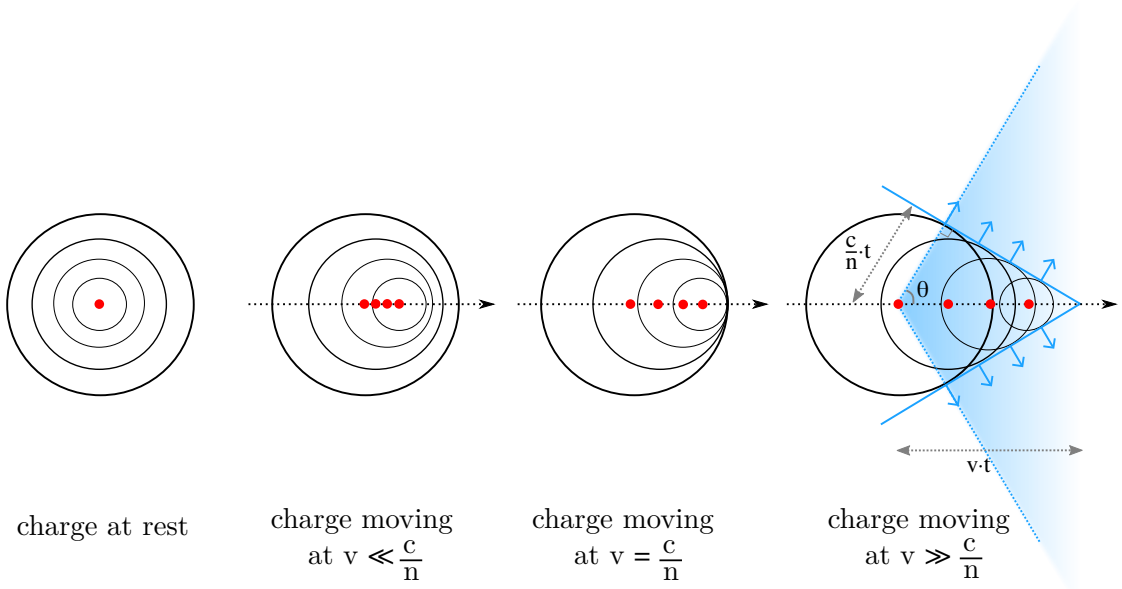

Figure 1.8: A charged particle traveling at a velocity v larger that the speed of light c in a medium of refractive index n emits Cherenkov light in a cone with opening angle θ.

called Cherenkov[12] light as sketched Figure 1.8. The opening angle θ of this cone depends on the refractive index of the medium as:

$$\cos\theta = \frac{c}{v.n} = \frac{1}{\beta.n} \qquad \text{where} \quad \beta = \frac{v}{c}$$

In the atmosphere, the refractive index[13] is $n = 1.0003$, hence the opening angle is $\theta \simeq 1°$. In water, $n = 1.3$ and $\theta \simeq 40°$. The Cherenkov light induced by all particles in the air shower produce overlapping rings on the ground. The ground area illuminated by Cherenkov photons from a shower of 1 TeV has a radius of ~120 m.

1.2.2 Imaging Atmospheric Cherenkov Telescopes

The first detection technique is used by Imaging Atmospheric Cherenkov Telescopes (IACTs). They use the atmosphere as a calorimeter where the charged particles from the extensive air shower propagate at a velocity larger than the speed of light in the atmosphere and produce a pool of Cherenkov light. IACTs located inside this light pool detect this light in the shape of an ellipse on their camera. The parameters that are derived from this image, which characterise

[12] Pavel Cherenkov got the Nobel prize in 1958 (shared with Ilya Frank and Igor Tamm) « for the discovery and the interpretation of the Cherenkov effect » and awarded the Soviet Union's Hero of Socialist Labour title in 1984. Blackett was the first to realise that cosmic-ray air showers would produce enough Cherenkov light to be detectable, in 1948. Galbraith and Jelley detected it for the first time in the early 1950s [44].

[13] Refractive index at ~8km above see level ; it is a function of the density of the air, and thus increases downwards.

the ellipse in terms of size, shape and amplitude, are called Hillas parameters [51]. They allow for the reconstruction of the direction, energy and type of the incoming particle originating the atmospheric air shower. Combining the images from several IACT cameras, as sketched in Figure 1.9, gives a stereoscopic view of the shower, and the direction of the incoming particle can be better reconstructed.

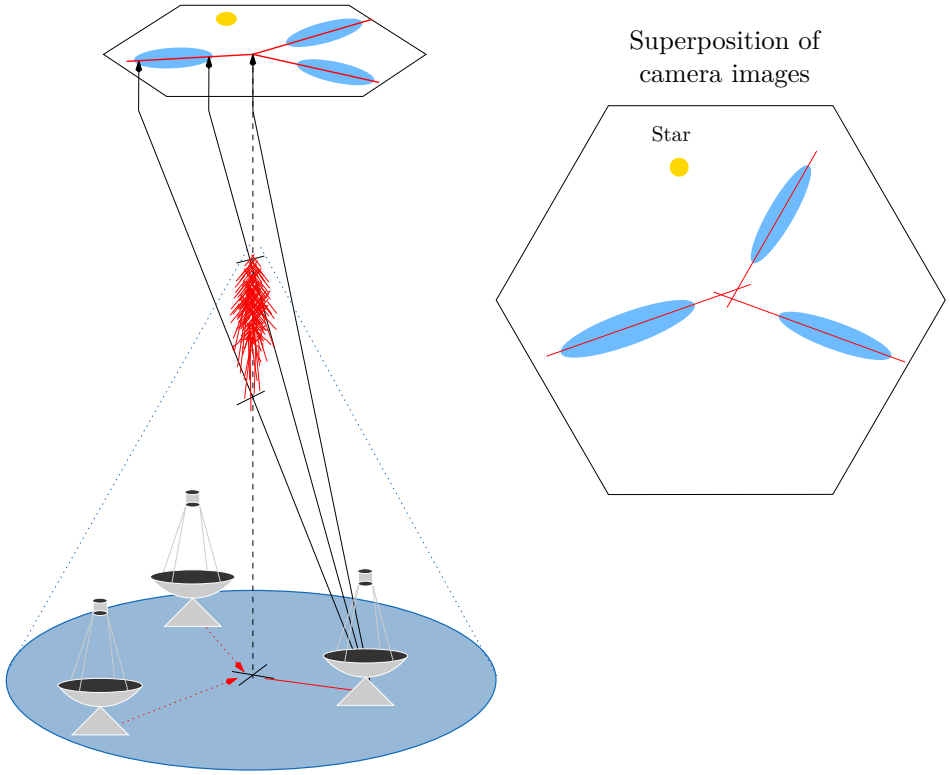

Figure 1.9: Reconstruction of the image on the telescope cameras

Observations indicating a 3σ excess above 0.1 TeV from the direction of the Crab Nebula were first reported in 1972, using data taken between October 1971 and April 1972 with a 10 m optical reflector on Mount Hopkins in Southern Arizona, the first generation of atmospheric Cherenkov detector [90]. The first official detection is made in 1988 by the Fred Lawrence Whipple Observatory, with a 9σ detection above 0.7 TeV using 85 hours of data [33] [98] and in 1991, with a 20σ detection using 30 hours of data[14] [90]. In 1988, a first catalogue of VHE γ-ray sources above 0.1 TeV is published with 13 objects [97]. The Crab spectrum is measured up to 50 TeV by the CANGAROO telescopes in 1998 [87]. From an extragalactic perspective, TeV emission from extragalactic objects was also detected, and in particular the Whipple observatory reported in 1992, the detection of the AGN Marakarian 421 with a statistical significance of 6σ [78]. This detection was confirmed by HEGRA in 1996 above 1 TeV [73]. HEGRA is the

[14]This was possible thanks to an upgrade of the Whipple telescope camera which led to an improved resolution.

first stereoscopic system[15] based on the simultaneous detection of air showers by more than 2 telescopes. Since then, the detection of new sources of TeV γ rays kept increasing with the new generations of instruments. Today, there are three arrays of telescopes in operation: the High Energy Stereoscopic System (H.E.S.S.) in Namibia, the Major Atmospheric Gamma-ray Imaging Cherenkov telescope (MAGIC) on the Canary Island of La Palma and the Very Energetic Radiation Imaging Telescope Array System (VERITAS) in Arizona, USA. All are located at an altitude between 1500 and 2200 m above sea level. The next project to come is the Cherenkov Telescope Array (CTA) which will be an array of several tens of IACTs of different sizes, on two sites in both hemispheres to get the best performances and the best sky coverage ever achieved by IACTs.

The strength of the IACTs is their angular and energy resolution, their effective area and their good γ/hadron separation. However, they are limited by their rather small field of view[16] and duty cycle, since they can operate only during night and are affected by moon light and weather conditions, corresponding to ~1000 hours observation per year.

1.2.3 Water Cherenkov Detectors

The other technique uses water as a detection medium. These Water Cherenkov Detectors (WCDs) need to be at higher altitude than IACTs since they directly detect particles from the extended air shower. A shower initiated by a 1 TeV photon typically has its shower maximum at 8 km above see level. Therefore, they are placed higher in alitude to be closer to the shower maximum. Contrary to IACTs, the main advantage of these detectors is that they can monitor the whole sky above them all the time, night and day, independently of the weather conditions. However, their energy and angular resolution is not as good as those of IACTs.

The MILAGRO experiment belongs to the first generation of such detectors. It was consisting of an 8 m deep pool of water with a surface area of 5000 m^2, and was located at an altitude of 2630 m in New Mexico, USA. It detected the first 6 sources [84] at TeV energies using this technique, during 6 years of operation. The new generation, namely the High Altitude Water Cherenkov (HAWC) observatory, has been built in Mexico at an altitude of 4100 m and is in operation since 2015. It consists of an array of 300 WCDs covering an area of 22000 m^2. Other experiments dedicated to other studies also use WCDs: The Pierre Auger observatory in Argentina, is a hybrid detector which uses 1660 water tanks, studying ultra-high energy cosmic rays above 10^{18} eV. The neutrino detector IceCube at the South pole has also an array of 162 ice tanks called IceTop, located at the surface of the IceCube detector and aim at detecting cosmic-ray events in coincidence by both the surface array and the deep detectors. More experiments are coming, such as the Large High Altitude Air Shower Observatory (LHAASO) in the Sichuan

[15] Field of view of HEGRA: 4.3°

[16] Field of view of H.E.S.S.: 5°, field of view of MAGIC and VERITAS: 3.5°

province of China or a future southern γ-ray observatory[17].

Other extended air shower detectors have also been developed such as ARGO, completed in 2007 at an altitude of 4300 m in Tibet. The detector, optimised to work in the TeV range, covers a surface of 111×99 m^2 with resistive plate chambers using gas to detect charged particles. Radio detection of extended air shower is also possible thanks to the reflection of radio waves by the ionisation produced by air showers in the atmosphere. The Jicamarca Radio Observatory, close to Lima, covers an area of 85000 m^2 with antenna to detect such signals.

[17] https://www.sgso-alliance.org

CHAPTER 2

TWO GROUND BASED γ-RAY EXPERIMENTS: H.E.S.S. AND HAWC

Two experiments are presented in this chapter that illustrate the two different techniques described previously: the first one, H.E.S.S., belongs to the third generation of Imaging Atmospheric Cherenkov Telescope (IACT). The second one, HAWC, is a water Cherenkov detector and belongs to the second generation of its kind. Both instruments are described, and their data analysis chain is explained from the detection of an event to its reconstruction and the map making. Data from both instrument have been used to perform the study presented in the next chapters.

2.1 The High Energy Stereoscopic System array

2.1.1 The array layout and telescopes properties

H.E.S.S. is an array of five IACTs located in the Khomas Highland in Namibia at a latitude of -23°, and at an altitude of 1800 m. Four identical telescopes, located on the corners of a square of 120 m length, started operation in 2003 as H.E.S.S. phase I. They have a 12 m diameter tessellated mirror made of 380 panels. They detect simultaneously the Cherenkov light from the air showers produced by γ rays in the atmosphere. They are sensitive to γ rays in the energy range from 100 GeV to 100 TeV. The array has an angular resolution of ~0.1 deg and an energy resolution of ~15% [17]. A fifth telescope, called CT5, with a 32.6×24.3 m mirror was added in 2012 at the center of the array to lower the energy threshold from 100 GeV to 30 GeV. It is the largest IACT ever built and is called H.E.S.S. phase II. Figure 2.1 shows the full H.E.S.S. array. It can be operated using only the four telescopes of H.E.S.S. I, if at least two of them trigger, or in hybrid mode using the five telescope. At the moment, this fifth telescope participates in ~90% of the triggered events, the 10% missing being due to its smaller field of view, 3.5° compared

to 5° for the smaller telescopes. The telescopes are evolving with time, for example the optical efficiency decreases progressively and the mirrors need to be re-coated during the experiment live-time.

As mentioned earlier, the air shower generated by a γ ray or a cosmic ray produces a pool of Cherenkov light that appears in the shape of an ellipse in the camera of the IACTs located in this pool. The image obtained with a telescope shows the track of the air shower. Each camera consists of Photomultiplier tubes (PMT)[1], 960 for each of the four small telescopes and 2048 for the bigger telescope. Each PMT is equipped with Winston cones. They are hexagonal light collectors used on top of the PMTs to reduce dead space between them and hence increase the collection area. The PMT and its Winston cone constitute a pixel of the camera. Their angular size is $\sim 0.16°$ and $\sim 0.067°$ respectively [79] [27].

H.E.S.S. is operated by shifters on site every moonless and clear night following an observation program. Observations necessitate the pointing of the telescopes towards the region of interest. Observation are split in runs of typically 28 minutes. H.E.S.S. takes in average 1000 h of data per year.

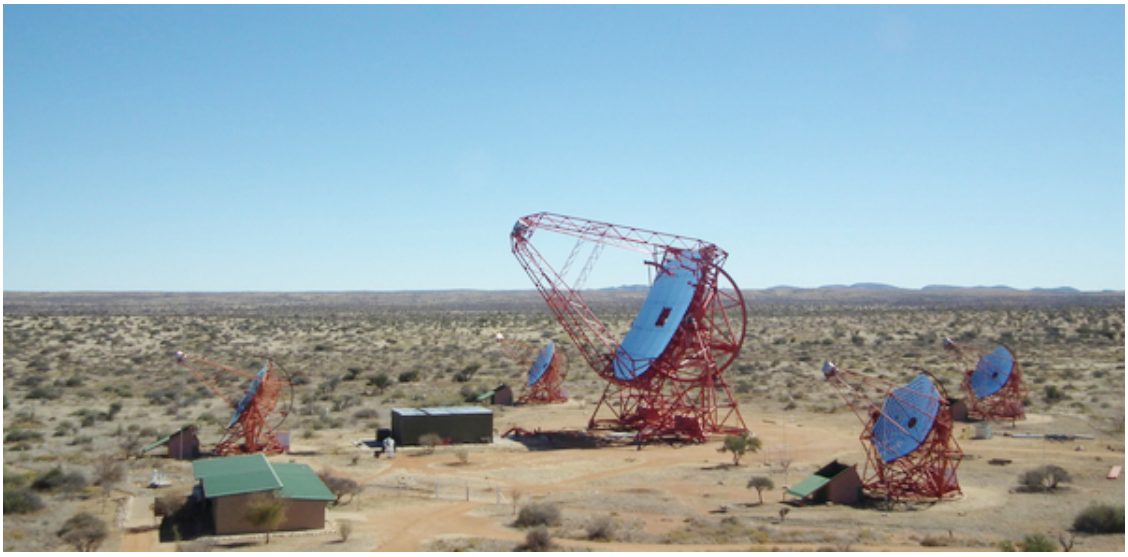

Figure 2.1: The H.E.S.S. array in Namibia, composed of the four 12 m telescopes and the 28 m telescope in the middle (credit : H.E.S.S. collaboration).

2.1.2 Data analysis

Calibration

Calibration of each pixel is of course an essential step for the image analysis [16]. The signal in each PMT is digitalised and the calibration gives the conversion between ADC counts, and

[1]The PMTs are 30 mm Photonis XP-2960 and 42 mm XP-29600 for the small and the big telescope respectively

the number of photoelectrons extracted from the PMT photocathode that produced this signal. Thanks to a flashing LED that illuminates the camera with very low intensity to be in the single photoelectron regime, the PMT gain is determined and the electronic baseline[2] is measured. The amplitude recorded in each pixel needs to be corrected as well by the relative efficiency of each pixel compared to the mean value over the whole camera. This correction accounts for the difference in optical and quantum efficiencies between pixels within a camera. It is obtained by illuminating the camera with a uniform high intensity light.

Another step is the cleaning of the raw images, needed to reduce the effect of the night sky background. In addition, some quality cuts are applied: first, any defect pixel is identified and excluded from the analysis. If a telescope counts more than 15% of broken pixel, the whole telescope is discarded from the event reconstruction. Secondly, the quality of the image is directly related to the quality of the atmosphere [48]. Hence, if the trigger rate is much lower than the mean trigger rate, or if significant fluctuations are recorded, the run is discarded.

Event reconstruction

In the standard analysis, the image is parametrised using the **Hillas method** [51], based on the fact that the image of the Cherenkov light produced by a γ-ray shower on the camera has an elliptical shape. The major axis of the ellipse gives the incoming direction of the shower. If seen by several telescopes from different points of view, the stereoscopic view has the advantage of getting a better reconstruction of the geometry of the shower and a precise direction of the incident particle, by intersecting the major axis of the different camera images. Figure 2.2 depicts the images of the five telescopes of the same 700 GeV γ-ray shower, and the final picture when combining all of them. The intersection of the major axis of the ellipses gives the original γ-ray direction. Moreover, the intensity of the image is related to the energy of the incident particle. The shape of the camera image is also used to distinguish between γ rays and cosmic rays. Figure 2.3 shows the image of a γ ray compared to a cosmic ray in a camera. The cosmic ray looks more irregular with substructures: because the initial particle is different, the shower development is different and involves different particles as was described in Section 1.2.1. Hence a cosmic ray shower is likely split into sub-showers and involves muons for example, that carry a large fraction of the shower to the ground and will produce very specific feature in the camera.

Another approach is to use a table of templates produced by Monte Carlo simulation of air showers. The observed image is compared to these templates and a likelihood fit is performed to get the best shower parameters described earlier and reconstruct the direction and the energy of the shower. This is the Image Pixel-wise fit for Atmospheric Cherenkov Telescopes (**ImPACT**) reconstruction [72]. Because it uses full Monte Carlo simulations in combination with an accurate model of the expected camera images, it shows improved performance compared to the traditional

[2]The electronic baseline is also called electronics pedestal. The pedestal position is defined as the mean ADC value recorded in the absence of any Cherenkov light [16]

Hillas method over the whole energy range, and even more pronounced at the highest energies.

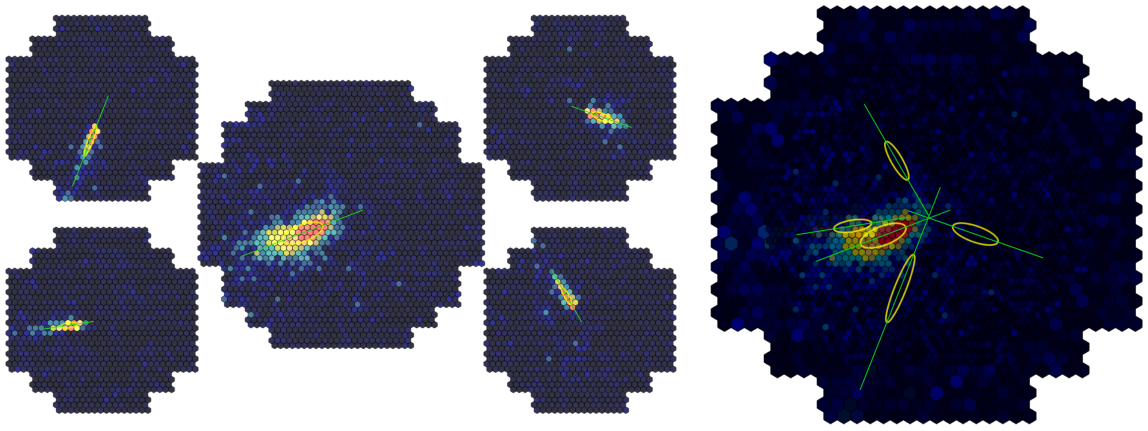

(a) (b)

Figure 2.2: Simulation of a 700 GeV γ ray seen by the five telescope cameras of the H.E.S.S. array: (a) shows the camera images separately, the middle one being the H.E.S.S. II telescope camera, and (b) is a superposition of all the ellipses and their major axis of all cameras (credit : Ramin Marx, MPIK Heidelberg, and the H.E.S.S. collaboration).

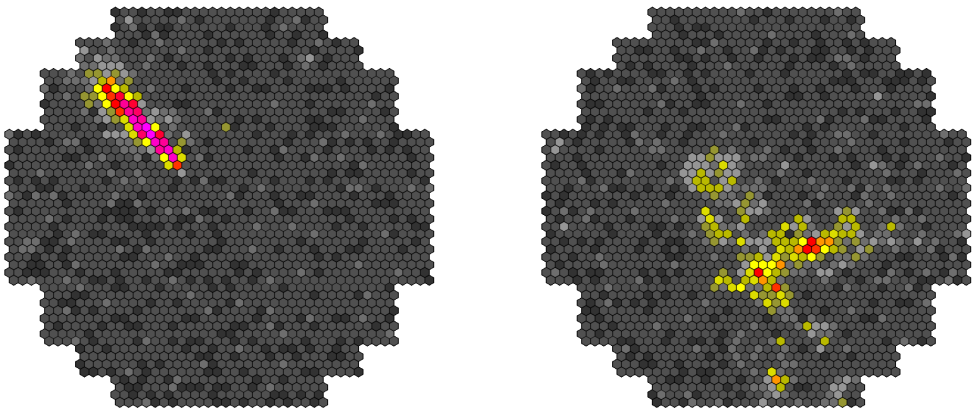

(a) (b)

Figure 2.3: The shape of the camera image allows distinguishing between a γ ray (a) and a cosmic ray (b) as seen here by the camera of the H.E.S.S. II telescope (credit : Ramin Marx, MPIK Heidelberg, and the H.E.S.S. collaboration).

Figure 2.4 shows the angular resolution as a function of energy and zenith angle and the energy resolution for ImPACT and Hillas reconstruction methods. The best angular resolution is 0.04° achieved above 10 TeV for zenith angle lower than 30° with ImPACT. The energy resolution is also a factor of 2 better using ImPACT, lower than 10% above 1 TeV.

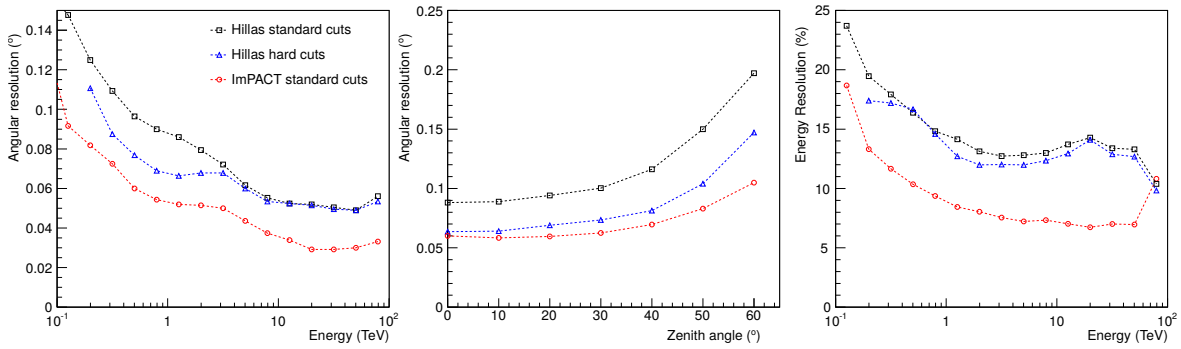

Figure 2.4: H.E.S.S. angular resolution as a function of energy (left) and zenith angle (middle) and energy resolution (right). The black curves uses the Hillas reconstruction method and standard cuts. The blue curves, using Hillas reconstruction and hard cuts is used for H.E.S.S. Galactic Plane Survey (HGPS [47]). The red curves uses ImPACT reconstruction. From [47].

2.1.3 Map making

Each event in an observation run gets assigned the reconstructed coordinates in the sky where it is coming from, and the reconstructed energy. A correction taking into account the observation conditions and the acceptance of the system needs to be applied. The acceptance is defined as the probability of accepting, after triggering, analysis cuts and γ-ray selection, a background event reconstructed at a certain position in the field of view and with a certain energy. It is generated as the number of background events as a function of the angular distance between reconstructed events direction and system pointing direction. Observations without significant γ-ray sources in the field of view have been used to obtain a model of the radial system acceptance [23].

Figure 2.6 illustrates the different steps in the map making process on observation runs of the Crab. First, cuts on parameters describing the shape of the camera image are applied to reduce background events by a factor of 100. What remains are γ-ray-like events which are real γ events and cosmic rays that look like γ rays. This is shown in map (a), called the ON map, which is a count map of γ-like events of the region of interest. The number of counts in each pixel is N_{ON}. To estimate the remaining background, an OFF region, is defined. The choice of an OFF region much larger than the ON region is wise because it allows for a more accurate determination of the background. To produce maps, a method used in H.E.S.S. to provide the number of counts in the OFF region, N_{OFF}, and estimate the background is called the **ring-background method** and is illustrated Figure 2.5. For each observation run, a ring is defined for each pixel in the field of view, and the number of events found in this ring gives N_{OFF}. If known sources are present in the field of view, they are masked to avoid any contamination as shown in the map (c) of Figure 2.6. The ring can be defined with a fix size and thickness for all pixels in the field of view, or can be made adaptive. In the later case, if part of the field of view is masked by an exclusion region, the ring

will extend automatically to fulfill a criteria on the parameter α: it accounts for the difference in exposure time, zenith angle, acceptance, shape and size between both regions. The requirement is that the acceptance integrated in the ring (but outside exclusion regions) must be more than four times the acceptance integrated at the position of the pixel. For the H.E.S.S. Galactic Plane survey [47], the typical size of the inner ring radius is 0.7°, with constant thickness 0.44°. The inner radius is enlarged to a maximum outer radius of 1.7° if a large portion of the ring area overlaps with exclusion regions to ensure that the OFF region is large enough.

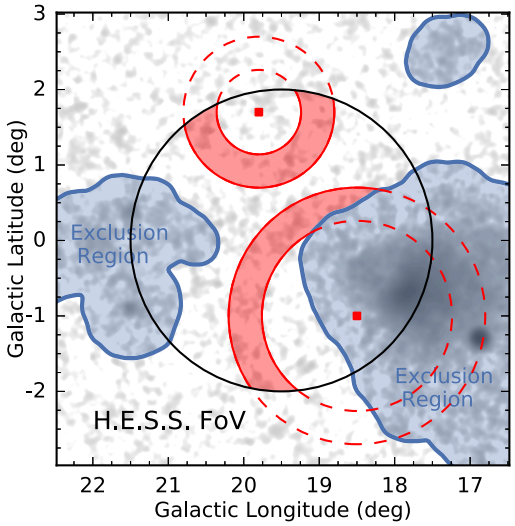

Figure 2.5: Ring-background model used to estimate the background in each pixel of the map. The blue regions are exclusion regions. The red area are the rings defined for both red pixels. For the pixel at the bottom right, the ring needs to be enlarged because of the nearby exclusion region. The black circle is the H.E.S.S. field of view. From [47].

The map (b) of Figure 2.6 is the OFF map where the value in each pixel is the number of counts N_{OFF} in the ring defined for each pixel. Using the parameter α, αN_{OFF} is an estimation of the background. The maps (d) and (e) of Figure 2.6 show a map of the parameter α and a background map. The **excess** is defined as:

$$N_{\mathrm{excess}} = N_{\mathrm{ON}} - \alpha N_{\mathrm{OFF}} \tag{2.1}$$

The map (f) of Figure 2.6 is an excess map of the Crab. A top hat function of radius 0.07° is used to produce the correlated excess map (g). The **statistical significance** of the excess, can be calculated using Li & Ma method [66], that tests how likely it is that an excess comes from a background fluctuation. In first approximation, for a large number of events, it is the ratio of the excess and its standard deviation:

$$N_\sigma = \frac{N_{excess}}{\sigma_{excess}} = \frac{N_{\mathrm{ON}} - \alpha N_{\mathrm{OFF}}}{\sqrt{N_{\mathrm{ON}} + \alpha^2 N_{\mathrm{OFF}}}} \tag{2.2}$$

The map (h) of Figure 2.6 is the significance map of the crab region.

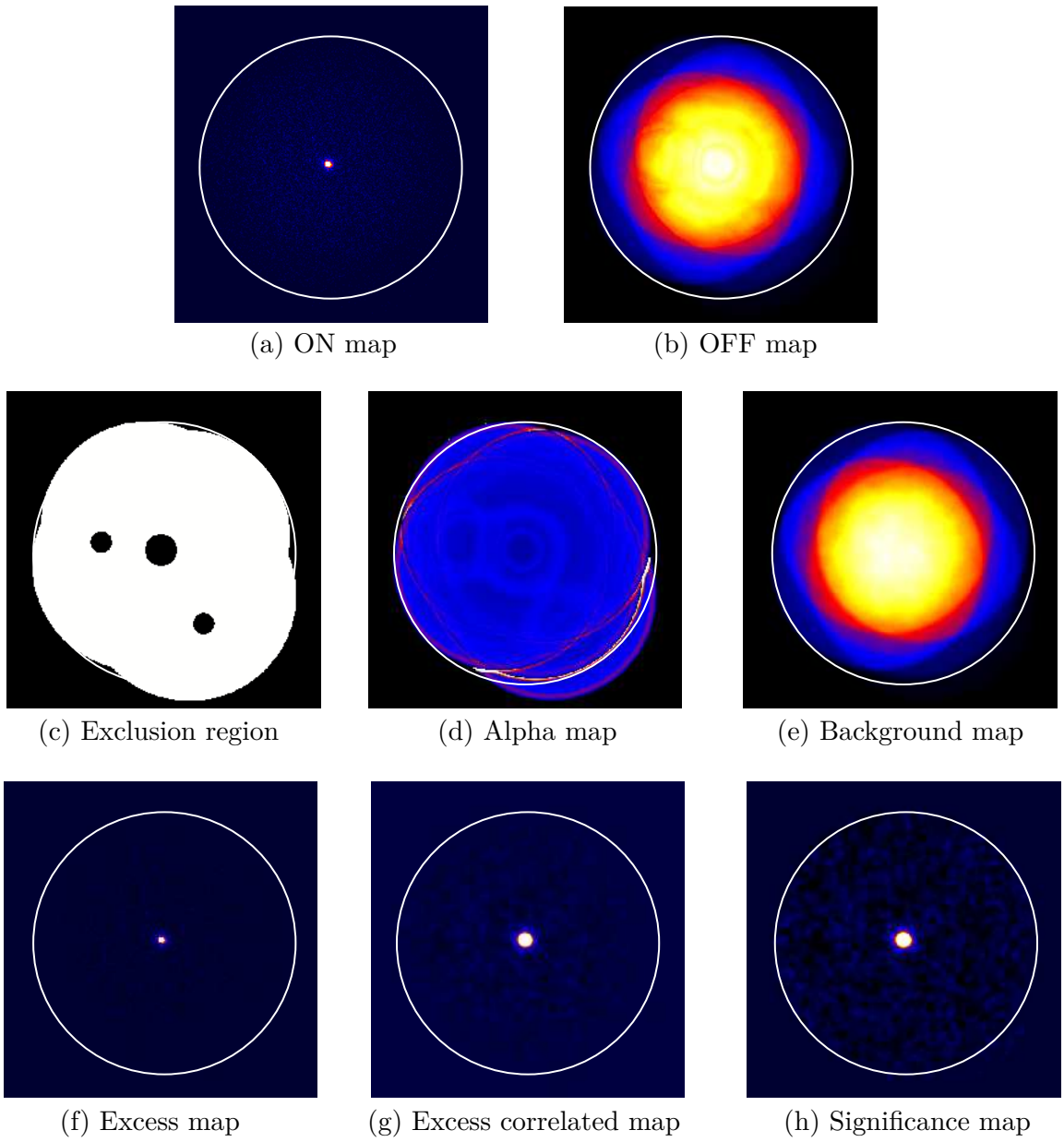

(a) ON map (b) OFF map

(c) Exclusion region (d) Alpha map (e) Background map

(f) Excess map (g) Excess correlated map (h) Significance map

Figure 2.6: H.E.S.S. maps of the Crab using 15 hours of data taken with the four telescopes of H.E.S.S. I. The white circle is the H.E.S.S. field of view of 2.5° radius. (a) is the ON map: it is the number of observed counts in each pixel. (b) is the OFF map: it is the number of counts in the ring associated with each pixel. (c) shows the exclusion regions. (d) is the map of the α parameter for each pixel. (e) is the background map, computed by multiplying the α map and the OFF map. (f) is the excess map computed using equation 2.1 . (g) is the excess map correlated using a top hat function with a correlation radius of 0.07° for point sources. (h) is the significance map computed using equation 2.2.

2.2 The High Altitude Water Cherenkov γ-ray observatory

2.2.1 Instrumentation and data acquisition

The High Altitude Water Cherenkov (HAWC) γ-ray detector is located at an altitude of 4100 m in central Mexico near the volcano Pico de Orizaba (Citlaltépetl) and at a latitude of 19°. Its 300 water tanks, 5 m high and 7.3 m in diameter, are covering an area of 22000 m^2, with a filling factor of 60%. HAWC was under construction between 2013 and 2015. It started operating with a third of the array in August 2013 and is operating in its full configuration since March 2015. A picture of the HAWC array is shown in Figure 2.7. Each tank is instrumented with four photomultiplier tubes (PMT), making a total of 1200 PMTs. A 10" PMT is located at the center of the bottom of each tank and is surrounded by three 8" PMTs. Each water tank is filled with purified water up to 4.5 m, covering the four PMTs with 4.0 m of water, which corresponds to more than 10 radiation lengths. It guarantees that the electrons, positrons, and γ rays from the air shower loose their energy, while producing Cherenkov light, well above the PMT level. High voltage of the order of ~ 1500 V is applied on the PMTs using RG59 coaxial cables. The signals recorded by the PMTs are transferred via the same cables to the counting house in the center of the array where the Front End Board (FEB) amplifies and shapes the PMT pulses. The Time to Digital Converter (TDC) digitalises the pulses using 2 thresholds at 0.25 and 4 photoelectrons. The time at which the pulses cross the thresholds is compared between all the PMTs that have been hit by an air shower and the time differences are used for the direction reconstruction of the shower. Data are constantly read out, the trigger decision is made in the software: a computer gathers synchronised data from the TDCs. Under the trigger condition that 28 PMTs were hit within 150 ns, the full data of the array in a time window of 1500 ns is written to disk. The HAWC trigger rate is of the order of ~ 24 kHz.

Figure 2.7: Picture of the HAWC main array (left) and picture of a water tank (right).

2.2.2 Performance and science cases

HAWC sees most of the Northern hemisphere sky, between -20° and 60° in declination. For sources that transit through its field of view, HAWC typically accumulates 1500–2000 hours per year of total exposure. What makes HAWC unique is its sensitivity at very high energy one order of magnitude better than its predecessor MILAGRO, from a few hundreds of GeV up to several hundreds of TeV. This is due to a larger area, a higher elevation, better reconstruction algorithms and background rejection techniques. Its very wide field of view of 2 sr, and its very high duty cycle higher than 90%, operating night and day, regardless the weather conditions is also a main advantage compared to IACTs. The sensitivity of HAWC peaks around 10 TeV (depending on the source spectrum and declination). Above 10 TeV where photon statistics becomes poor, HAWC achieves better sensitivity than the current generation of IACTs. HAWC achieves in one year a survey sensitivity of ~ 5–10% of the Crab Nebula flux.

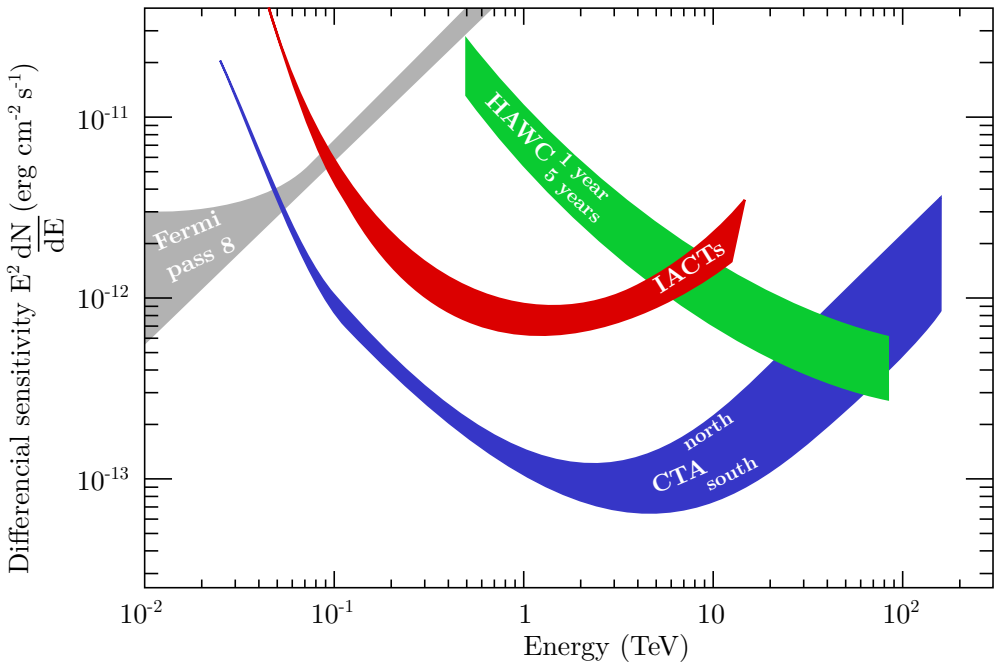

Figure 2.8: Differential point sources sensitivity of HAWC compared to the *Fermi* satellite and to IACTs (MAGIC, H.E.S.S. and VERITAS, CTA for 50 h). Adapted from www.cta-observatory.org/science/cta-performance.

In terms of energy coverage, HAWC is complementary to satellite instrument like the Fermi Large Area Telescope (*Fermi*-LAT) which observes the whole sky in the energy range 200 MeV - 300 GeV. HAWC is also complementary to IACTs, whose energy ranges overlap. However, contrary to HAWC, they have a very small field of view of the order of a few degrees, but an angular resolution better than HAWC: at 1 TeV, the resolution of HAWC is ~0.4° while it is smaller than

0.1° for H.E.S.S. The HAWC angular resolution and energy resolution are visible in Figure 2.10. The performance of HAWC was assessed with observations of the Crab nebula [8].

The HAWC detector is an instrument dedicated to the observation of Very High Energy (VHE; $E > 100$ GeV) γ rays. A milestone in the scientific achievement by the HAWC collaboration was the publication of its catalogue of sources [7] using 507 days of data, showing the detection of 39 TeV γ-ray sources, 16 of them being not associated with any known TeV source from previous catalogues. HAWC is particularly suited for the detection and the observation of extended galactic γ-ray sources such as Pulsar Wind Nebulae (PWN) and Supernova Remnants (SNR). A good example is Geminga, that was discovered by Milagro. The TeV emission region is several degrees across and was attributed to electrons and positrons diffusing away from the pulsar and upscattering the cosmic microwave background photons [5].

Taking advantage of its wide field of view and continuous observation of the sky above it, it is a survey instrument that can continuously monitor sources [4]. This makes it sensitive to flaring objects [10] and γ-ray bursts (GRB) [22] and it can rapidly emit alerts to pointing instruments like IACTs. The HAWC collaboration also studies extended diffuse emission regions like the galactic plane or the Fermi Bubbles [9]. The search for dark matter signature is also performed [18] [19]. Finally, HAWC is involved in multimessenger detection. *Fermi* showed for a recent binary neutron star merger event, for which the Advanced LIGO and Advanced Virgo detectors detected gravitational waves, that γ-ray counterparts can be observed [1]. For this particular event the Fermi Gamma-ray Burst Monitor (GBM) observed coincidentally a γ-ray burst. HAWC could only derive upper limits, but future event producing gravitational waves could be observed in γ rays by HAWC. Moreover, HAWC has been involved in looking for a γ-ray counterpart to the neutrino event IceCube-170922A [55], which was coincident with a known γ-ray blazar, TXS 0506+056, observed to be in a flaring state by the Fermi-LAT. Again, HAWC derived upper limits for this event.

2.2.3 Data analysis

The HAWC data are analysed and reconstructed using the analysis version known as Pass 4. For each event, the amount of charge and the hit time of the signal are recorded for all PMTs. These two pieces of information are used to reconstruct the characteristics of the showers, their core and direction, the type of primary particle, and to assign them to an energy bin. For illustration, an event recorded by the HAWC detector is displayed in Fig. 2.9. It shows the **footprint** of the shower on the detector.

Core and direction reconstruction

First, a core fitter analyses the lateral distribution of the pulse amplitude and identifies the most likely location of the core, where the energy density is the highest in the shower footprint. It corresponds to the location on the ground where the primary particle would have landed if

it would have made it to the ground. It is marked by the red star on the event displayed in Figure 2.9.

Then the lateral distribution of the hit time is fitted to derive the angles characterising the direction of the shower. In Fig. 2.9, the color gradient illustrates the propagation of the shower front and hence the direction of the shower. The direction defines the location in the sky where the primary particle was coming from, and in the case of a γ ray points to its astrophysical origin.

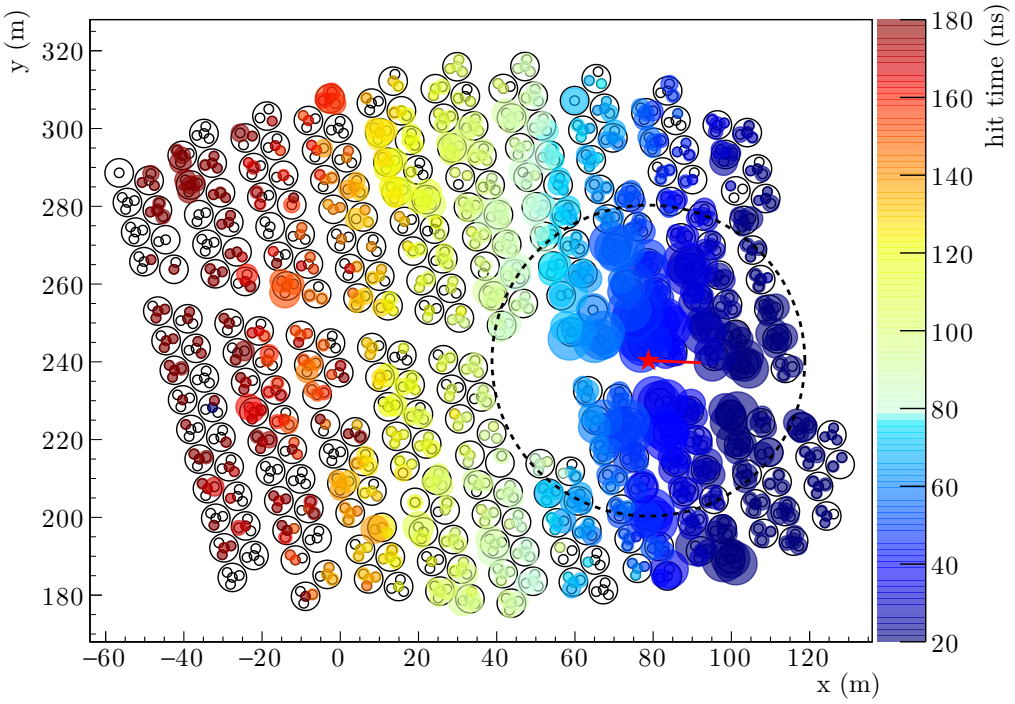

Figure 2.9: A ~ 40 TeV event recorded by the HAWC detector. The color is the arrival time of the shower particles at each PMT and the size of the circles represent the amount of charge recorded by the PMTs. The reconstructed core of the shower is highlighted by the red star, and the direction by the red line. The dotted circle represents the 40 m region around the shower core.

Energy estimation

Regarding the energy, in the standard HAWC analysis, events are classified with respect to the fraction of the main array that was triggered by an event. They are assigned to one of the 9 nHit bins, from nHit bin 1 gathering events triggering 7 to 10% of the array, to nHit bin 9 for events hitting 84 to 100% of the array. Table 2.1 and Figure 2.10 give the characteristics of each bin. This binning can be seen as an energy proxy, since small events triggering only a small fraction of the array are likely to have lower energy than big events triggering most of the array. However, although a median energy can be assigned for each bin, there is a large overlap between them.

B	$fhit$ (%)	ψ_{68} (°)	E_γ^{MC}	Crab excess per transit
1	6.7 - 10.5	1.03	0.7	68.4 ± 5.0
2	10.5 - 16.2	0.69	1.1	51.7 ± 1.9
3	16.2 - 24.7	0.50	1.8	27.9 ± 0.8
4	24.7 - 35.6	0.39	3.5	10.58 ± 0.26
5	35.6 - 48.5	0.30	5.6	4.62 ± 0.13
6	48.5 - 61.8	0.28	12	1.783 ± 0.072
7	61.8 - 74.0	0.22	15	1.024 ± 0.053
8	74.0 - 84.0	0.20	21	0.433 ± 0.033
9	84.0 - 100.0	0.17	51	0.407 ± 0.032

Table 2.1: Characteristics of the 9 nHit bins. Each bin is defined by the fraction of the array hit $fhit$. It is characterised by its corresponding 68% PSF containment ψ_{68} (cf. Figure 2.10 (b)). Its median energy E_γ^{MC} (cf. Figure 2.10 (a)) is obtained for simulated γ-ray photons from a reference source of spectral index -2.63 at a declination of 20°. The last column gives the number of excesses coming from the Crab per transit falling in each bin [8].

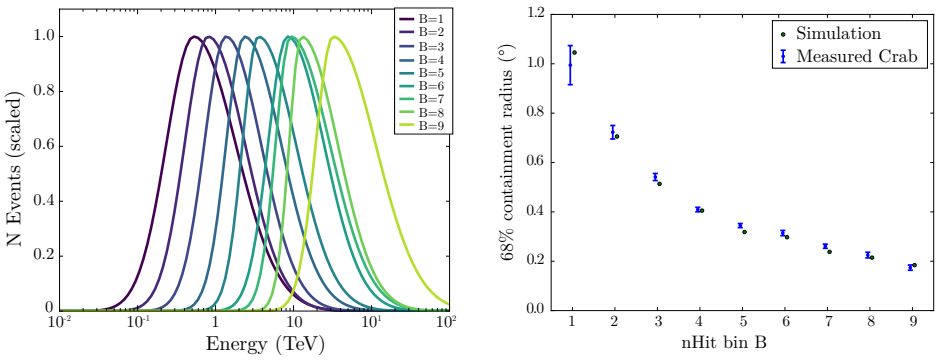

(a) (b)

Figure 2.10: (a) Fits to the true energy distribution of photons from a source with a spectrum of the form $E^{-2.63}$ at a declination of +20° N for nHit bin B between 1 and 9, summed across a transit of the source (normalised for display). (b) Measured angular resolution required to contain 68% of the photons from the Crab, as a function of the nHit bin B compared to expectations from simulations. From [8].

Gamma/hardon separation

Figure 2.11 shows the footprint of a hadronic shower (right) and a γ-ray shower candidate (left). To discriminate γ and cosmic rays, selection cuts based on shower morphology are used. The first cut is based on how much charge has been deposited further than a certain distance from the shower core. This parameter is called *compactness* and is defined by the fraction of hits detected outside a region of a given radius, in general 40 m, from the reconstructed shower core:

$$\mathscr{C} = \frac{\mathrm{N}_{hit}}{\mathrm{CxPE}_{40}} \tag{2.3}$$

where N_{hit} is the total number of hit PMTs in a shower and CxPE_{40} the effective charge recorded outside a region of 40 m radius around the shower core.

A second parameter called *PINCness*[3] describes how clumpy the lateral distribution of the shower is, as depicted in Figure 2.12 . In other words, if there are clumps of charge deposition away from the shower core due to particles like muons carrying a lot of energy to the ground, it is the sign for a hadronic shower.

$$\mathscr{P} = \frac{1}{N}\sum_{i=0}^{N}\frac{(\zeta_i - \langle\zeta_i\rangle)^2}{\sigma^2_{\zeta_i}} \tag{2.4}$$

where $\zeta_i = \log_{10}(Q_{\text{eff}}, i)$ for each PMT i that measured an effective charge Q_{eff}, $\langle\zeta_i\rangle$ is an average of ζ_i in all PMTs in an annulus containing the PMT i centered at the core of the shower and with a width of 5 meters.

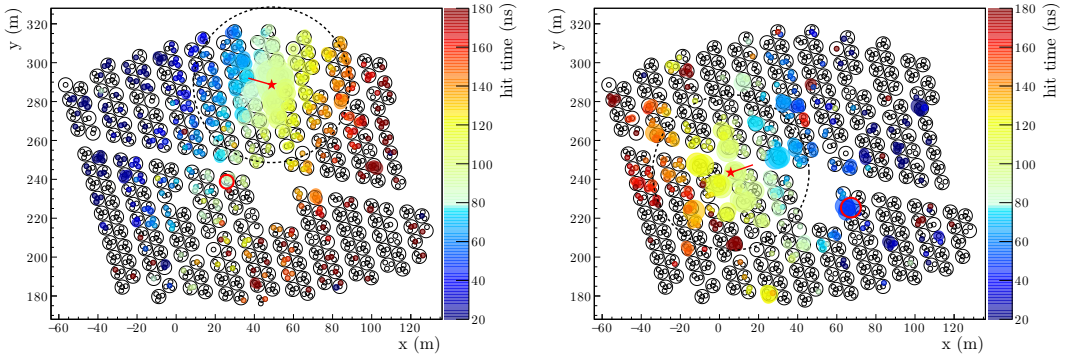

Figure 2.11: Footprint of a γ-ray shower candidate (left) and a cosmic-ray shower (right). Cuts based on their morphology is used to distinguish them. A dense and compact core region, in the dotted circle, and a smoothly decreasing charge deposition with distance from the core characterise the γ ray shower. A very clumpy shower, with isolated high energy deposition points away from the core is the sign for a cosmic ray shower.

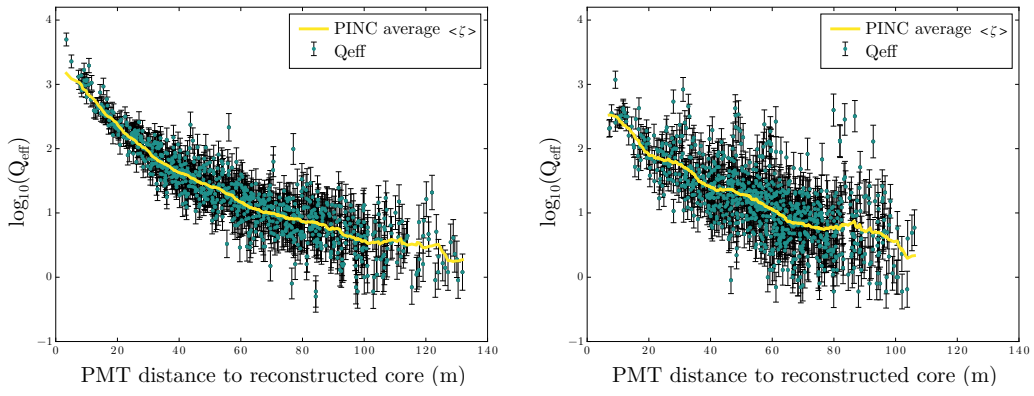

Figure 2.12: Lateral distribution function of a γ-ray candidate (left) and a cosmic ray from the crab nebula (right). Each of the PMT hits has a measured effective charge Q_{eff}. For each hit, the logarithm of the charge $\zeta = \log_{10}(Q_{\text{eff}})$ is calculated and averaged in all PMTs contained in an annulus containing the hit, with a width of 5 meters, centered at the core of the air shower (yellow curve). Adapted from [8].

[3]PINCness is the short version of Parameter Identifying Nuclear Cosmic rays

Figure 2.13 shows the efficiency of γ/hadron separation for simulated γ rays and the measured efficiency for hadronic background after the cuts presented above as a function of the nHit bin. It is 1 to 2 orders of magnitude better for nHit bins above 6 than the first bins.

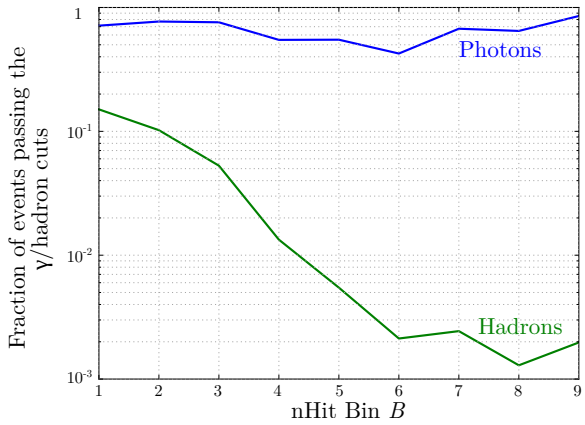

Figure 2.13: Fraction of simulated γ rays and measured background hadron events passing the γ/hadron cuts as a function of the nHit bin B [8].

Background estimation

After γ/hardon separation, the remaining background is estimated using the **direct integration method**[4]. An acceptance map $E(ha,dec)$ is built by adding events to a local map (binned in ha,dec) as illustrated in Figure 2.14, normalised to 1 at the end of each period of 2 hours. It can be interpreted as the sensitivity of the detector, depending on the position on the sky. Typically, HAWC is more sensitive to events coming from zenith, and it degrades smoothly up to the horizon. This acceptance map is convolved with the event rate $R(t)$ of the whole sky with the exception of known γ-ray sources and integrate over a period of time, here 2h :

$$N_{\text{bkg}}(ra,dec) = \int R(t)E(ha,dec)dt = \int R(t)E(t-ra,dec)dt$$

To avoid any contamination, know γ-ray sources are excluded, namely the Crab, the two Markarians and the Geminga region as well as a region of $\pm 3°$ around the Galactic Plane. Two assumptions are made here: first, the acceptance of the detector is a function of the local coordinates: its shape does not vary over the integration period (typically 2h) and it is independent of the trigger rate over this period. Secondly, the background produced by cosmic rays is assumed spatially isotropic. Moreover, the period of 2 hours allows for sufficient statistics while minimising the systematic errors coming from the possible change in the acceptance over long periods of time. This duration is fine for the low nHit bins. However, for the highest bins, the number of events is much lower, since the cosmic ray flux decreases rapidly with energy and the γ/hadron separation becomes

[4]Internal HAWC documentation available at
https://private.hawc-observatory.org/hawc.umd.edu/internal/doc.php?id=2347

better. Hence, the direct integration background map is averaged over 0.5°. Tests made on simulations shows that it does not affect significantly the background estimation. Figure 2.15(a) is a data map for 1128 days. The value in each pixel give the number of events from the corresponding location in the sky. Map (b) is the corresponding background map using the direct integration method. The maps are produced using a HEALPix[5] pixelisation scheme [45], where the sphere is divided in 12 equal area base pixels. Each of them is subdivided into a grid of $N_{side} \times N_{side}$. For the analysis presented in this thesis, maps uses $N_{side} = 1024$ corresponding to a mean spacing between pixel centers of less than ~0.06°.

Using these maps, a test statistic (TS) is computed which compares the likelihood that a source is present against the hypothesis that there is no source but background fluctuations only:

$$TS = 2 \ln \frac{\mathscr{L}(\text{source model})}{\mathscr{L}(\text{no source})} \tag{2.5}$$

TS maps are performed under one of the following hypotheses: a point source and a power law with spectral index -2.7 or an extended source represented by a disk of radius 0.5°, 1° or 2° and a power law with spectral index -2.0 [7]. The TS map is done by scanning all the possible source positions in the sky. The square root of TS is called significance. We define 1σ significance as the standard deviation of the Poisson distribution, meaning that a source is not a background fluctuation with 68% probability. A detector response is also needed. It is computed using Monte Carlo simulation of γ rays and cosmic rays, assuming the shape and the spectral parameter of the source mentioned previously and the instrument PSF. It gives the angular response of the detector. Figure 2.16 shows an excess map, which is the difference between the number of events in the data map and the number of background events, and a significance map. The galactic plane is barely visible on the excess map but is visible very clearly on the significance map.

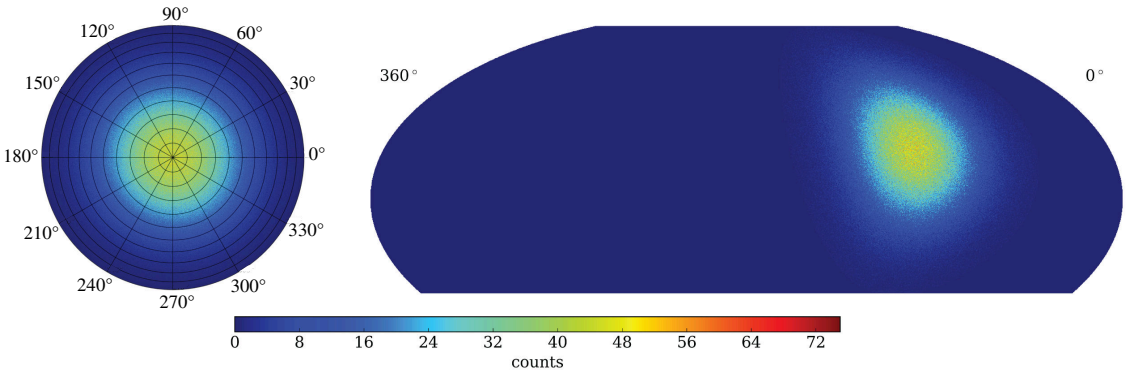

Figure 2.14: Events have been accumulated for 2 hours, reconstructed and displayed: the left map is the local map above HAWC, projected to a whole sky map to give the right map. The zenith coordinates (0°,0°) in the middle of the left map corresponds to HAWC location on the right map (-lon=97.26°, lat=19.03°).

[5]HEALPix stands for Hierarchical Equal Area isoLatitude Pixelisation

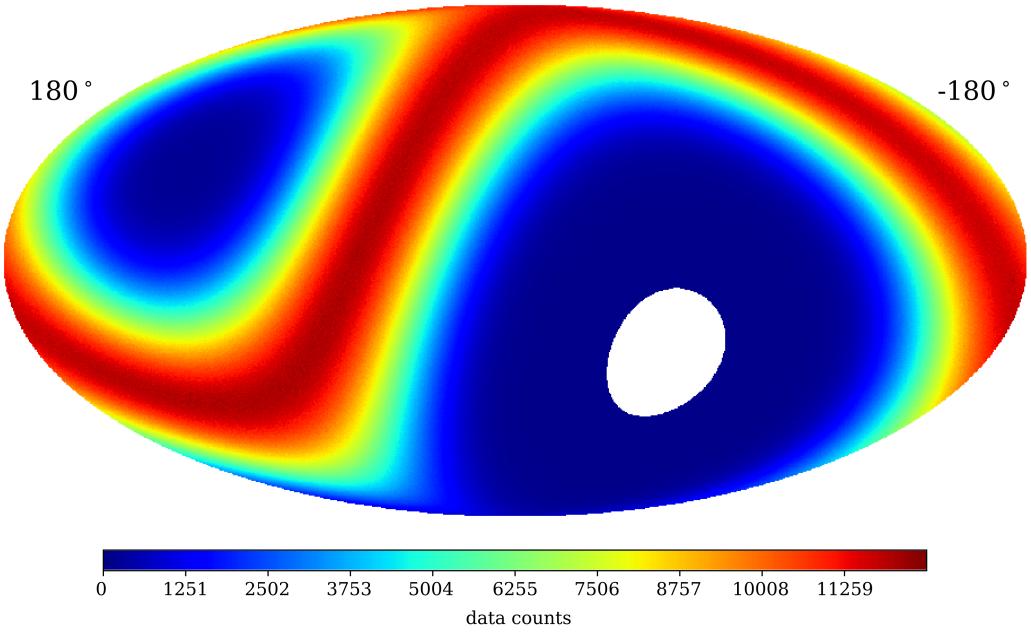

(a)

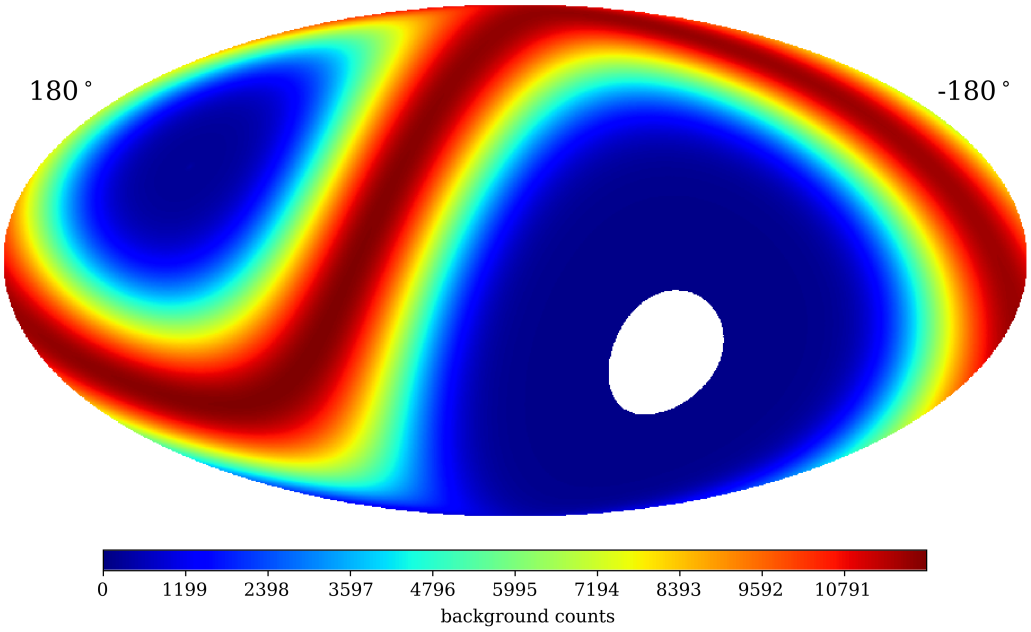

(b)

Figure 2.15: HAWC data map (a) and background map (b) in galactic coordinates for 1128 days of data using nHit bins 1 to 9.

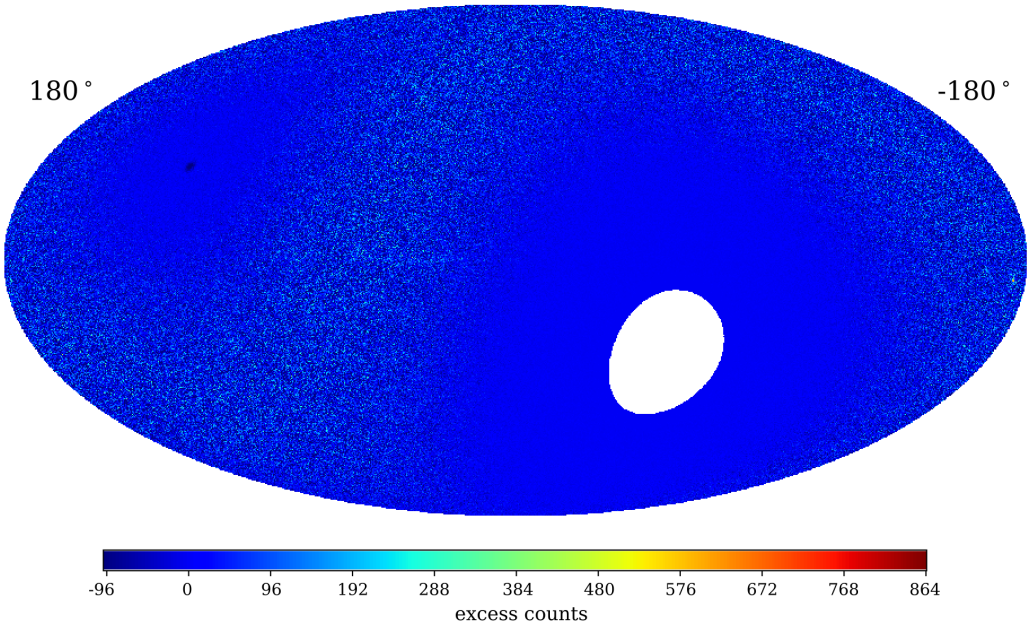

(a)

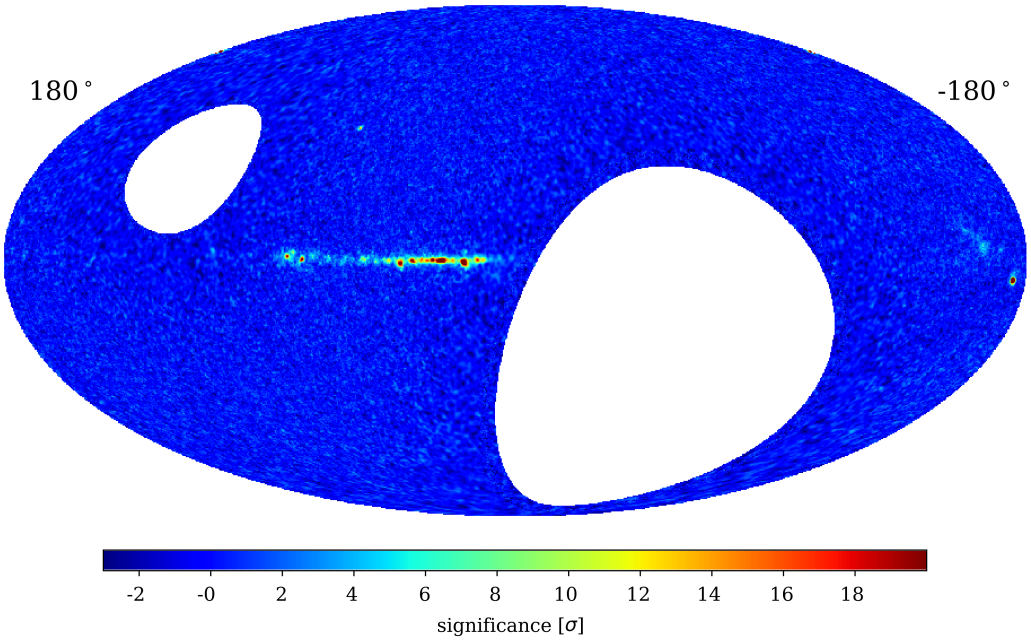

(b)

Figure 2.16: HAWC excess map (a) and significance map (b) in galactic coordinates for 1128 days of data using nHit bins 1 to 9.

CHAPTER 3

HAWC HIGH ENERGY UPGRADE WITH AN OUTRIGGER ARRAY

A major upgrade to the HAWC observatory has been recently performed. It consists of a sparse array of smaller water Cherenkov detectors surrounding the main array. For this reason it is called the **outrigger array** and is aimed at improving the observatory performance at the highest energies.

Calibration is an essential and necessary step to operate any instrument. This chapter focuses on the charge amplitude and timing reconstruction of the outrigger signals. The outrigger array has been designed with a different philosophy than the main array and needs its own calibration. A procedure has been developed using a laser system and was tested on-site with the first outrigger prototypes, with a partial array and finally implemented on the whole array. The electronics, readout system and synchronisation were also extensively tested. Since the whole array can be operated remotely, the monitoring of some parameters over time is possible to ensure of the good working conditions of the array.

3.1 Introduction on the outrigger array

The outrigger array has been completed and is now under commissioning. This section describes the needs that led to this upgrade, the design of the array as well as all the electronics components.

3.1.1 Motivation

The HAWC detector main array, and its 300 densely packed water tanks, is limited at the highest energies by its finite size of ~150 m by 150 m. An air showers above ~10 TeV have a footprint bigger than the size of the main array. If the core of the shower falls inside the main

array, it can be reconstructed correctly. In the case where the core of the shower is outside the main array, it can be wrongly interpreted as a shower of lower energy, with a wrong core location and a wrong arrival direction. To illustrate this, the sketch in Figure 3.1 shows that a high energy shower (red) with the core (red star) falling far away from the main array looks very similar to a low energy shower (green) which core (green star) falls on the edge of the main array, from the main array point of view. Hence, the core location, the arrival direction and the energy of the primary particle may be wrongly reconstructed. To overcome the mis-estimation of the high energy shower parameters, the idea is to add, around the main array, smaller water tanks, to record the missing information for showers with energy above ~10 TeV falling partially outside the main array. Because we are aiming at assisting the main array for the highest energy showers, and improving HAWC performance at multi TeV energies, these tanks do not need to be as big and as close to each other as the ones of the main array. Hence, they are sparsely distributed over an area 4 times the size of the main array [81] [57]. An outrigger tank and a main array tank are sketched to scale in Figure 3.1.

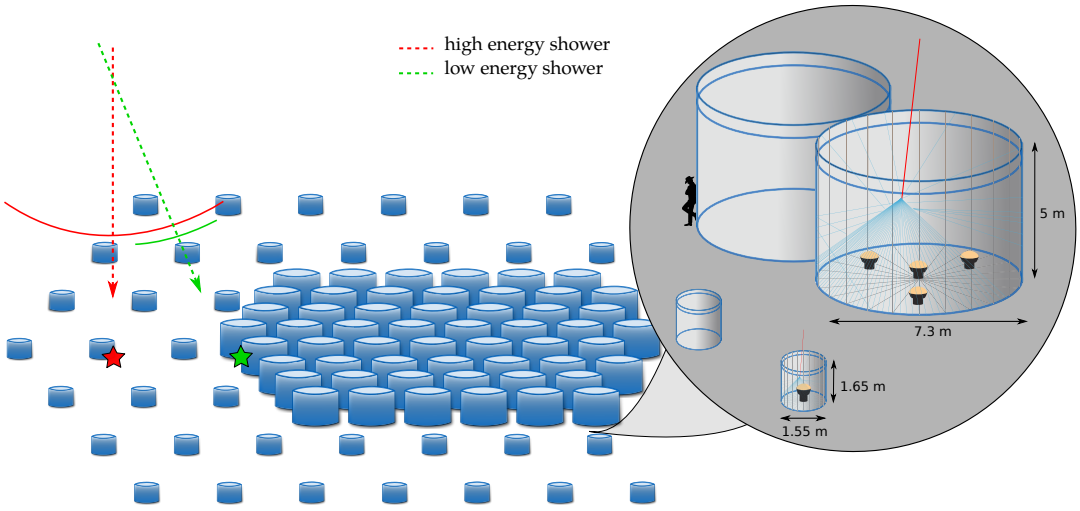

Figure 3.1: Sketch of the outrigger array around the main array tanks: from the main array point of view a high energy shower (red) and a low energy shower (green) may look similar leading to a mis-reconstruction of the core and the direction of the shower. In the bubble, an outrigger tank is sketched to scale next to a main array tank (PMTs not to scale).

3.1.2 Outrigger array layout

The outrigger array consists in 345 small water tanks, 1.65 m high and 1.55 m in diameter, around the main array. They are separated by 12 to 18 m from each other. The outrigger array is divided into five independent sections named from A to E for readout purposes. They are highlighted by the red lines on Figure 3.2(a). In each section, a **node** gathers all the electronics

needed for the section to be functional. A picture of the electronics of node A is visible in Figure 3.2(b).

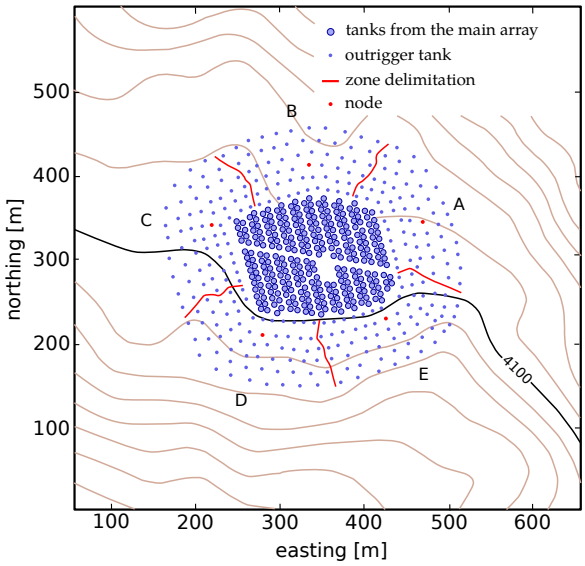

(a)

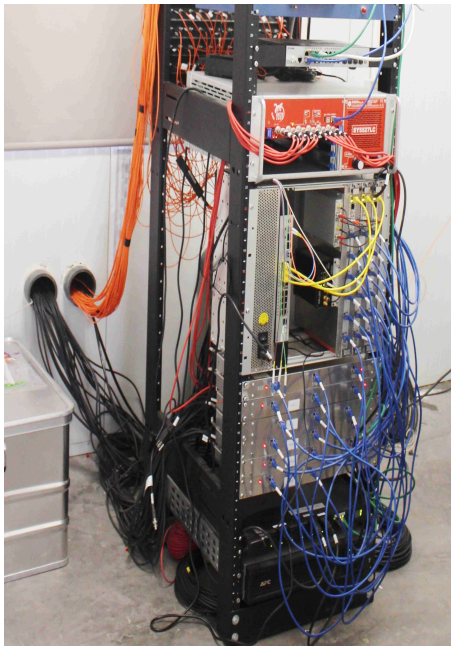

(b)

Figure 3.2: (a) Layout of the outrigger array. The big blue densely packed circles in the middle represent the main array tanks. The small blue circles sparsely distributed around it are the outrigger tanks. They are divided into 5 sections, named by a letter from A to E, delimited by the red lines. The red dots represent the nodes, where all the electronics needed to operate each section individually is gathered.
(b) Picture of the electronic devices inside a node. The orange fibres are optical fibres that carry laser light to each outrigger tank. On the front, the red cables are carying the high voltage to back of the pick-off modules. The black cables are RG-59 coaxial cables that carry the high voltage and the signal to and from each PMT. They are connected at the back of one of the six pick-off modules. The blue Ethernet cables carry the signal from the pick-off module to the FADC cards. The yellow Ethernet cables send the data from the FADC to the main server.

3.1.3 Outrigger deployment

The outrigger array deployment started as soon as the permit was signed by the Mexican government, in September 2017. First the tanks were placed in the field at their final location, then filled with purified water, and finally equipped with a PMT and an optical fibre used for calibration. The whole deployment took approximately one year, as shown by the plot in Figure 3.3(a), which shows the progress of the tanks deployment with time. Meanwhile, the five nodes where installed in the middle of each of the five outrigger sections. Figure 3.3(b) shows the installation of a PMT in an outrigger tank. The pictures in Figure 3.4 shows the outrigger array fully deployed around the main array.

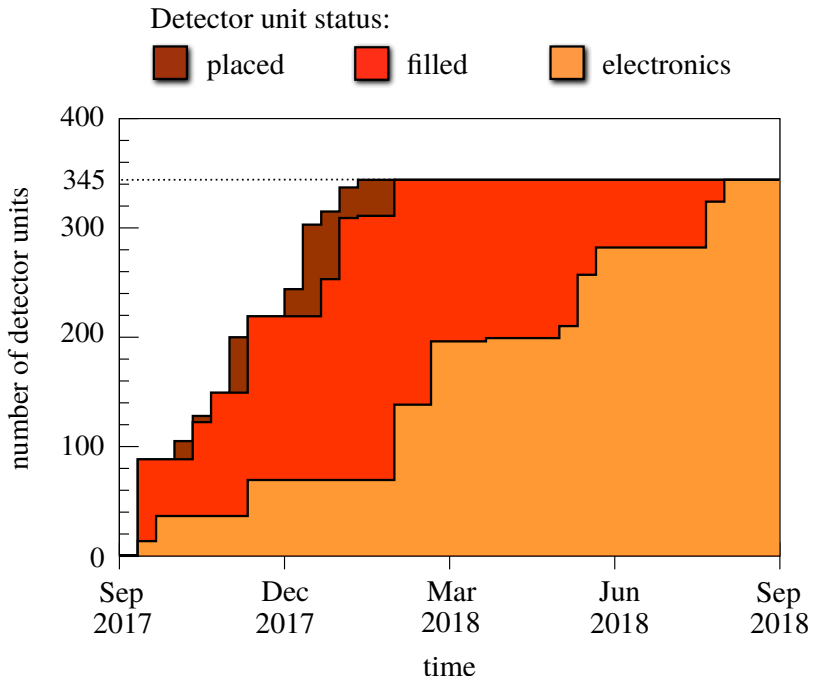

(a)

(b)

Figure 3.3: (a) Evolution of the outrigger array deployment between September 2017 and September 2018 (credit: Harm Schoorlemmer, MPIK Heidelberg). (b) Installation a PMT into an outrigger tank.

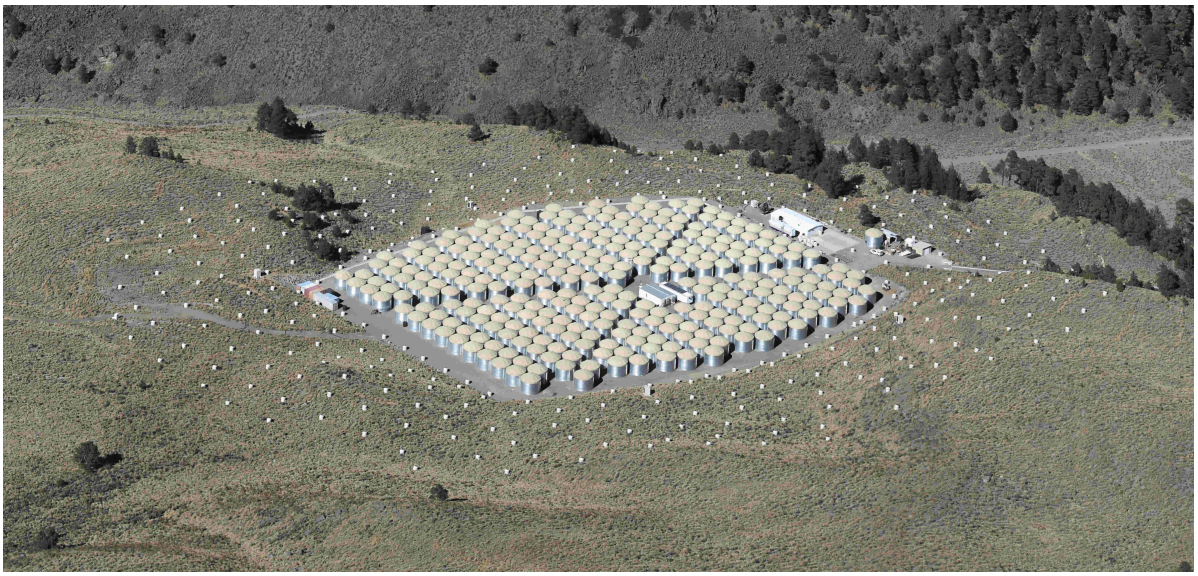

(a)

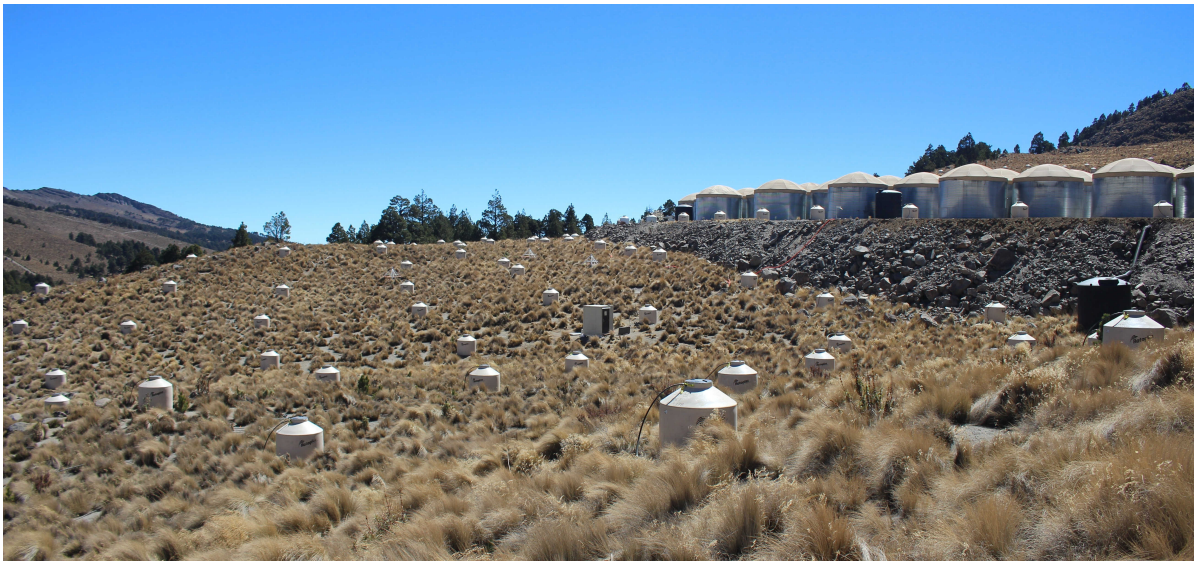

(b)

Figure 3.4: Pictures of the newly installed outrigger array around the HAWC main array. (a) Picture taken from the Sierra Negra volcano, 500m above HAWC. (b) Picture of section B. Node B is visible at the centre of the picture.

3.2 Electronics

3.2.1 Light sensor

Photomultiplier tubes (PMT) are widely used in astroparticle physics. There are different types of PMTs, but all have the same principle: convert a light signal into an electric signal and amplify it. Each outrigger tank is equiped with one **Hamamatsu R5912 8" photomultiplier tube**, identical to the three 8" PMTs in each of the main array tanks[1]. They were chosen for their large effective area and their large dynamic range.

A PMT consists of a photocathode to convert incoming light. For the PMT considered here, the photocathode is made of a bialkali material that, when excited by a photon, emits via the photoelectric effect, electrons called **photoelectrons** (PE). They are emitted in a vacuum tube where electrodynodes at different electrical potentials accelerate them and multiply them, producing secondary electrons in cascade. After the last electrodynode, all the secondary electrons are collected by the anode. Inside the tube, the electron trajectories, determined by the electric field and hence the electrodynode configuration as well as the voltage applied, are optimised to minimise the transit time jitter. As illustration, a schematics of a HAWC PMT is depicted in Figure 3.5. A picture of one of these PMTs being encapsulated to make it water tight, and a picture of the base are also shown in Figure 3.6. The important values of the parameters described here, taken from the Hamamatsu data sheet[2], are gathered in Table 3.1.

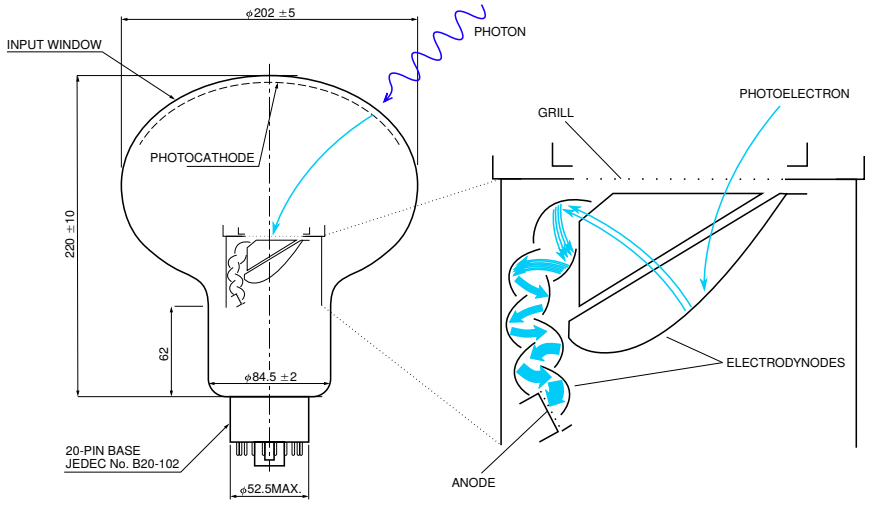

Figure 3.5: The left schematic is a HAWC R5912 8" photomultiplier tube (credit: Hamamatsu Photonics K. K). The right schematics shows the principle of electron amplification within such a PMT of type box-and-line.

[1]Internal HAWC documentation at https://private.hawc-observatory.org/hawc.umd.edu/internal/db/2222_01.pdf
[2]The full datasheet for this PMT can be found at http://pdf.datasheetcatalog.com/datasheet/hamamatsu/R5912.pdf

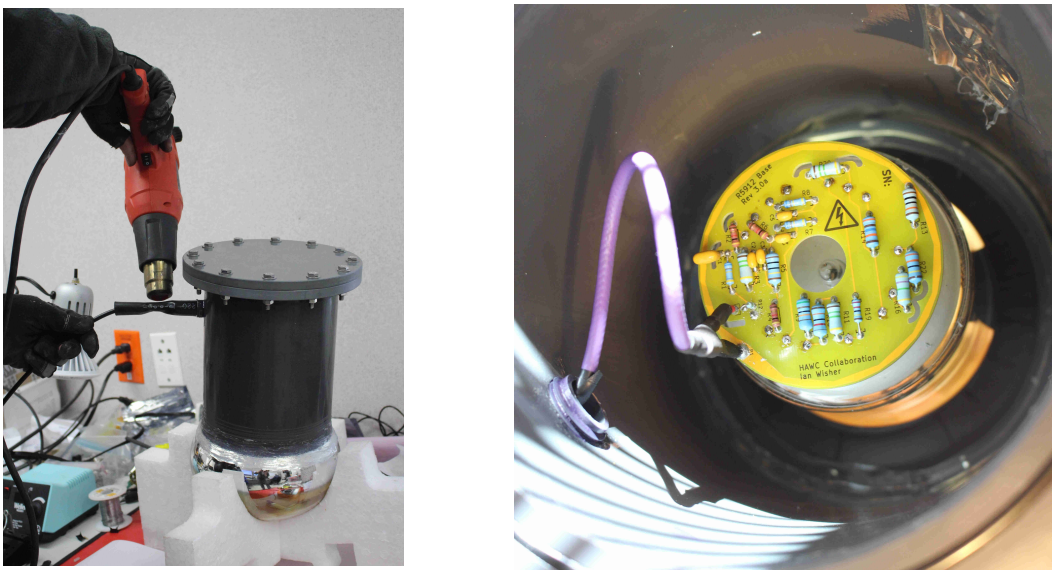

(a) (b)

Figure 3.6: (a) Picture of the HAWC PMT while being made water tight. (b) Base of the PMT.

A PMT is characterised by several parameters [82]:

- The photocathode composition determines the wavelength range of the PMT **sensitivity**, meaning its efficiency to convert incident photons into photoelectrons. Its variation with the incident light wavelength, is described by the **spectral response characteristics**. It depends on the quantum efficiency and the collection efficiency. Figure 3.7 shows the spectral response of an outrigger PMT. It peaks around 400 nm, and is therefore sensitive to Cherenkov light.

- The emission of a photoelectron is a probabilistic process described by the **quantum efficiency** that depends on the photon wavelength. It is the ratio between the number of emitted photoelectrons from the photocathode and the number of incident photons. For the HAWC PMTs, it is of the order of 25% in the wavelength range for Cherenkov light. Figure 3.7 shows the quantum efficiency as a function of wavelength.

- The probability that photoelectrons emitted by the photocathode create a detectable signal depends on the **collection efficiency** of each dynode, noted α_i. Some electrons that do not hit the useful area of a dynode may be lost or be **under-amplified** leading to an excess noise factor. The collection efficiency is usually 60 to 90 %. It is optimised by designing carefully the shape of the photocathode, and by means of focusing electrodes whose arrangement and shape optimise the trajectory of the emitted photoelectrons from the photocathode to the dynodes. The electric field between the dynodes can be adjusted by the voltage divider on the base of the PMT, as visible in Figure 3.6(b).

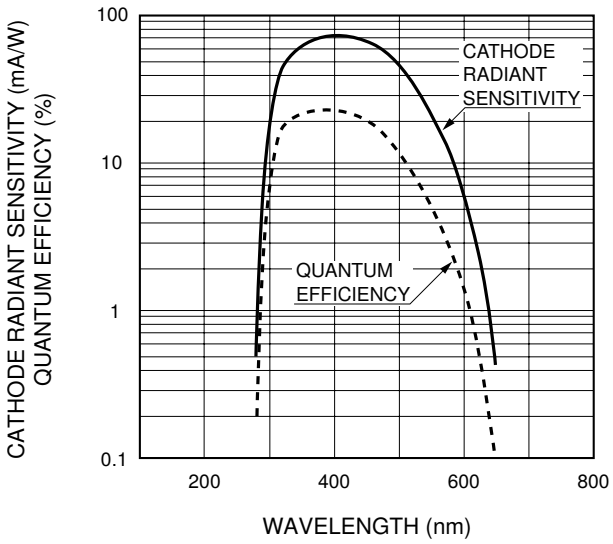

Figure 3.7: Typical spectral response of an outrigger PMT: sensitivity and quantum efficiency as a function of wavelength (credit: Hamamatsu Photonics K. K).

- The **excess noise factor** (ENF) is a measure of the deviation of the observed photodetector resolution to the expected resolution based on Poisson statistics. It is caused primarily by noise added during each step of the multiplication process by the dynode stages, and by under-amplified electrons.

- The charge amplification from the photocathode to the anode is the **gain**, noted η. It is the ratio of the anode charge Q_a and the photocathode charge Q_p, which is equal to the product of the collection efficiency α_i and the amplification factor of each dynode δ_i:

$$\eta = \frac{Q_a}{Q_p} = \prod_{i=1}^{n} \alpha_i \delta_i \quad \text{where} \quad \delta_i = \frac{Q_i}{Q_{i-1}} \tag{3.1}$$

  It depends on the high-voltage ($\propto$ HV^a) with $a \simeq 0.6 - 0.8$ typically) because a higher HV implies a higher electric potential and hence a higher amplification factor. Typically, Hamamatsu specify a gain of 1.10^7 electrons for a supply HV of 1500V for this PMT and this is also roughly the gain and HV at which the HAWC PMTs are operated.

- The PMT response to very weak signal is very important since HAWC trigger and analysis makes use of pulses from individual photoelectrons. Single PE can produce pulses with a distribution of amplitude called the **single photoelectron spectrum**. One of HAWC outrigger PMT was tested under lab conditions and the expected single photoelectron spectrum measured. Figure 3.8 shows that the spectrum we obtained (red) is narrower than the one measured by Hamamatsu, probably because of our custom base that increases the voltage of the first dynode.

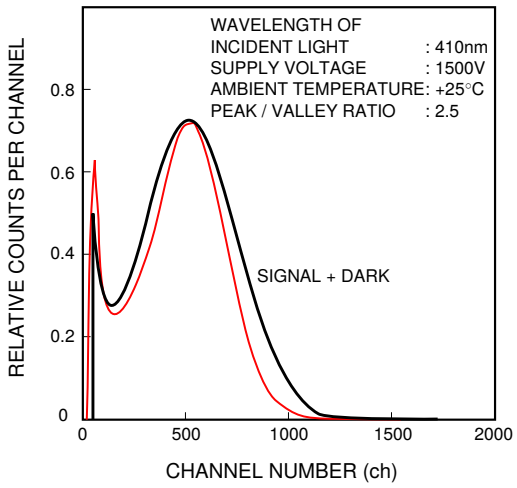

Figure 3.8: Single photoelectron spectrum for an outrigger PMT from Hamamatsu (black, credit: Hamamatsu Photonics K. K) compared with our measurements in the lab (red).

- The PMT time response is characterised by the **transit time** needed for the PEs emitted from the photocathode to produce a signal at the anode after being accelerated and multiplied. It depends on the HV: the electron transit speed is improved with increasing HV, and the transit time shortens by a factor inversely proportional to the square root of the supply voltage. The fluctuation of the transit time is known as the **transit time jitter**. It is usually expressed as the FWHM as shown in Figure 3.9 or the standard deviation of the transit time distribution, depending on the convention[3]. The time resolution improves as the number of PEs per pulse increases, inversely to the square root of the number of PEs.

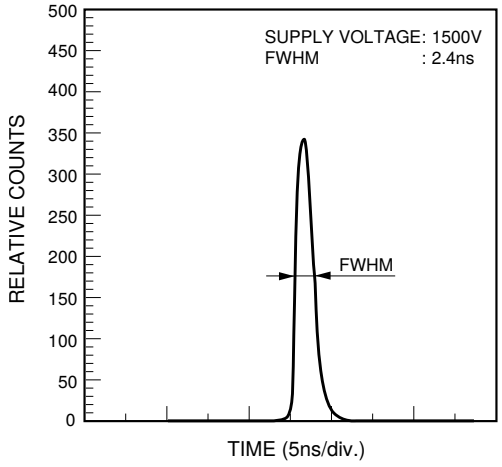

Figure 3.9: Transit time jitter for an outrigger PMT (credit: Hamamatsu Photonics K. K)

[3]If time transit histogram is a Gaussian distribution, the FWHM is 2.35 times the standard deviation.

- The **dynamic range** is the range of incident light level measurable by the PMT.

- The dependence on the angle between the incident light and the PMT is the PMT **angular response**[4]. Commonly, the photocathode sensitivity improves at larger angles of incidence and is larger at longer wavelengths, within the wavelengths range sensitivity of the PMT.

- PMT pulses can be followed by **late pulses** or **after pulses**[5]. Late pulses are produced by electrons that were back scattered from a dynode, and re-accelerated, producing secondary electrons reaching the anode with a delay. According to Hamamatsu documentation they are expected to happen with a probability of 1.5% and have a characteristic delay of 8 to 60 ns after the main pulse. A typical late pulse is of the order of 1 PE. On the other hand, after-pulses occur when a photoelectron emitted from the cathode ionises a residual gas atom inside the PMT. The ionized nucleus is accelerated toward the cathode and produces one or more photoelectrons which then produces another signal. They are expected to happen with a probability of $\sim 2\%$ and have a characteristics delay of 100 ns to 16 μs after the main pulse. A typical after-pulse is a 1 to 10 PE signal.

- Even when a PMT is completely in the dark, it produces **dark noise**, mainly due to thermal fluctuations, that results in a similar signal to a photoelectron from the photocathode. A dark rate can be defined as the signal rate while the PMT is in the dark, measured after some adaptation period, typically 2 hours. For a HAWC PMT it is of the order of 4 to 8 kHz.

Parameter	typical value
Spectral response	300 - 650 nm
Wavelength at maximum response	420 nm
Quantum efficiency at 390 nm	25%
Gain	1.10^7 electrons
Supply voltage for gain of 1.10^7 electrons	1500 - 1800 V
Dark counts (after 15 h in darkness)	4.10^3 - 8.10^3 Hz
Electron transit time	55 ns
Transit time jitter (FWHM)	2.4 ns
Late pulse	8 - 60 ns after the main pulse
After pulse	100 ns - 16 μs after the main pulse

Table 3.1: Typical parameters of a Hamamatsu R5912 8" PMT (credit: Hamamatsu Photonics K. K).

[4]Internal HAWC documentation available at https://private.hawc-observatory.org/hawc.umd.edu/internal/db/2321_01.pdf
[5]Internal HAWC documentation available at https://private.hawc-observatory.org/hawc.umd.edu/internal/db/2186_01.pdf

3.2.2 Node electronics

Figure 3.4(b) shows a picture of the electronics inside a Node. Figure 3.10 shows a schematic of all the elements and how they are connected to each other.

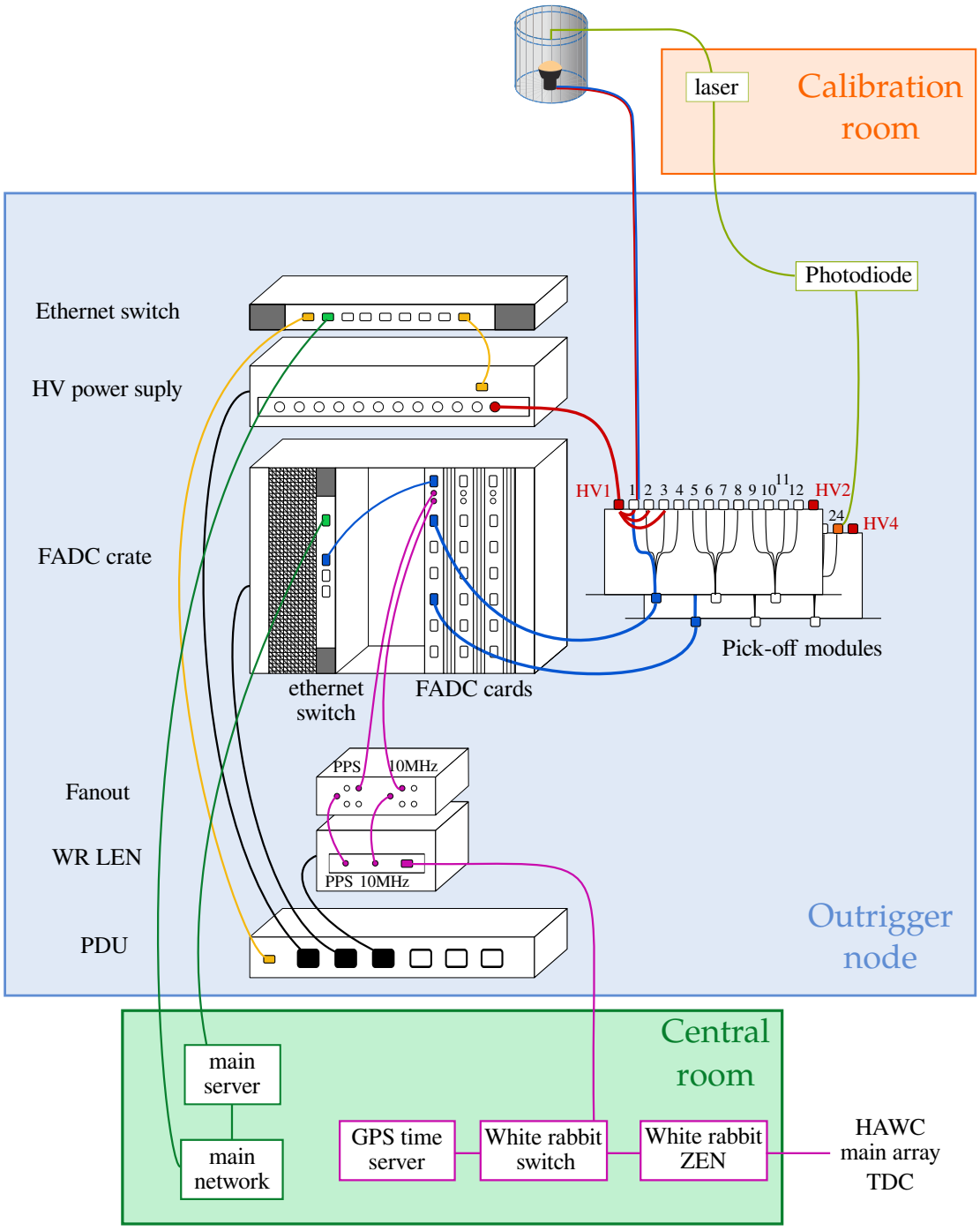

Figure 3.10: Schematic of all the electronic devices and connections inside a Node needed to operate an outrigger section.

The different components per node are described in the following paragraphs.

High Voltage power supply

A multichannel High Voltage (HV) power supply system from CAEN visible in Figure 3.11 is used to deliver HV to the pick-off modules. The HV ranges from 1400 V to 1800 V, and can be controlled remotely. There are 2 HV channels per pick-off module.

Figure 3.11: Picture of the multichannel HV power supply system.

Pick-off module

Each pick-off module distributes the HV to 6 PMTs via RG-59 coaxial cables. These 6 PMTs are supposed to be matched in gain from lab measurements. In a Node, a total of 6 pick-off modules are connected to 69 PMTs. Three channels are kept for the laser signal from the photodiode (described later in the paragraph about the laser system). Analogue signals from the PMTs are transmitted via the same cable as the HV to the pick-off module. It separates the HV from the signal and sends the signal to the FADC card via Ethernet cables. A picture of such a pick-off module is shown in Figure 3.12.

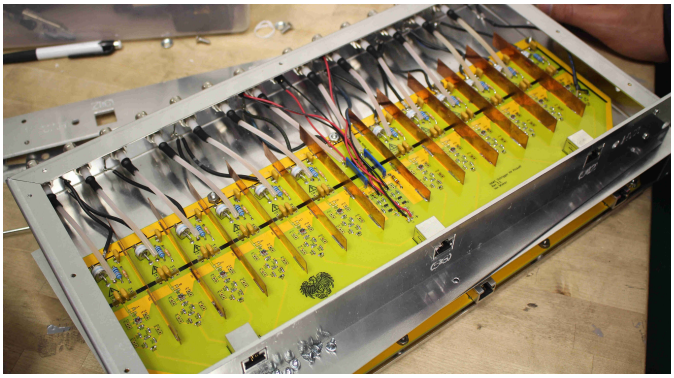

Figure 3.12: Picture of a pick-off module.

The Fast Analogue to Digital Converter (FADC)

The PMT signals are sent via Ethernet cables to the 12 bit FADC cards like the one visible in Figure 3.13, that convert them into a digital signal: they are sampled at 250.10^6samples per second [77]. There are three FADC cards, two pick-off modules connected to each of them, which means 24 channels per FADC card: 23 PMTs and one photodiode. Unlike the main array, the full traces can be acquired and stored for a given number of samples. Examples of such traces are displayed later in this chapter. A readout switch gathers the traces of triggered events from the three FADC cards and sends them via a 10 Gbit fibre to the main server.

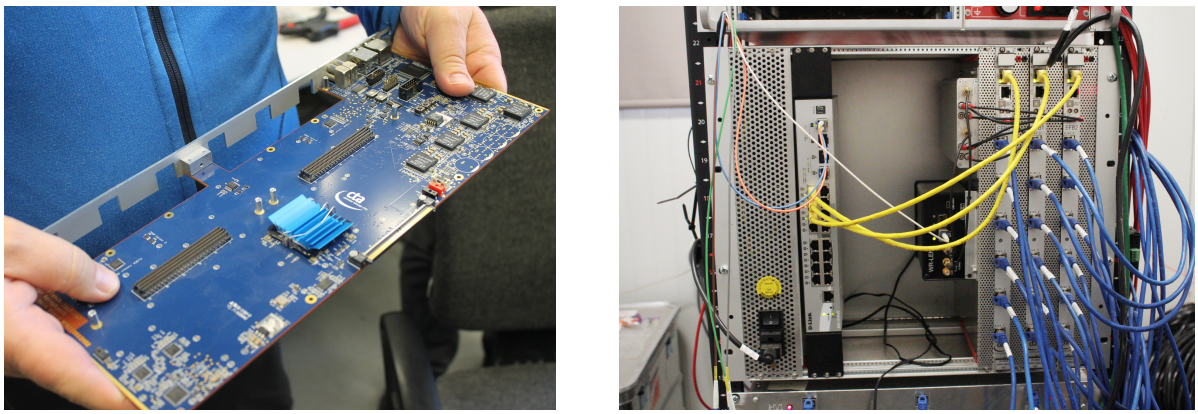

Figure 3.13: Picture of a FADC card (left) and of the whole FADC crate (right): the three cards are on the right hand side, the White Rabbit LEN and the fanout (described in the next paragraph) are visible in the middle, and the Ethernet switch on the left hand side.

White Rabbit LEN

The White Rabbit (WR) LEN generates 1 pulse per second and 10 MHz signals synchronised to the central GPS time server. A custom fanout circuit[6] adapts and distributes these signals to the clock inputs of the FADC modules to assign a time to each event.

Figure 3.14: Picture of the WR LEN and the fanout (credit: Felix Werner).

[6]Internal HAWC documentation available at
https://private.hawc-observatory.org/wiki/images/4/49/FW_20170818_PassiveClockFanoutInstallationAndTesting.pdf

Power Distribution Unit

A Power Distribution Unit (PDU) powers each element. It is remotely controllable. It also powers temperature and humidity sensors that are continuously monitored.

Ethernet switch

There are two Ethernet switches: one permits the remote control of the FADC cards and the WR LEN, and sends via a 10 Gbit fibre the FADC data to the main server. The second one allows remote control of the HV power supply and the PDU.

Laser system

A 532 nm laser located in the calibration room is used for calibration purposes. A system of three filter wheels (FW) is used to manage the laser intensity. The laser and the FWs can be controlled remotely. Each node is also the place where the laser light is spitted and distributed to each outrigger tank via optical fibres. A detailed schematics of the laser calibration system is depicted in Figure 3.15.

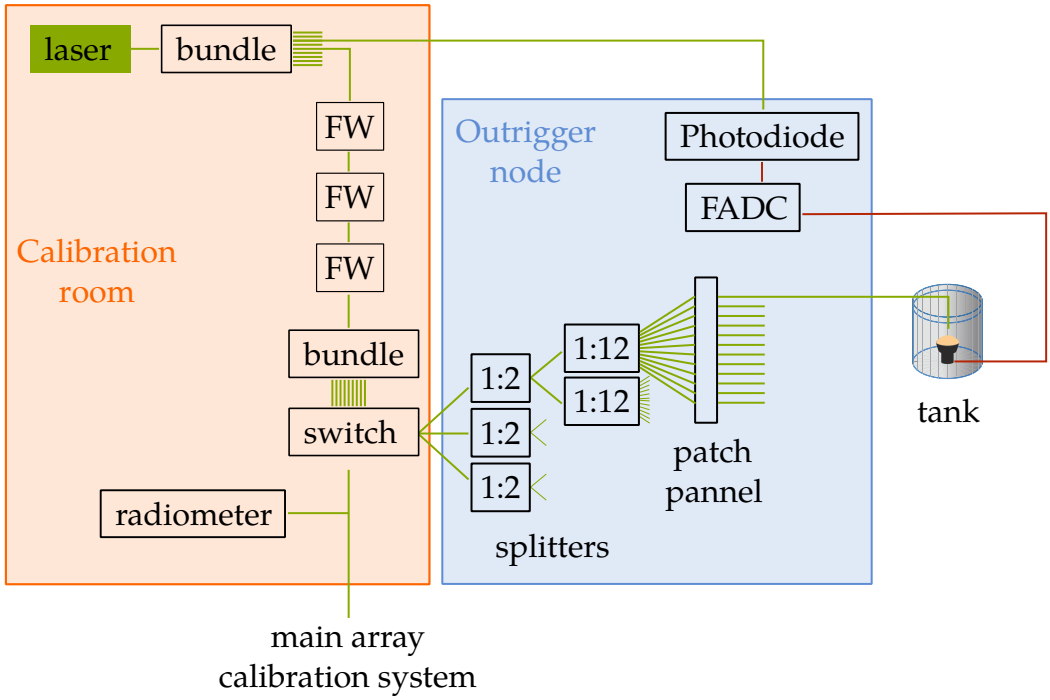

Figure 3.15: Schematic of the laser system from the laser in the calibration room, to the outrigger PMT in the field via the outrigger node. Green lines represent optical fibres and red line other cables. The radiometer measures the laser pulse energy which is used as reference in the calibration process.

3.3 Calibration of the charge pulse reconstruction

Signal extraction of the 345 photomultiplier tubes of the outrigger array needs to be calibrated in terms of pulse charge and timing. This section describes the signal processing and analysis, the calibration procedure is explained in details and its performance is discussed.

3.3.1 Design specifications

At the time of development of the outrigger array, some requirements regarding the performance of the charge and time reconstruction of the outrigger PMT signals were drawn:

- the dynamic range must be at least 0.2 - 2000 PE
- the PMTs should be matched in gain and the gain calibration constants fall in the range 15-25 LSB[7] per PE to allow reasonable measurement of the single PE spectrum and a wide dynamic range.
- the ADC saturation should be not lower than 200 PE
- the time resolution must be of the order of the transit time jitter for signals smaller than ~ 10 PE and smaller than 1 ns for higher signals

3.3.2 Signal properties

The PMT signals in the FADC traces have some specific features that are worth mentioning. They will influence the choice of the strategy to reconstruct the signal charge.

- Each PMT is connected to its corresponding node via a 150 m cable. It results in a pulse which is smaller, wider, and with a longer tail than with a shorter cable as visible in Figure 3.16.

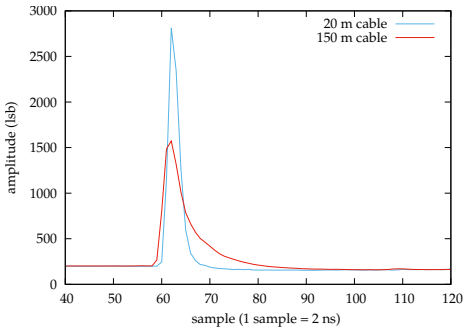

Figure 3.16: Difference in pulse shape with different cable length.

[7]LSB stands for Least Significant Bit

- High pulses show very large **undershoot** as shown in Figure 3.17 where the signal is under the baseline from the end of the pulse to the end of the trace. It is caused by the AC coupling from the transformer and the capacitor inside the pick-off module.

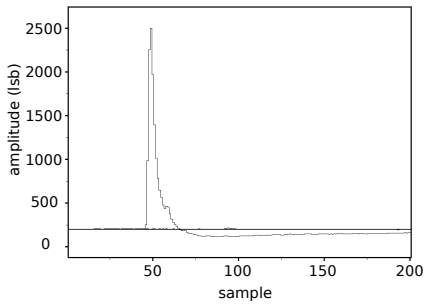

Figure 3.17: Example of a pulse undershoot.

- As mentioned previously, **late pulses** and **after pulses** are common features. Figure 3.18 shows an example of each of them. The late pulses are particularly problematic since they are very close to the main pulse. They are present in ~1% of the signals.

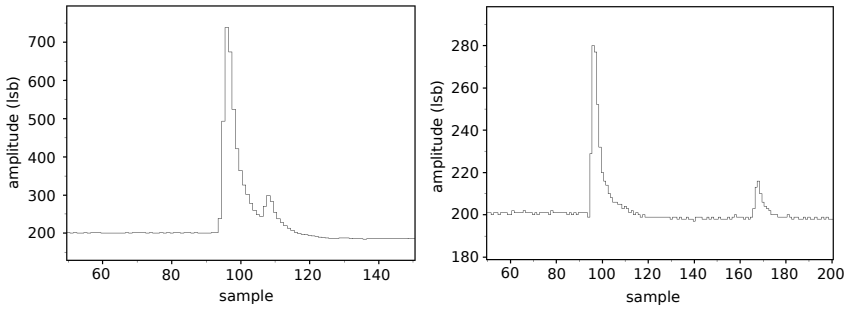

Figure 3.18: Example of a late pulse (left) and an after pulse (right) following the main pulse.

- **Crosstalk** are undesired signals produced by high pulses on a neighbouring channel. They have a bipolar shape that helps to identify them. An example is shown in Figure 3.19.

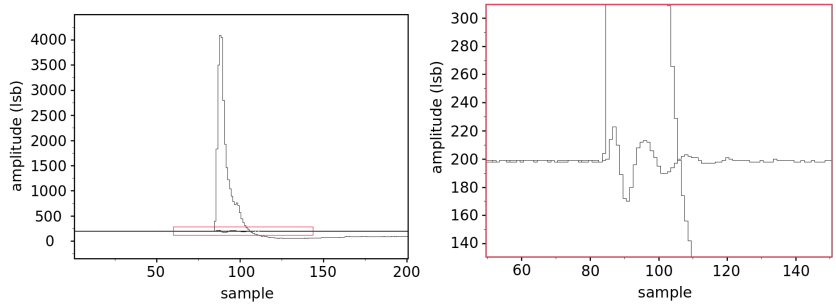

Figure 3.19: Example of a cross talk signal created by a large signal on a neighbouring channel.

3.3.3 Signal processing and shaping

Examples of PMT signals have been shown in Figures 3.17, 3.18 and 3.19. We need to extract from such signals charge and timing in a robust way. To do so, we perform digital signal processing and shaping [85] to make the signal better suited for analysis. The different operations are described in the following paragraphs.

Baseline estimation

The first step is usually to define the electronic baseline to subtract it. It can be either computed internally in the FADC with a specific baseline search algorithm using a few microseconds before the trace that is considered, or estimated by taking the value of the first samples of the trace. Here, the later option is used because of the presence of the undershoot. Figure 3.20 shows a signal (green pulse and green y-axis) for which the baseline has been subtracted (red y-axis).

Upsampling

The data are sampled in the ADC at 4 ns intervals. By upsampling, the number of samples per unit time, the sampling rate, is increased, which means the distance between the points decreases. If the upsampling parameter is set to n, each sample is split into n samples and interpolated. It does not increase the available information. A smoothing of the upsampled trace is also applied. Figure 3.20 shows the advantage of upsampling by comparing the original signal (green) and the upsampled signal (red): the signal looks smoother and the position and the amplitude of the peak can be identified more clearly.

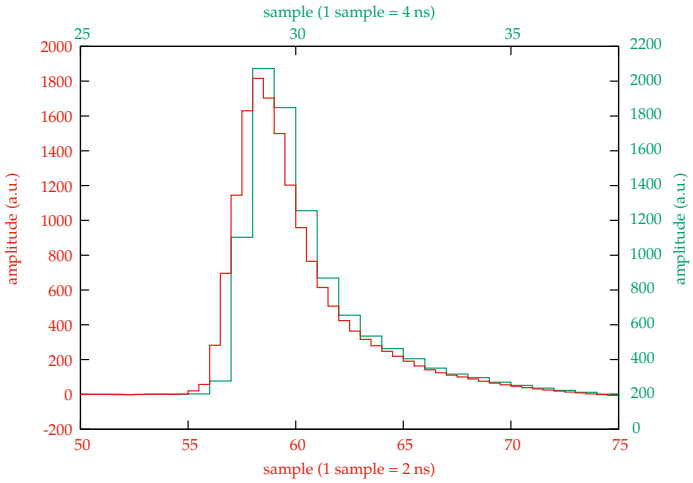

Figure 3.20: Signal upsampling: the green pulse is the input signal with a precision of 4 ns. The baseline is subtracted and the signal is upsampled to 2 ns precision and smoothed to give the red pulse.

Shaping by a moving average

The signal is always shaped by applying a moving average from left to right and from right to left, twice, to the upsampled trace with a given window. The advantages of shaping is that it reduces the influence of the noise, as well as the effect of the transit time jitter. Applying a moving average consists in setting the value of each point to the average of the values of the neighbouring n points, defining the window. It is equivalent to a convolution with a step function n samples wide, as illustrated in Figure 3.21. It behaves like a low pass filter and results in a smoothing of the trace. The shaped pulse is smaller and wider, depending on the value given to the window.

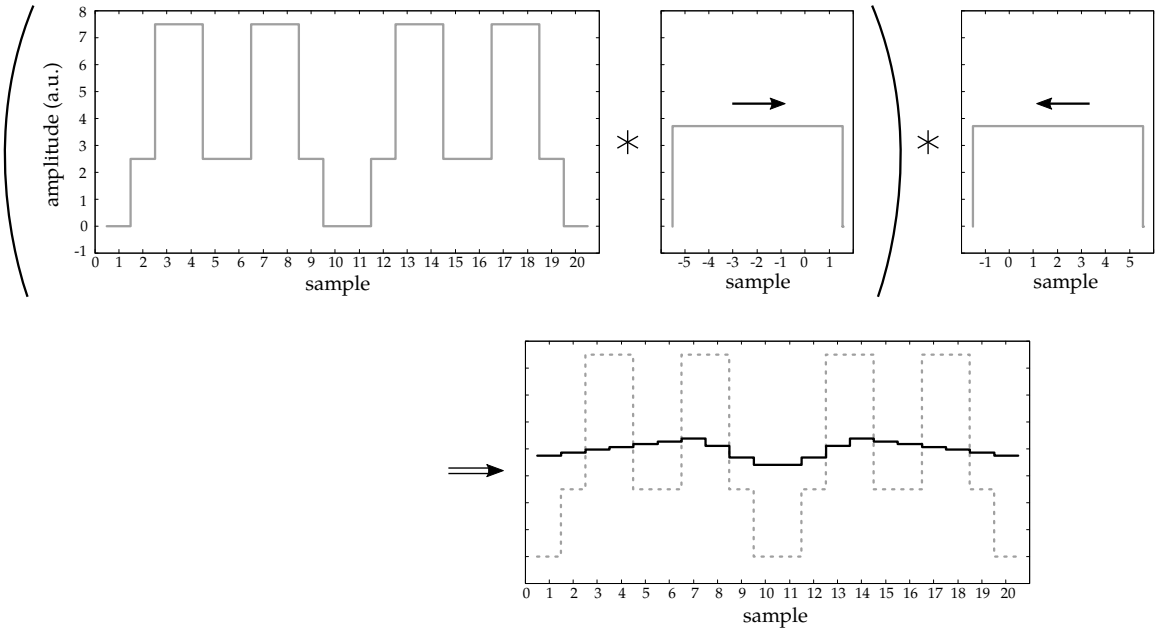

Figure 3.21: Illustration of a moving average. The input signal (top left panel) is convolved with a step function from left to right (top middle panel) and from right to left (top right panel). The resulting trace is on the bottom panel.

Signal differentiation

The fully differentiated signal results in a bipolar signal. It is the slope of the tangent to the signal at each point. Its maximum corresponds to the highest slope of the rising edge of the original signal. The main advantage of using a differentiated signal is that it removes undershoot because of it slow temporal evolution, as well as any baseline fluctuation, that prevents from estimating properly the baseline.

Fast shaping and slow shaping

After substracting the baseline and upsampling the signal, the pulse is either shaped using a moving average with a window *ss* - it is called **slow shaping** - or first differentiated and then shaped with a moving average of window *fs* - it is called **fast shaping**. The size of the window *ss* and *fs* are in number of samples after upsampling. The effect of the size of the window is illustrated in Figure 3.22(a) for the slow shaped trace and Figure 3.22(b) for the fast shaped trace.

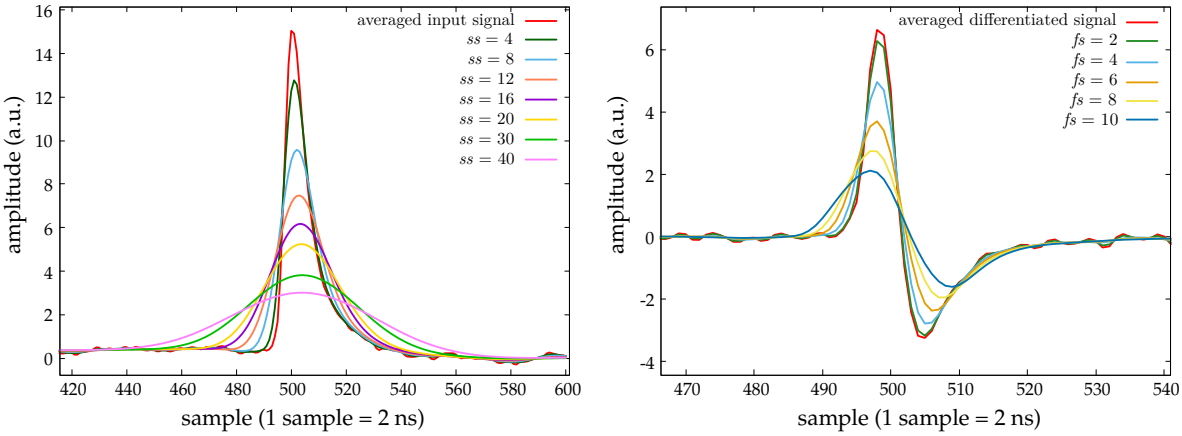

Figure 3.22: Slow shaped signal (a) and fast shaped signal (b) for different windows *ss* and *fs* respectively.

Figure 3.23 shows, for one value of the parameter *fs* and one value of the parameter *ss*, the fast and slow shaped pulses corresponding to a variety of input pulse amplitudes, from single PE pulse to signal saturating in the ADC, called clipped pulse (left plot). The amplitude of the slow shaped pulse (right plot) keeps increasing with increasing input pulse amplitude, even when the later clips. This is not the case for the fast shaped pulse which saturates. Hence, for high intensity pulses and in particular for clipped pulses, the slow shaping is more suited to reconstruct the amplitude of the original pulse. On the other hand, there is a shift of the position of the peak of the slow shaped pulse towards the right as the amplitude of the input pulse increases, which means a shift in time. This is not the case for the fast shaped pulse. Hence, the fast shaping is recommended and will be used for time reconstruction.

The values of the shaping parameters, *fs* and *ss* must be chosen appropriately to optimise the reconstruction of the original pulse amplitude. Figure 3.24 illustrates the influence of the shaping parameters on the amplitude of the shaped signals. One aim of shaping is to allow reconstruction of pulses that clip. The fast shaped pulse (blue curves) is not appropriate to reconstruct clipped signals, since it saturates when the original pulse clips. However, the slow shaped pulse (orange curves) which grows slower than the original pulse, clips later. A value of $ss = 16$ seems appropriate in that case. It is also a suitable value for most of the PMTs. It is the

value currently used in the analysis.

Regarding the value of *fs*, it is chosen to make the pulse wide enough to ensure the stability of the amplitude reconstruction, but not too broad to be able to resolve double pulses. Hence the value of $fs = 8$ is used in the analysis as a good compromise.

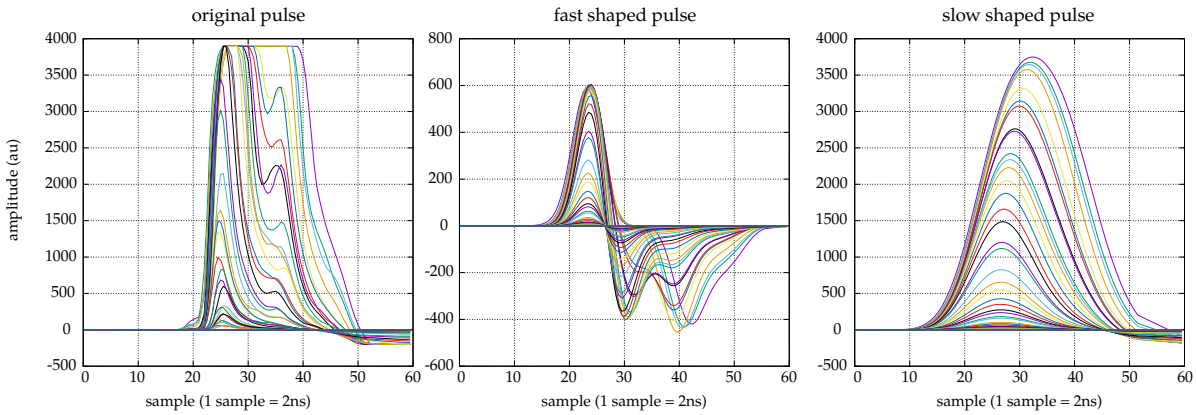

Figure 3.23: Fast shaped pulses and slow shaped pulses are shown on the middle panel and on the right panel respectively, for all the pulses from the left panel.

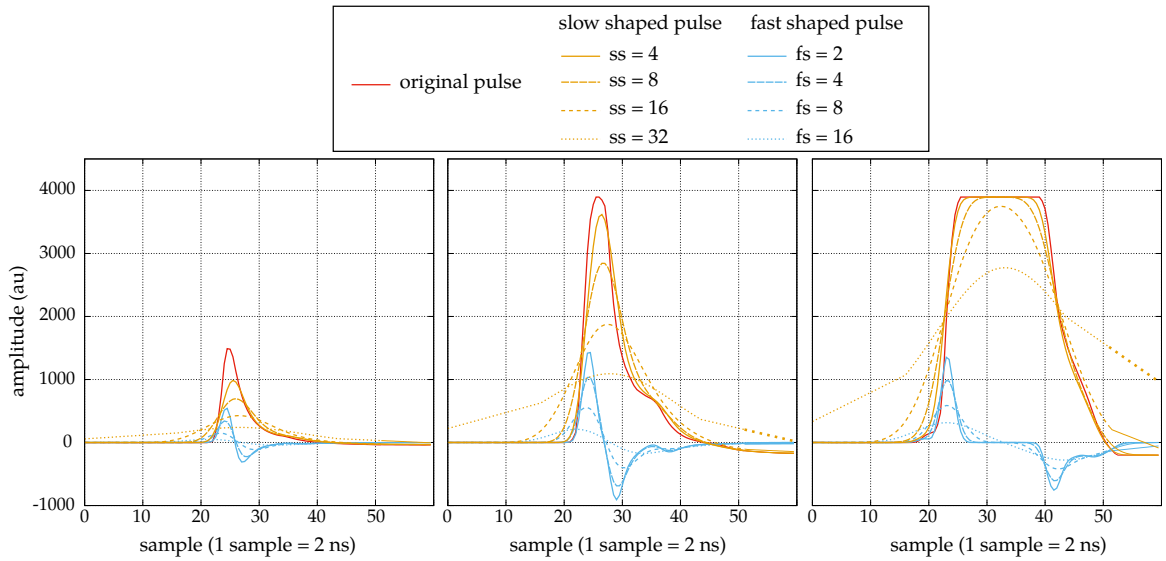

Figure 3.24: Red, blue and orange represent the original pulse, the fast shaped pulse and the slow shaped pulse for different values of the parameters *ss* and *fs*. The three plots illustrate three specific cases when the original pulse does not clip (left), is at the limit of clipping (middle) and is completely clipped (right).

3.3.4 Charge calibration of single photoelectrons

To calibrate the PMT, we need to evaluate the distribution of amplitudes of pulses produced by the PMT in response to a fait pulse, in the single photoelectron regime where photoelectrons can be counted individually. Usually, it is performed by using a laser of very small intensity. However in our case, because of the amount of crosstalk, and the fact that the laser light level is very different between all tanks, it is not an optimal solution. Our decision was to perform calibration during data acquisition using the data themselves. We choose to use air shower events, and identify isolated signals in the part of the trace after the trigger window as illustrated in Figure 3.25. They will be mainly single PE pulses independent from the triggered event, coming from dark noise, but can also be photons entering accidentally the tank, or signal produced by particles from a real shower. Figure 3.25 shows an example of an event with 2 outriggers that triggered in a time window of 50 samples. The trigger point is placed at 50% of the trace, at 100 samples.In the part of the trace between 120 samples and 200 samples, there will be most of the time no more signal, but sometimes, like in that case, there will be a small pulse.

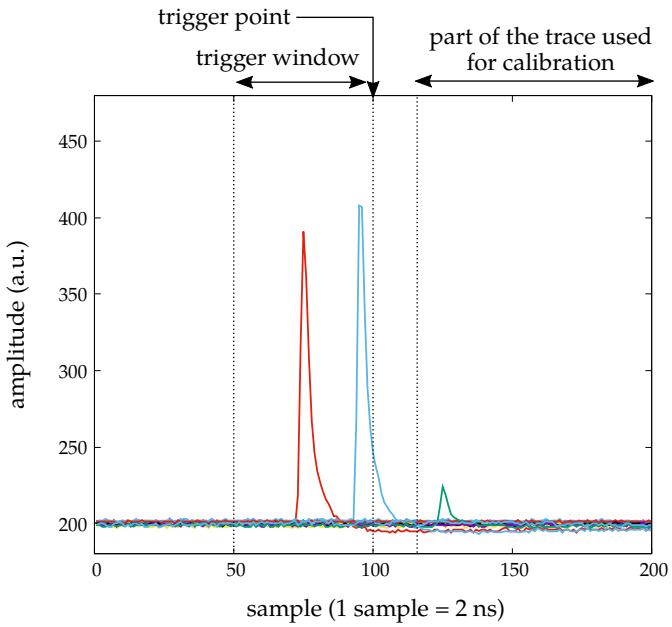

Figure 3.25: Example of a acquired event: 2 outrigger tanks triggered within the time window of 50 samples. The second part of the trace, after the trigger point at 120 samples, is used to look for signals.

These extra pulses are shaped using fast shaping and their amplitude is plotted to produce the distribution, shown in Figure 3.26 (blue curve). The high narrow peak around 0 LSB is called the noise peak. It contains all the empty traces, when the PMT did not detect any extra pulse. After subtracting the noise peak, the remaining distribution is the single PE spectrum. Figure 3.26 also illustrates the method used to subtract the noise peak while taking into account **under-amplified photoelectrons**. They are photoelectrons that did not strike the first dynode,

skip one of the dynode, or produced very few secondary electrons at the first dynodes. This leads to an increase of the noise component of the single PE spectrum. The distribution of the amplitude of the fast shaped signals is smoothed and the noise peak is cut at the height of the single PE peak as shown by the orange curve on the left plot. The remaining distribution is smoothed again to give the orange curve on the right plot. The small bump remaining around 3 LSB accounts for under-amplified photoelectrons. The mean of this distribution, computed from 0 to twice the single PE peak to avoid contamination from higher PE signals, here ~ 70 samples, is the number of LSB per PE, η, called **gain calibration constant**. This value, derived for each PMT, corresponds to the mean answer from the PMT to a 1 PE signal.

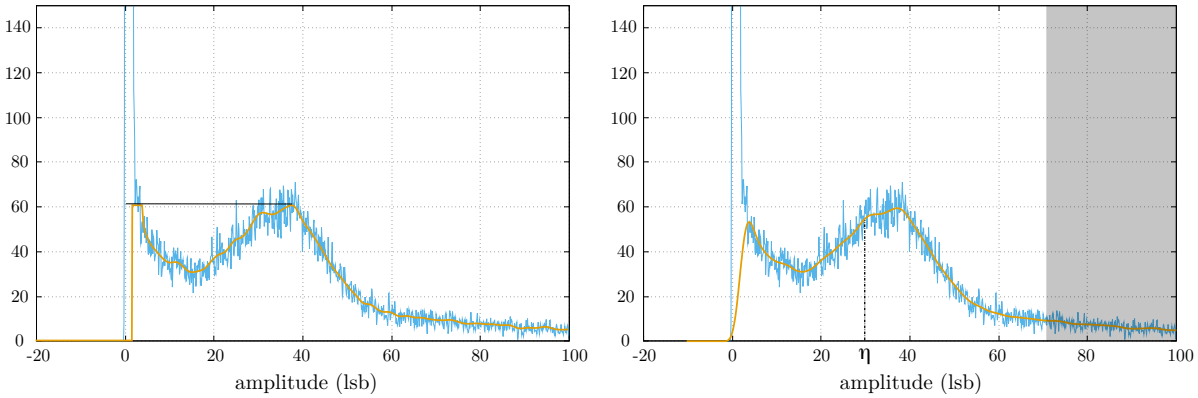

Figure 3.26: Noise peak subtraction. The blue spectrum is the amplitude distribution of the fast shaped pulses (same on both plots). It is smoothed and cut in the noise peak at the height of the single PE bump, as indicated by the horizontal black line. This is the orange curve on the left plot. It is smoothed again on the right plot. The mean of the distribution from 0 to ~70 gives the gain calibration constant $\eta = 32.5$ LSB per pe, as indicated by the vertical dashed line.

3.3.5 Pulse amplitude reconstruction for higher signal

From the calibration step in the single PE regime, an average single PE pulse is derived as a model of the PMT response. This 1 PE model pulse is scaled up over the whole dynamic range up to 200 times the clipping point (in LSB). At each step, the fast shaped and the slow shaped pulses are computed and the ratio between their amplitude and the scaled pulse amplitude is recorded in PE in look-up tables. During data taking, each acquired pulse is shaped as well using a slow shaping and a fast shaping and their amplitude is compared to the values in the look-up table. Depending on the amplitude of the pulse, the correction factor from the table will be applied to the amplitude of one or the other, or a combination of both shaped signal, to reconstruct the charge of the original pulse.

This is shown in Figure 3.27 and further illustrated in Figure 3.30. The bottom plot in

Figure 3.27 shows the correction factor in pe to apply to the fast shaped and slow shaped signal to retrieve the charge amplitude of the original signal, over the whole dynamic range.

- For small pulses with an amplitude A less than 1/4 of the clipping point (Figure 3.30(a)), the pulse is treated similarly to a single PE pulse: the amplitude of the fast shaped signal A_{fs} is used. Since it increases linearly with the amplitude of the original pulse, a constant correction factor n_{fs} is applied to retrieve the charge amplitude of the original pulse Q.
- For big pulses with amplitude A above 1/2 of the clipping point (Figure 3.30(c) and (d)), the slow shaped signal is more suited, especially for pulses that clip, because its amplitude A_{ss} increases slower than the original pulse amplitude and potentially does not clip. A correction factor n_{ss} is applied to retrieve the charge amplitude of the original pulse Q.
- In the transition region for pulses with amplitude between 1/4 and 1/2 of the clipping point (Figure 3.30(b)), a linear combination of both fast and slow shaped signal amplitude is used.

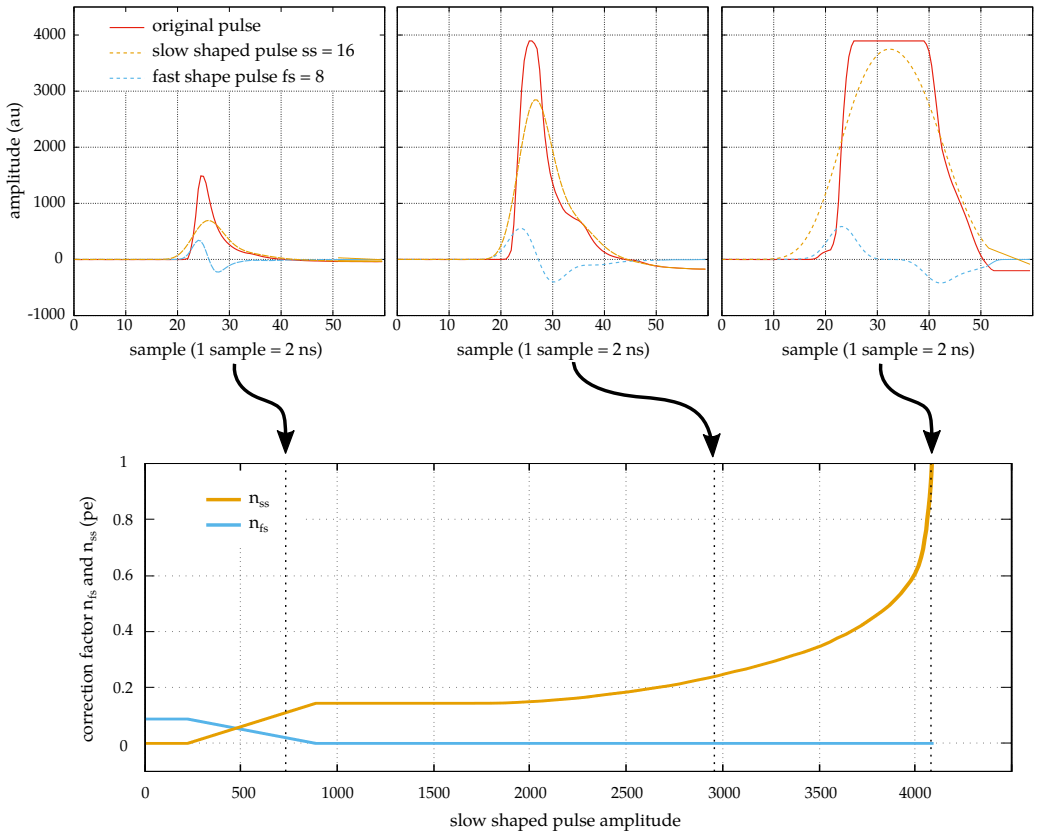

Figure 3.27: Correction factor applied to the slow and fast shaped pulses to retrieve the original pulse charge. The three plots at the top illustrate three specific cases when the original pulse does not clip (left), is at the limit of clipping (middle) and is completely clipped (right). The bottom plot shows the correction to apply to each shaped pulse to retrieve the original pulse charge in PE.

This can be summarised as follow:

$$Q = \begin{cases} n_{fs}A_{fs} & \text{if} \quad A < \frac{\text{clipping}}{4} \\ n_{fs}A_{fs} + n_{ss}A_{ss} & \text{if} \quad \frac{\text{clipping}}{4} < A < \frac{\text{clipping}}{2} \\ n_{ss}A_{ss} & \text{if} \quad A > \frac{\text{clipping}}{2} \end{cases} \tag{3.2}$$

where Q is the reconstructed charge amplitude of the pulse, A, A_{fs} and A_{ss} are the amplitudes of the original, fast shaped and slow shaped pulses respectively, n_{fs} and n_{ss} the correction to apply in PE, depicted by the blue and orange lines in the bottom plot of Figure 3.27.

3.3.6 Reconstruction of laser data

A laser is a very convenient source of monochromatic light to perform calibration. The laser used on the HAWC site has a wavelength of 532 nm. Laser pulses of short duration can be fired on the PMTs with a given frequency using a pulse generator, with an intensity that can be controlled using filter wheels. The laser light is split to be distributed to all the PMTs and to the photodiodes as explained in Section 3.2.2. The laser signals recorded by a photodiode are used as trigger signal. Knowing very precisely when the laser fired, and knowing the length of the cables, we can look for the PMT signal in a defined time window. The left panel of Figure 3.28 shows a PMT response to a laser pulse. However, the pulse produced by the PMT seeing an attenuated laser pulse of a given intensity, can have a very wide range of amplitudes. This is illustrated on the right panel of Figure 3.28 where the amplitude distribution of PMT pulses is plotted for laser pulses of different intensities.

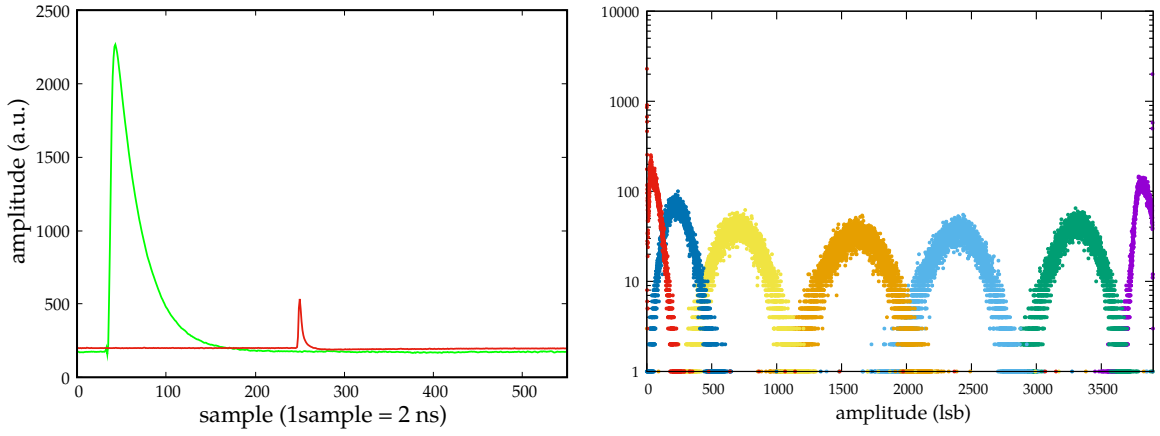

Figure 3.28: The left plot shows the laser pulse (green) recorded by a photodiode and the PMT response (red). The laser pulse is attenuated using filter wheels before arriving at the PMT. Hence the PMT actually sees an attenuated laser pulse compared to the one plotted here. The right plot shows the amplitude distribution of PMT pulses for different laser intensities, represented by the different colors.

Laser data can be taken for all possible filter wheel positions on the whole dynamic range. Typically, a 30 seconds run is recorded for each filter wheel position with the laser firing at 500 Hz, from no laser light (the filter wheels are closed) to the maximum possible laser light (the filter wheels are fully opened). For each filter wheel position, the laser pulse energy is measured using a radiometer to know the laser attenuation.

Knowing the laser frequency, hence the number of laser pulses that were fired, it is possible to work out the fraction of them that resulted in a signal above a certain threshold. For high intensity, the PMT should detect all of them but for very low intensity, in the single PE regime in particular, the PMT may or may not have detected it. It is a measurement of the detection efficiency and it allows to determine the light level in each tank. Since this is a process that follows Poisson statistics, the probability that the PMT does not detect any laser pulse while an average number of pulses μ is expected to be provided by the laser, can be written:

$$\mathscr{P}(0|\mu) = e^{-\mu} \tag{3.3}$$

The probability of detecting a signal is:

$$\mathscr{P}(>0|\mu) = 1 - \mathscr{P}(0|\mu) = 1 - e^{-\mu} \tag{3.4}$$

where the mean number of PE detected by the PMT for a given illumination μ is:

$$\mu = A.10^{-\mathrm{OD}} + \mu_{\mathrm{noise}} \tag{3.5}$$

with A the maximum illumination in PE and OD the optical density. Here μ_{noise} is negligible because of the small time window used and the low rate of dark counts. Hence, the function

$$f(x) = 100 \times (1 - e^{-A.10^{-\mathrm{OD}}}) \tag{3.6}$$

can be fitted to the PMT detection efficiency taken for all laser light levels with a trigger threshold as low as possible before the noise level. The result is shown in Figure 3.29 for one PMT. The blue dots are the fraction of laser pulses detected by the PMT as a function of the laser attenuation and the red line is the result of the fit. The value given by the fit for A gives the maximum amplitude in PE in the y top axis that corresponds to OD = 0. The dark blue vertical line corresponds to a mean amplitude of $\mu = 1$ PE:

$$\mu = A.10^{-OD} = 1 \quad \Rightarrow \quad OD_{1pe} = -\log_{10}\left(\frac{1}{A}\right) \tag{3.7}$$

The laser intensity is now calibrated in PE: we know exactly for each laser intensity, the corresponding PMT signal amplitude in PE. Note that it is different for each PMT because of the variation of the PMT properties from one to the other, the difference in gain and the inhomogeneity in light level in each tank.

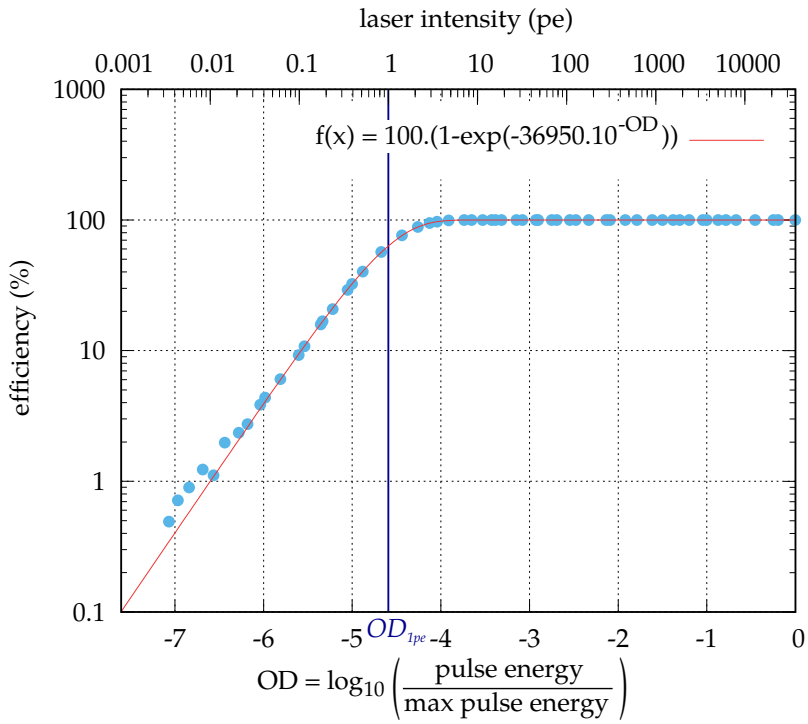

Figure 3.29: Fraction of laser pulses detected by a PMT as a function of the laser intensity. The red curve is a fit to the points and the result of the fit is given in the legend. This PMT detects at maximum 36950 PE from the laser. It detects in average pulses of amplitude 1 PE for an optical density $OD_{1pe} = -4.6$

Summary and reconstruction refinement for clipped signals

Figure 3.30 illustrates the amplitude reconstruction of pulses of different intensities, following equation 3.2. Similarly to Figure 3.27, the blue and orange curves in the side panel of each plot illustrate the correction factor to apply to the fast and the slow shaped signal for the original pulse amplitude reconstruction. The main plot in this figure shows a linear relation between the incoming laser pulse amplitude (red dots) and the reconstructed amplitude, until the pulse is clipped (black dotted line). After this point, the signal may be mis-resonstructed either because parameters for the slow shaping is not optimal, or because of the presence of under-amplified electrons that are not well taken into account. It may also be an effect of the non linearity of the PMT above ~200 PE. This would require further investigation. A this point, an additional correction is applied to the reconstructed amplitude. It simply consists in the difference between the reconstructed amplitude and the linear relation with a linear interpolation, resulting in the green points.

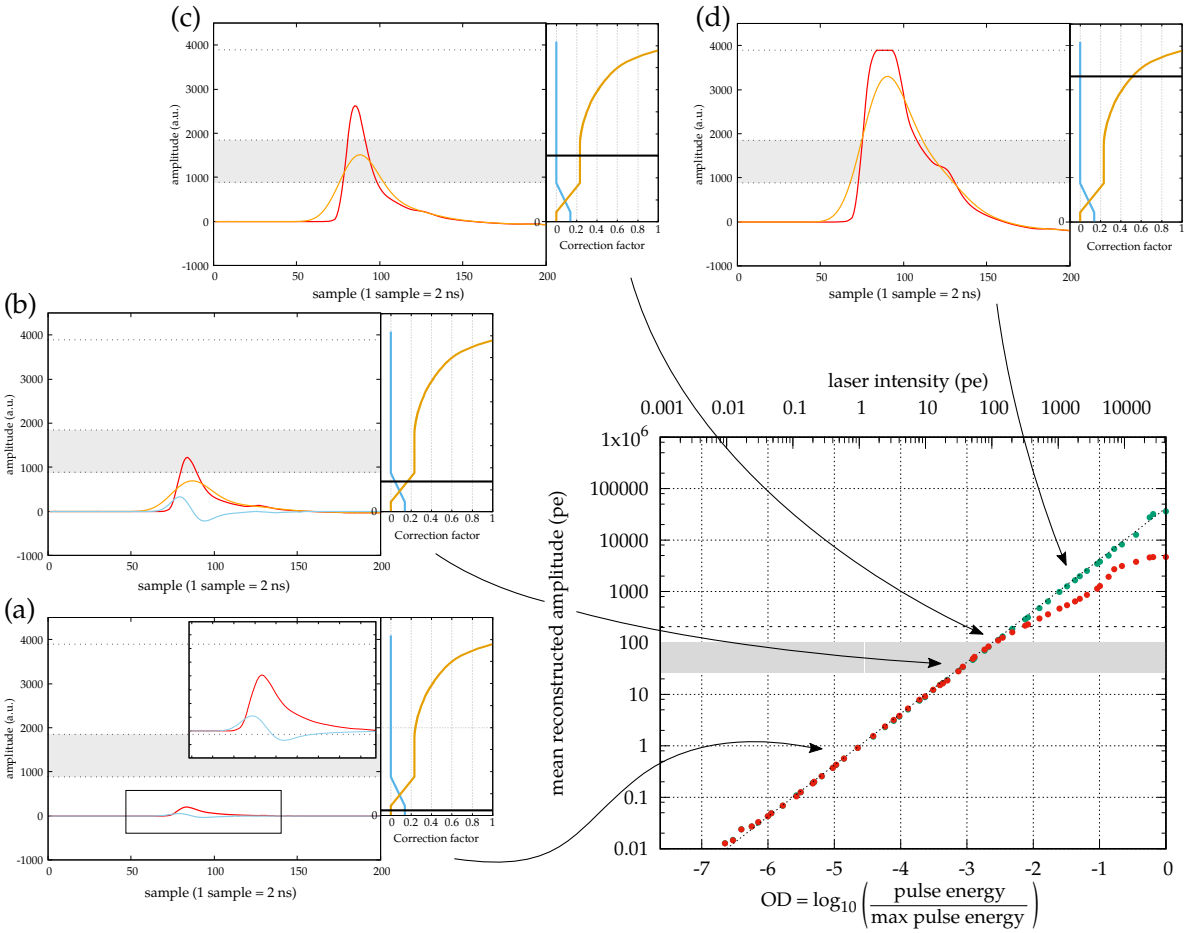

Figure 3.30: The PMT pulse amplitude is reconstructed using the fast shaped pulse (below 1/4 of the clipping point), the slow shaped pulse (above 1/2 of the clipping point) or a linear combination of both (between 1/4 and 1/2 of the clipping point, represented by the grey region). It gives the red points on the main plot. The four panels on the side show examples of pulses in the different regions and the correction factor given by the blue and the orange curves. The horizontal doted line represents the clipping point. A final correction is applied to account for the deviation to the linear relation for clipped pulses, giving the green points.

3.3.7 Time reconstruction

Regarding time reconstruction, the time of the maximum of the fast shaped pulse is always used because, unlike the time of the slow shaped pulse, it is very stable over the whole dynamic range. As described in the first section, it corresponds to the time when the slope of the rising edge of the original pulse is the highest. Figure 3.31 shows a raw pulse (green) that is upsampled (red) differentiated (dark blue) and shaped with a window $fs = 8$. The samples of the differentiated pulse in the box are those used to calculated the highest sample of the fast shaped pulse in the moving average. The maximum of this fast shaped pulse is found, and the center of gravity in a

window of $fs/2 = 4$ around the maximum is computed to give the time of the pulse, here 112 ns. Figure 3.32 shows the time difference between the fast shaped pulse and the laser pulse, as a function of the laser pulse intensity. We can see that it is very stable within a few percents up to ~500 PE, near the clipping point.

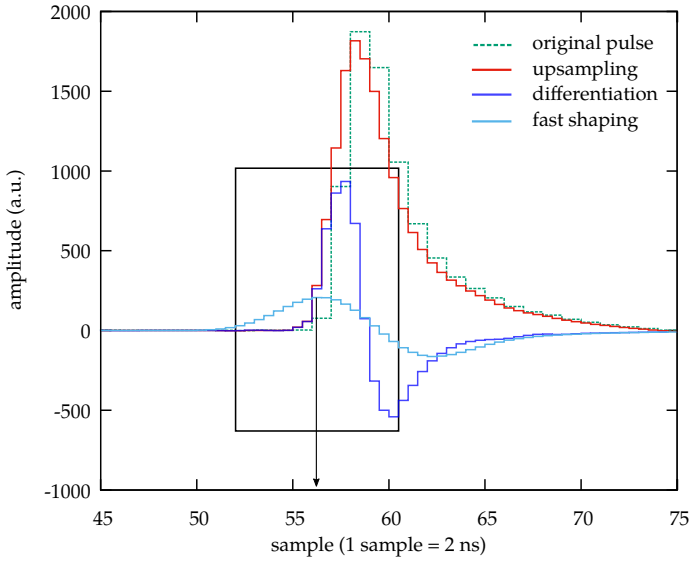

Figure 3.31: The original pulse (green) is upsampled (red) differentiated (dark blue) and shaped with a window $fs = 8$ (light blue). The time of the peak of the fast shaped pulse is used for the time reconstruction. It is calculated with a moving average using the samples of the differentiated pulse in the black box.

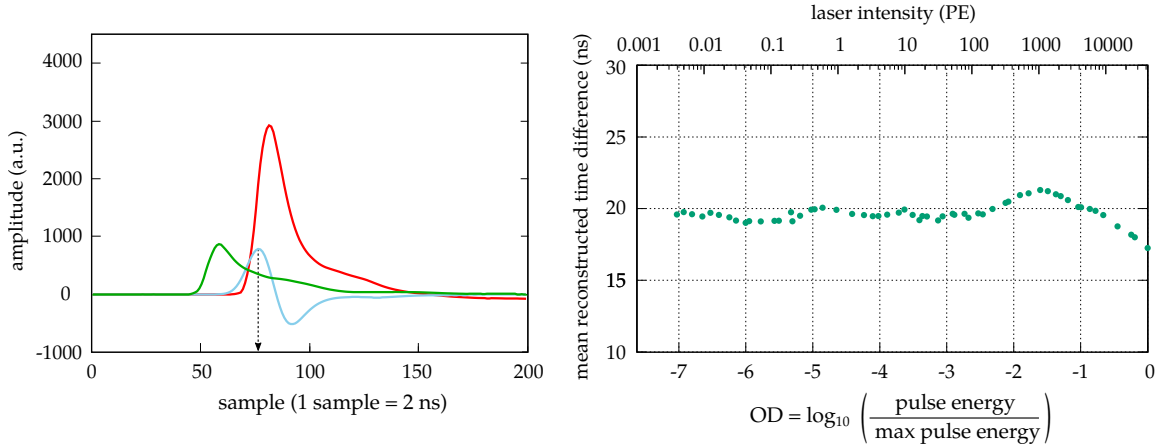

Figure 3.32: The time of the fast shaped pulse is used for time reconstruction as illustrated on the left plot. The right plot shows the time difference between the fast shaped pulse and the laser pulse, as a function of the laser intensity.

3.3.8 Time and amplitude resolution

To assess this method, and check that it fulfils the requirements, the performance of the time and the amplitude reconstruction are estimated using reconstructed laser data. The resolution, given by the standard deviation, is calculated using:

$$\sigma = \sqrt{\frac{\sum_{i=1}^{N}(x_i - \overline{x})^2}{N-1}} \tag{3.8}$$

where x_i are either the reconstructed amplitude (for the amplitude resolution) or the time difference between the PMT pulse and the laser pulse (for the time resolution) for N recorded pulses, and $\overline{x}$ is the mean value in each case. Both time and amplitude resolution curves are plotted in Figure 3.33 as a function of the illumination level.

The amplitude resolution between 1 PE and 500 PE follows the Poisson limit ($\sigma = \sqrt{\text{charge (pe)}}$). The points should be above the Poisson limit and the deviation to this limit should be roughly given by the ENF. For our PMT the ENF is expected to be between 1.2 and 1.4. Some points have value slightly below this limit, which may be an indication that the calibration of the single PE is not completely correct. Above 1000 PE, there is an increasing deviation to the Poisson limit, due to the FADC clipping and the saturation of the PMT. The range below 1 PE is not relevant for the amplitude resolution because the signal are mainly dominate by noise.

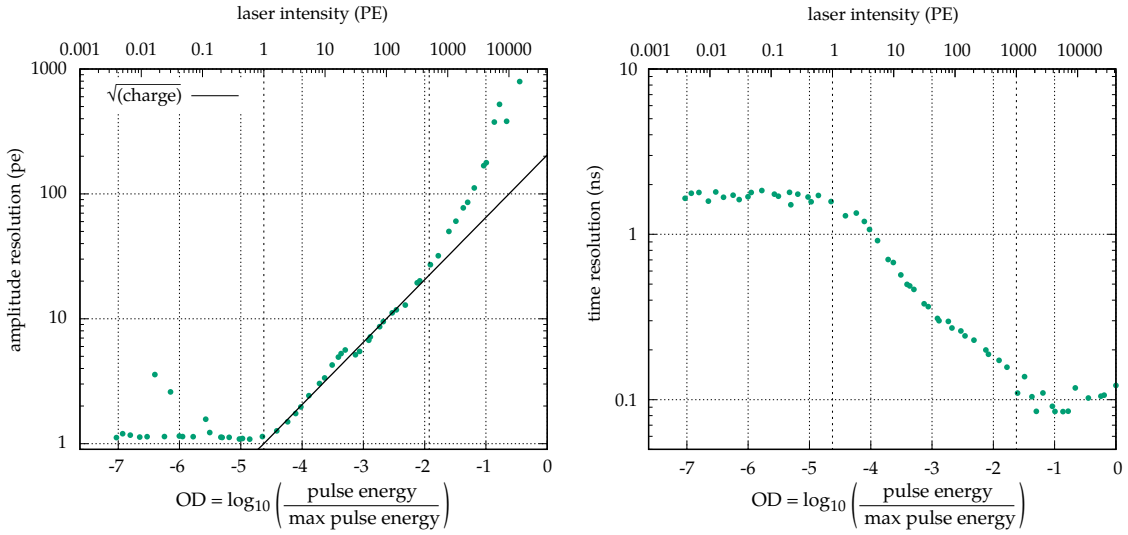

Figure 3.33: The left plot depicts the amplitude resolution for one PMT. The black line is the limit if the amplitude distribution would follow perfectly a Poisson distribution. The right plot is the time resolution for the same PMT.

The time resolution at 1 PE is ~1.2 ns which roughly corresponds to the expected value of the transit time jitter (FWHM = 2.4 $\Rightarrow \sigma$ = 1 ns for this type of PMT, according to Hamamatsu) which was our requirement. The small deviation to this value is caused by the different evaluation of the rise time jitter: it is estimated by Hamamtsu for PE value > 0.25 whereas our measurements are starting at 0 PE. Below 1 PE the time resolution is mainly dominated by our signal search window of ~8 ns which corresponds to σ = 1.8 ns for events with no signals. It drops between 1 PE and 1000 PE to reach a resolution of 0.1 ns, and it stays constant above 1000 PE because of FADC clipping and PMT saturation.

The results are shown for one typical PMT only, but the requirements are fulfiled for almost all of our PMTs. The time resolution above 10 PE which is the most important parameter for our experiment to accurately reconstruct the shower direction, is much better than the requirements.

3.4 On-site measurements and diagnostics

3.4.1 Data acquisition

The data acquisition (DAQ), online data reduction and data formatting is combined in a multi-thread pipeline specifically developed for the HAWC outriggers, called FALCON-DAQ. The pipeline is sketched in Figure 3.34. The main thread reads the configuration files and loads calibration files. These files contain all the parameters needed in the acquisition:

- the number of samples that will be recorded: typically 100 samples, which is 400 ns
- the requirements on the trigger multiplicity: 2 PMTs triggering within a window of 160 ns
- the trigger threshold: 1 PE for each PMT

The main thread further receives commands from a control socket to start and stop DAQ, or configures a calibration run. Examples of events are shown in Figure 3.35 for 23 PMTs of a FADC card over 200 samples. They are passed to the zero suppression module that flags all empty traces. Most of the events trigger 2 PMTs only, as it is the case for the event on the left of the figure. Hence, only theses traces are processed further. The 21 others can eventually be discarded. The remaining traces are passed to the pulse reconstruction module that reconstructs charge amplitude and timing for these pulses. This is also where online calibration takes place, using a determined fraction of events. This step was explained in details in Section 3.3. Finally, the event writer formats the event for storage in a file in XCDF format[8]. Calibration data and random triggered data, used for noise analysis and simulation, are stored in separate files. The event files will be read later for merging, event reconstruction and analysis.

[8]The eXplicitly Compacted Data Format, Copyright (c) 2014, University of Maryland Jim Braun and Segev BenZvi. Available at https://github.com/jimbraun/XCDF.

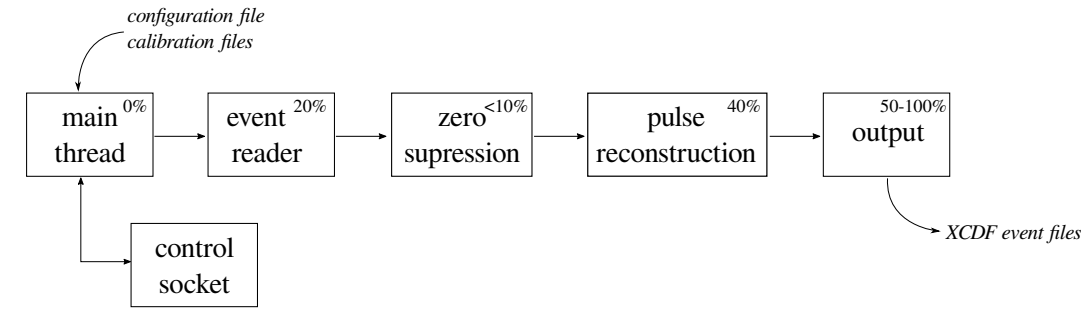

Figure 3.34: Diagram of the data acquisition pipeline. Percentages give the approximate CPU core usage during normal data taking.

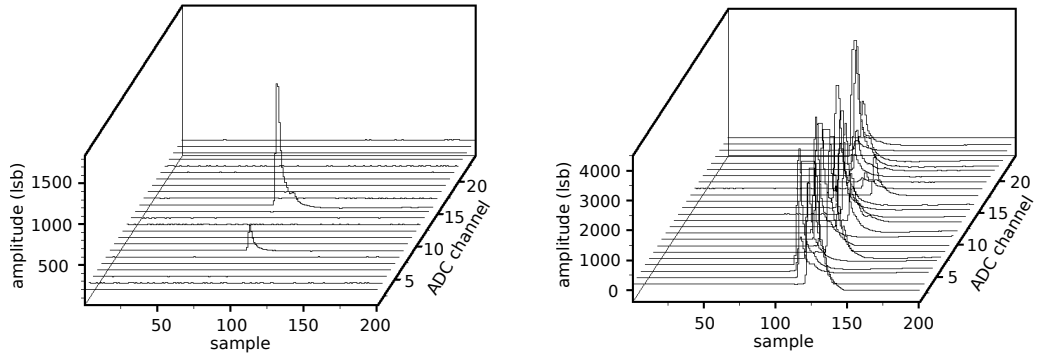

Figure 3.35: Example of events from a FADC card. The traces of the 23 channels are displayed.

3.4.2 Monitoring of the outrigger array

While the outriggers were being deployed, and now that the array is fully operational, it is very useful to monitor remotely some parameters to make sure that the system is working as expected. Some examples are given here.

Stability of the gain calibration constants

An important question is how often do the PMTs need to be calibrated. In other words, how stable is the calibration over time. As soon as the PMTs were deployed, and the calibration procedure operational, calibration runs have been taken regularly to assess its stability. An advantage of being able to perform calibration during normal data taking is that it can be done anytime and as often as needed. The left plot of Figure 3.36 shows the monitoring of the gain calibration constant η over the 7 first months of operation of node A, for the 23 PMTs of the first FADC card. The calibration constants are stable for all of them within a few percents during this period of time. A small jump is visible for a few PMTs in November 2018 that may be due to a change in HV. The white vertical spaces are periods where it has not been possible to take data

for example for maintenance reasons. The right plot of Figure 3.36 shows the distribution of the gain calibration constants for all 345 PMTs of the outrigger array. There are 7 PMTs with a null calibration constant, likely not installed or defect PMTs. The mean value is around 15 LSB per PE. The array is gain matched within $\sigma = 20\%$.

As explained in Section 3.2.2, PMTs have been gathered in groups of 6 per HV channel, depending on their nominal HV. It is also possible to check for each HV channel individually the distribution of gain calibration constants of the 6 PMT connected. An example is plotted in Figure 3.37 for the 12 HV channels of node A. It can be immediately seen which PMT is not matched in gain with the others of the same HV channel. For example, on HV channel 4 one PMT has a very high gain constant of ~32 LSB per PE when the others have a gain constant between 15 and 19. Otherwise for this node, most of the channel are matched within $\sigma = 20\%$ as already concluded from the previous figure.

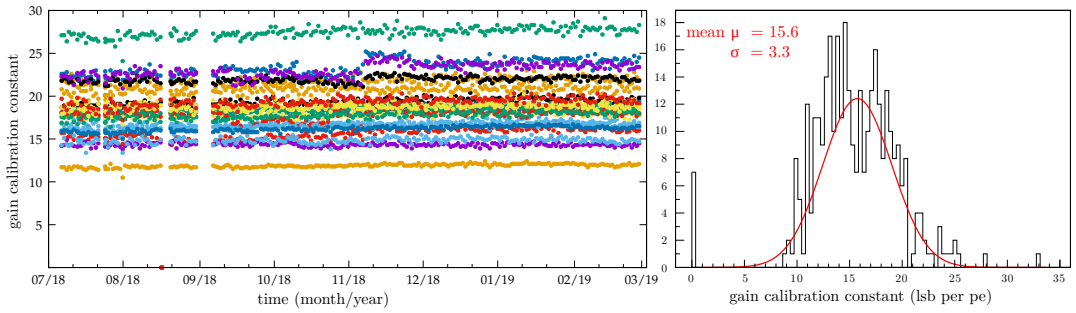

Figure 3.36: The left plot shows the stability of the gain calibration constants of the 23 PMTs connected to the first FADC card of node A over the first 7 months of operation. The right plot shows the distribution of the gain calibration constant for all 345 PMTs of the outrigger array.

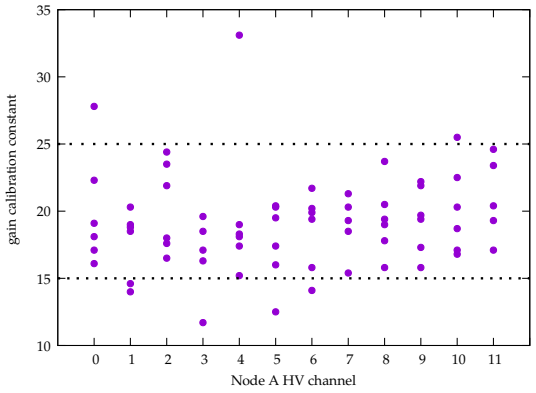

Figure 3.37: Distribution of the values of the gain calibration constants per HV channel. On this plot are represented the 12 HV channels of Node A, with 6 PMTs being connected to each channel. The dotted line represent our requirement range.

Trigger rate

The trigger rate of the PMTs individually and of the array in general is very important to monitor. A stable trigger rate is a sign of the good health of the instrument. Moreover, monitoring the triger rate can help to quickly identify a bad PMT, or a light leak in a tank. Figure 3.38 is an illustration of the trigger rate of the 23 PMTs of the first FADC card of node A over 3 days. Each point type and color represent a different PMT. Some periodic variability is visible for the PMTs with the highest rate. The continuous black line is the trigger rate of the whole FADC card under the trigger condition defined for data acquisition: 2 outrigger tanks triggering above a threshold of 1 PE within a time window of 160 ns. It is quite stable around 4500 events per second. On a longer time period, Figure 3.38 shows the rate of 2 PMTs of the first FADC card of node A over 5 months. Each point corresponds to one measurement taken roughly every 6 hours. The continuous lines are the mean trigger value averaged over periods of one week. For these 2 PMTs, it looks very stable. The continuous black line is again the data acquisition rate.

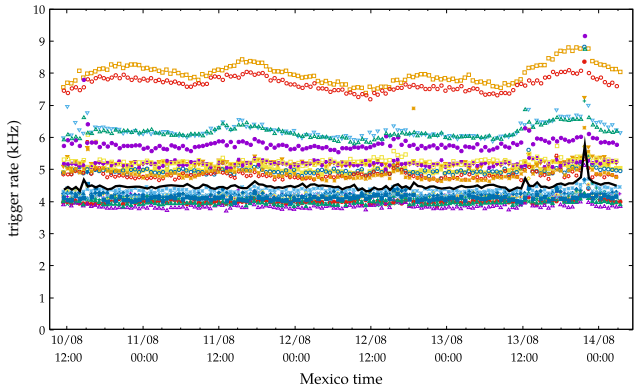

(a)

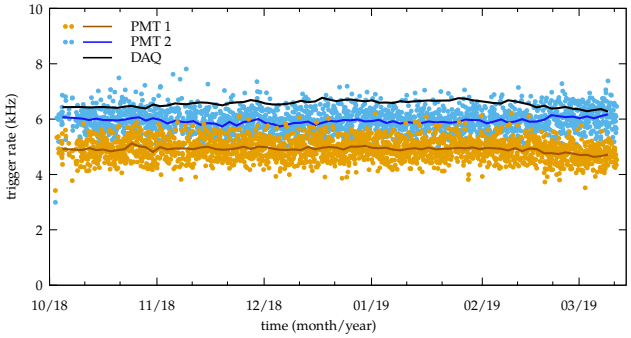

(b)

Figure 3.38: Monitoring of the trigger rate of individual PMTs over different time scales: the top plot shows the rate of all the 23 PMTs of the first FADC card of node A over 3 days. The measurements are separated by 30 minutes. The bottom plot shows the rate of two of these PMTs over 5 months. The measurement are separated by 6 hours and the continuous lines are the mean trigger value averaged over periods of one week. In both plots, the black lines are the acquisition rate for this FADC card.

Multiplicity trigger

Another interesting parameter to look at is the event multiplicity: the number of PMTs participating in the triggered events. The plot in Figure 3.39 shows that no events were recorded with 0 or only 1 PMT triggering. That is expected since the requirement for data acquisition is that a minimum of 2 PMTs trigger within 160 ns. 80% of the recorded events have signal in 2 PMTs only, 10% have signal in 3 PMTs. Less that 1% have a signal in more than 8 PMTs.

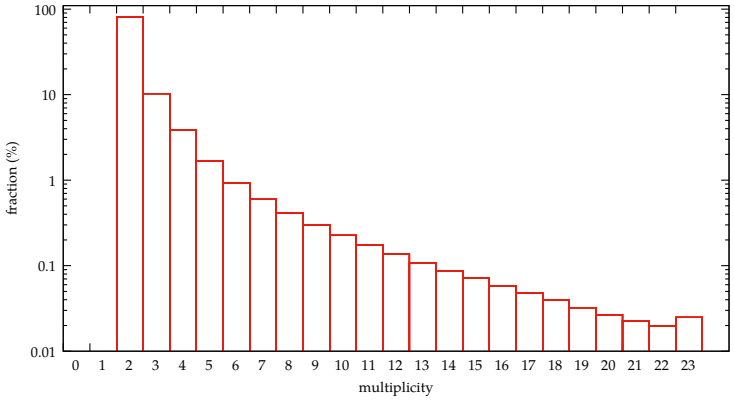

Figure 3.39: Multiplicity trigger of acquired events for the first FADC card of Node A, averaged over 6 months.

Participation fraction

The participation fraction, representing the fraction of acquired events for which a PMT triggered, is also important to diagnostic any outlier: a PMT that does not participate enough may have connection issues, or a PMT that participates more than the others can be noisy or in a tank that is not light tight for example. The plot in Figure 3.40 shows that all PMTs seem to participate equally within $\sigma = 10\%$.

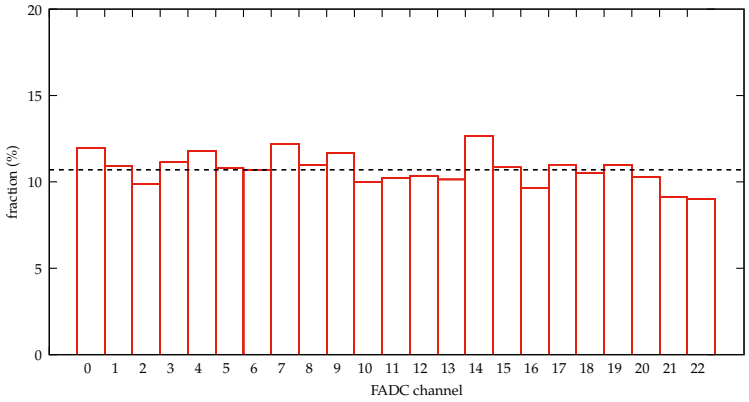

Figure 3.40: Participation fraction of all the 23 PMTs of the first FADC card of Node A averaged over 6 months. The dotted line is the average participation fraction of all the PMTs.

Time between events

The time between consecutive events is expected to be exponentially distributed because the arrival time of events is random and the events are independent. This can be seen on the plot in Figure 3.41 which shows the distribution of the time between two consecutive events, averaged over 2 hours. The right plot is the whole distribution over 3 ms. The black line is the exponential function $f(x) = a \cdot \exp(-x/b)$ fitted to the data between 0.1 and 1.5 ms, with $a = 154$ and $b = 0.27$ ms. The inverse of b, equal to 3.6 kHz corresponds to the aquisition rate. Note that the value is lower than the acquisition rate in Figure 3.38 (black line) because the later is affected by crosstalks. The left plot is a zoom on the first 20 μs. There are three features that deviate from the exponential fit. The first high peak in the first bin of the histogram is likely due to retriggerd events: two events triggering within the same trace. The large bump between 5 and 8 μs are probably due to after-pulses. According to the Hamamatsu technical sheet for this PMT, they are expected between 100 ns and 16 μs after the main pulse. The narrow peak around 2 μs could be due to signal reflection within the cables, or to after-pulses created by lighter ions.

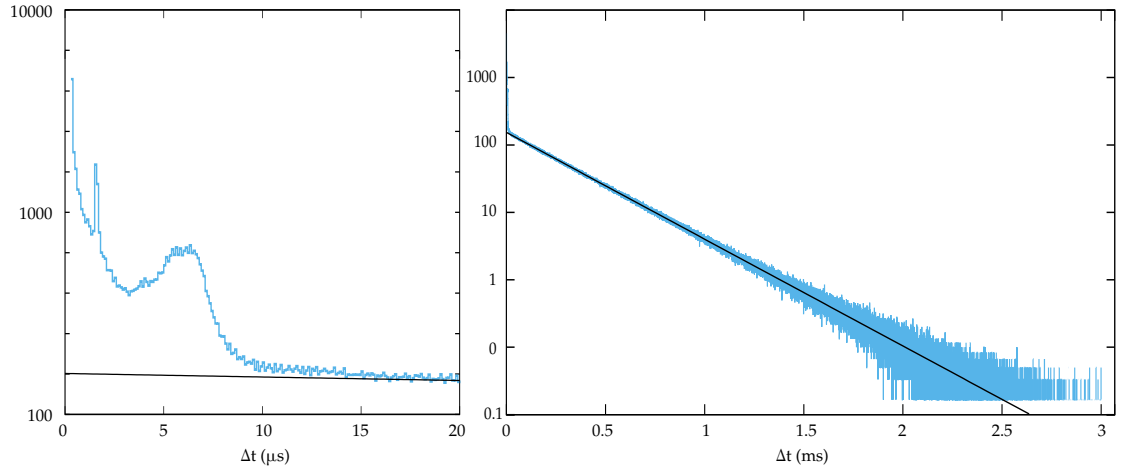

Figure 3.41: Time distribution between events. The left plot is a zoom of the right pot between 0 and 20 μs. The black line is an exponential function fitted to the data.

3.5 Event merging with the main array

Events that trigger the main array or the outrigger array, according to their respective trigger conditions are recorded independently. Merging both data sets is performed afterward: if an outrigger event is found between 500 ns before a main array event and up to 1000 ns after, they are supposed to belong to the same air shower event and are merged. Figure 3.42 displays an example of an air shower event that fulfiled these conditions. A few pulses from outrigger PMTs are also shown. The color scale represents the arrival time and the size of the disks represents the amount of charge deposited in those PMTs. The small red disks in the middle of big yellow

disks are likely after pulses. This figure also illustrates why the outrigger array is useful: for this particular very high energy event, the main array is saturated and the core of the shower was reconstructed using the main array only, on the edge of the array. The signal deposited in the outrigger tanks will help for the core, the direction and the energy reconstruction of the shower.

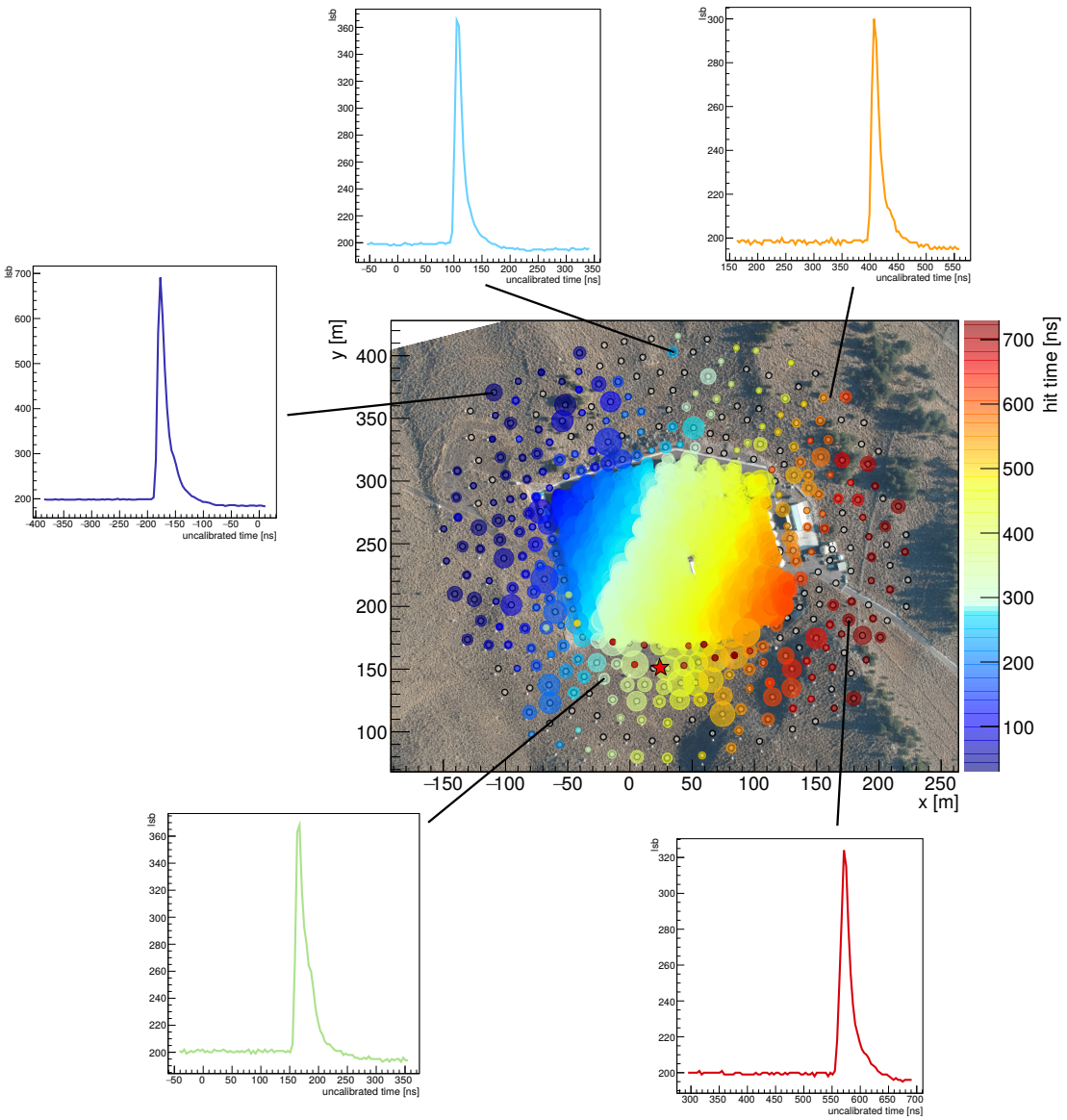

Figure 3.42: Example of an air shower that triggered both the main array and the outrigger array. The colors code the arrival time of the particles in the water tanks. The size of the disks represent the corresponding amount of charge in the PMTs. The red star represents the reconstructed core location using the main array only. Some PMT pulses from outrigger tanks are also displayed (credit: Harm Schoorlemmer, MPIK Heidelberg).

3.6 Conclusion

The outrigger array was the focus of this chapter. I presented its layout, its design and all related pieces of electronics, with a focus on the PMT used in each outrigger tank. I contributed to the calibration of the charge pulse reconstruction, in extensively testing the calibration procedure and assessing its performance. The calibration consists of several steps: first, the derivation of the single PE spectrum and the gain calibration constants for each PMT. It can be performed during data acquisition which has the advantage that it can be done regularly and monitored easily. Secondly, an average single PE pulse is used to derive a look up table to reconstruct signals of higher amplitude. Finally, the reconstruction of laser data are used to apply finer correction at the highest amplitude, for clipped signals.

The whole array can be remotely operated, which allows important parameters such as the trigger rate of each PMT, the acquisition rate of each FADC card, the multiplicity trigger or the gain calibration constants to be monitored. All are very stable since the deployment.

The outrigger array is fully deployed since September 2018. It is now continuously taking data that can be merged with the main array data. A core reconstruction method has been developed and can be used on these data [58]. A next step is the development of a direction reconstruction algorithm to really take all the benefit of this array and improve the reconstruction of γ-ray events above 10 TeV and hence the observatory sensitivity.

CHAPTER 4

THE GALACTIC PLANE WITH HAWC AND H.E.S.S.

The H.E.S.S. collaboration recently published its Galactic Plane Survey (HGPS) [47], which is the deepest survey of the Milky Way in TeV γ rays, using almost 10 years of observations. It contains 78 sources, including 16 new sources previously unknown. On the other hand, the HAWC collaboration also published its first catalogue based on 507 days of data [7]. It is the result of the first source search performed with the complete HAWC detector. In this search, 39 sources have been reported, amongst them 16 detected for the first time at TeV energies. In both cases, supernova remnants and pulsar wind nebulae seem to be the dominant population of sources at this energy. The HAWC data set doubled since then, revealing 10 more sources. Both instruments are very different in terms of conception and regarding the techniques used at every step, from the event observation to the reconstruction, using different γ/hadron separation and background estimation. However, they operate at a similar energy range, complementing each other. In this chapter, I will show an analysis of H.E.S.S. galactic plane data in the spirit of making H.E.S.S. and HAWC maps as comparable as possible. I will show the first comparison of the galactic plane from both instruments, highlight similarities and differences and try to solve some of the apparent inconsistencies that arise from intrinsic properties of the instruments and from their dedicated data analysis.

4.1 The H.E.S.S. Galactic Plane Survey

H.E.S.S. surveyed the galactic plane from 2004 to 2013, producing the H.E.S.S. Galactic Plane Survey (HGPS) [47] with 2700 hours of good quality-selected data. This observation program was carried out by the first four small telescopes, known as H.E.S.S. phase I. Regarding the data quality selection, criteria such as the transparency of the atmosphere, the zenith angle and the minimum number of telescopes participating were applied: observations where the

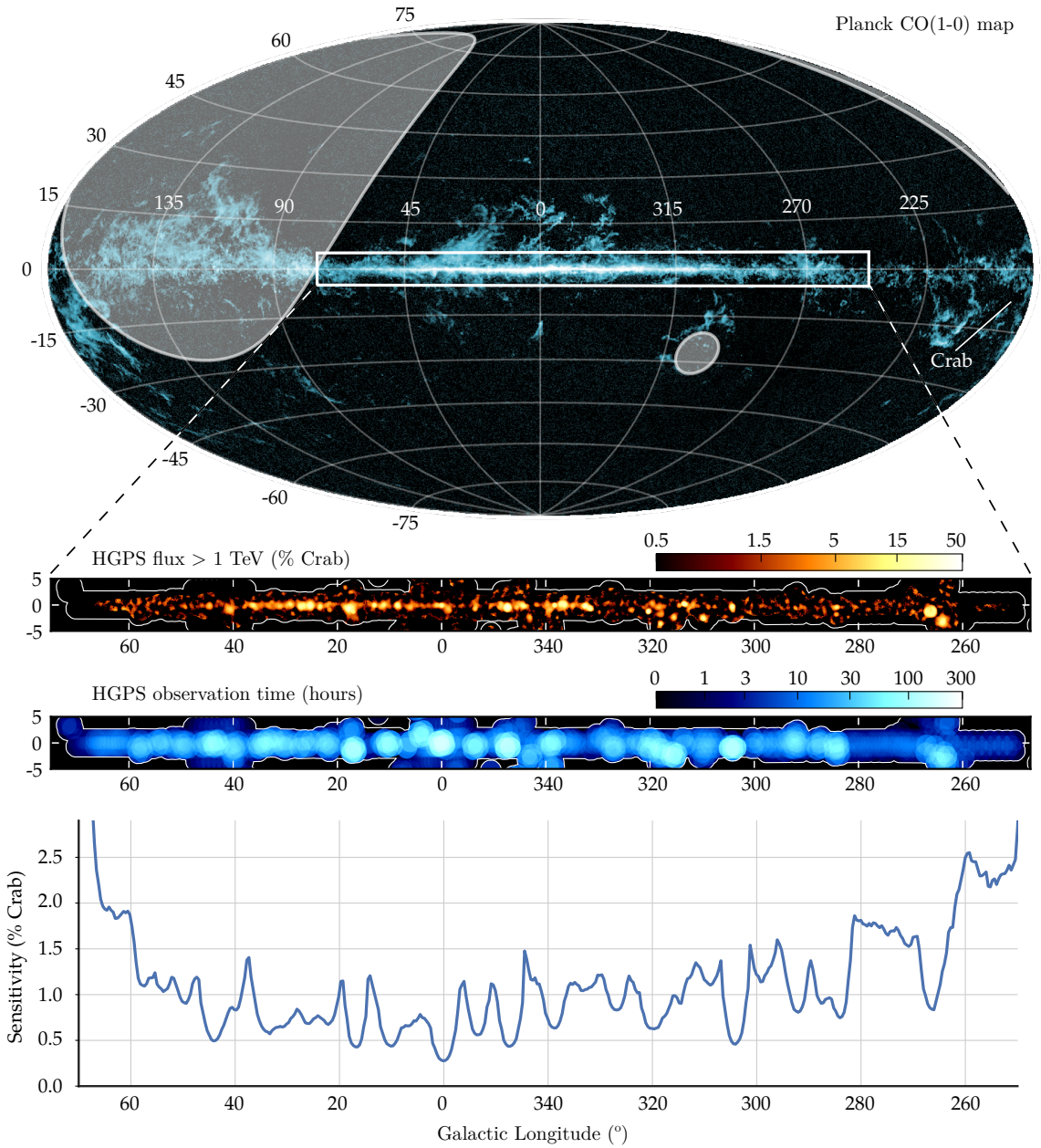

Figure 4.1: H.E.S.S. Galactic Plane Survey (HGPS). The top map is an all-sky image of the Planck CO(1-0) data [75] in galactic coordinates and Hammer-Aitoff projection. The white rectangle represents the region of the sky surveyed by H.E.S.S for the HGPS. The grey shaded regions denote the part of the sky that are not visible by H.E.S.S.. The middle panels show the HGPS γ-ray flux above 1 TeV for regions where the sensitivity is better than 10% Crab with a correlation radius of 0.4°. Below is and the observation time. The bottom plot is the HGPS point-source sensitivity profile along the galactic plane at a galactic latitude $b = 0°$ in % Crab, for a correlation radius of 0.1°, assuming a spectral index of -2.3 under the isolated point source assumption. Here the crab integrated flux above 1 TeV is $2.26.10^{-11}$ cm^{-2} s^{-1} as reported by H.E.S.S. [17]. Adapted from the HGPS paper [47].

Cherenkov transparency coefficient $0.8 < T < 1.2$, characterising the atmospheric conditions for clear skies were used [48]. Moreover, only runs with a zenith angle lower than 65° were considered. Telescopes with significant pixel problems in the camera were also suppressed. At the end, runs with less than 3 telescopes passing the quality cuts have been discarded; 77% of the data that passed the quality cuts actually uses the 4 telescopes. The HGPS covers the region of the sky of longitude $70° < \ell < 250°$ and latitude $-5° < b < +5°$ around the galactic plane, as illustrated by the white box on the Planck all-sky map in Figure 4.1. In the middle panel of this figure, the HGPS γ-ray flux above 1 TeV is depicted, together with the exposure time that varies from a few hours to a few hundreds of hours. The bottom plot shows the HGPS sensitivity as a function of longitude for $b = 0$.

The HGPS map has a pixel size of 0.02°. H.E.S.S. has an angular resolution of ~0.08° and a field of view of 5°, rather large compared to other IACTs like MAGIC and VERITAS that have a field of view of 3.5°. It covers an energy range from 0.3 to 100 TeV, and has an energy resolution of 16% above 440 GeV for a Crab-like source [17]. The achieved sensitivity is less than 2% of the Crab flux, assuming a point source with spectral index of -2.3. It goes down to 0.5% in some specific regions with high observation time, like the galactic center, as shown by the bottom plot in Figure 4.1. Together with the HGPS flux and sensitivity maps, a catalogue has been released with the spatial, morphological and spectral characteristics of all sources. It reports the detection of 78 γ-ray sources. Amongst them 8 Supernova Remnants (SNR), 12 Pulsar Wind Nebulae (PWN), 8 composite objects and 3 binary systems. These types of objects are indeed believed to be amongst the main acceleration sites of charged particles that produce the cosmic ray background detected on Earth. However, 47 sources are not yet firmly identified.

The map making procedure has been described in section 2.1.3. The maps used to perform the analysis presented in this chapter have been made using the Image Pixel-wise fit for Atmospheric Cherenkov Telescopes (ImPACT) [72] event reconstruction algorithm. It uses a maximum likelihood fit to get the best-fit shower parameters, instead of using the traditional parametrisation of the camera images [33], used in the published HGPS [47]. It allows for an improvement in sensitivity of more than a factor 2 for point-like sources.

4.2 The galactic plane with HAWC

The latest HAWC map at the time of writing this thesis uses 1128 days of data taken between the 26th November 2014 and the 24th April 2018. Part of the data was taken with a partial array only, before its completion in March 2015. Since HAWC is a survey instrument, it continuously monitors the sky above it. The part of the galactic plane visible in the Northern hemisphere is present in the HAWC skymap. An all-sky significance map is displayed in Figure 4.2, with a zoom on the galactic plane for longitude $0° < \ell < 90°$ and latitude $-5° < b < +5°$. The same figure shows a plot of the sensitivity of HAWC in this region made in the same condition as the HAWC

catalogue [7]. It is much smoother that the H.E.S.S. sensitivity curve from Figure 4.1 since the observation time varies uniformly with declination. The results I will present make use of events falling in the nHit bins from 4 to 9. These are events that triggered more than 24% of the main array. The main motivation is to have a good enough reconstruction. The angular resolution of the instrument at these energies ranges between 0.4° for bin 4 up to less than 0.2° for bin 9. The data analysis, event reconstruction and map making procedure were explained in section 2.2.3.

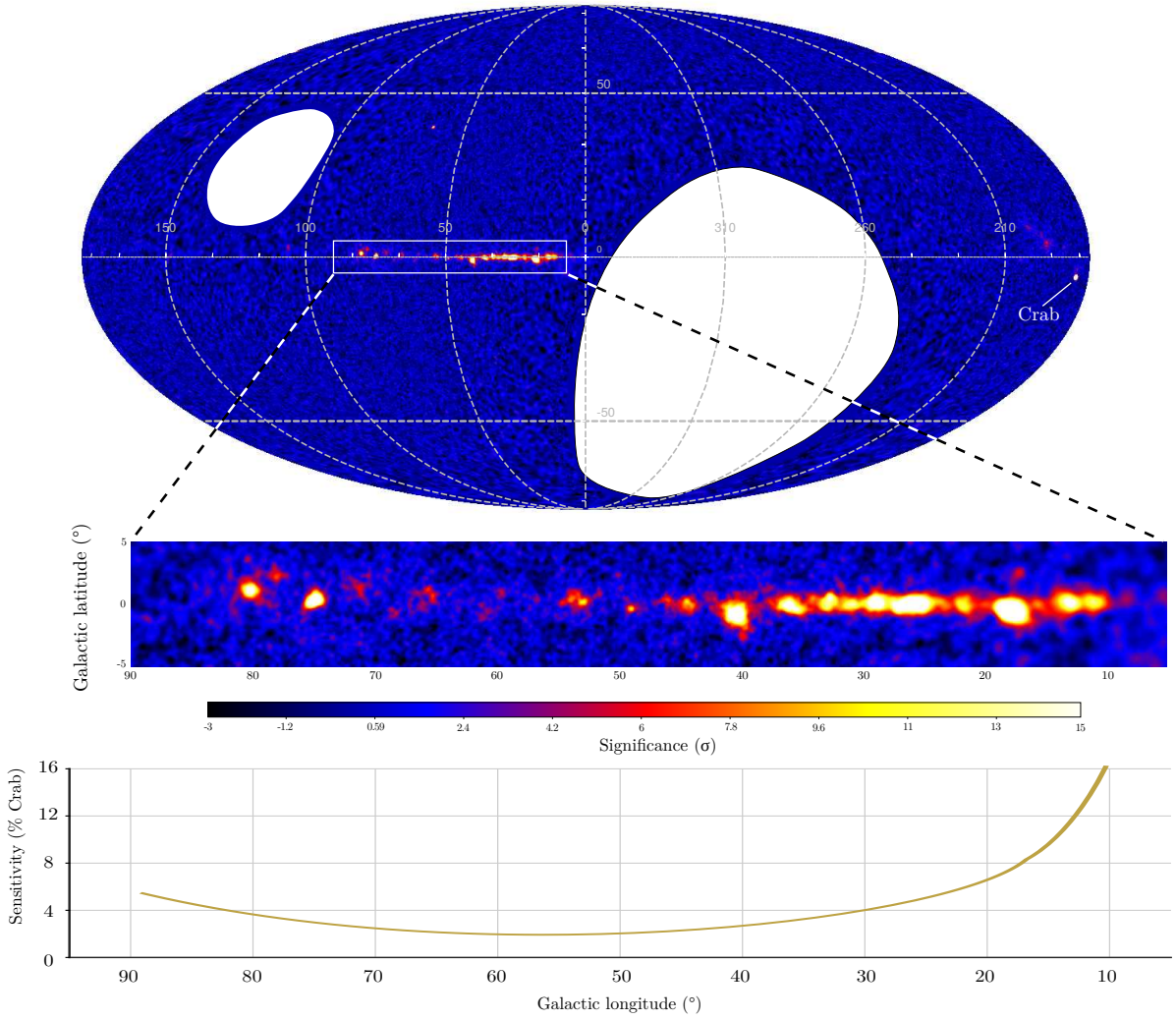

Figure 4.2: HAWC all-sky map with 1128 days of data and using events falling in nHit bins 4 to 9, in galactic coordinates and Mollweide projection. The part of the galactic plane in the white rectangle is used for the comparison with the HGPS. The bottom plot shows the HAWC sensitivity in % Crab for this region made in the same condition as the HAWC catalogue [7]. Here the Crab integrated flux above 1 TeV is $1.86.10^{-11}$ cm^{-2} s^{-1} as reported by HAWC [8].

4.3 Comparison of the γ-ray emission detected by HAWC and CO emission

Most of the interstellar gas in our galaxy is molecular hydrogen H_2, contained in Giant Molecular Clouds (GMC). These massive clouds of gas and dust have a typical size of 50 to 200 pc and a mass ranging between 10^4 and 10^6 solar masses. They are the place of star formation. In addition, they are the source of much of the diffuse galactic γ-ray emission [54]. The dominant processes by which cosmic rays interact with the interstellar medium and produce γ rays, are high-energy electron bremsstrahlung, inverse Compton interactions with low-energy photons and nucleon-nucleon interactions. For the later, molecular clouds are favourable environments. Hence, it is interesting to compare the galactic gas distribution, and the γ-ray emission detected by HAWC.

However, H_2 is not easily observable because this molecule has no electric dipole moment due to its symmetric shape. For this reason, it does not emit radiation from neither vibrational nor rotational transitions. However, CO emits radiation through a rotational transition (J=1→0) when excited by collisions with hydrogen molecules. Hence CO emission is used to trace H_2 molecular clouds. The abundance of CO is typically about $7.2.10^{-5}$ for one hydrogen molecule. Two isotopes are mainly used: ^{12}CO and ^{13}CO. The main difference is that ^{12}CO is optically thick while ^{13}CO is optically thin, the first one being in average ~60 times more abundant than the second one [67]. Here for a global visualisation of the galactic plane, I use the latest ^{12}CO survey by Dame, Hartmann and Thaddeus [38]. It is a combination of 32 surveys obtained with two different instruments, the CfA 1.2 m millimeter-wave telescope in the USA and the Cerro Tololo Inter-American Observatory in Chile, over the last 20 years. It provides a composite ^{12}CO map of the galactic plane, showing the main structural features of the molecular galaxy. This map is compared to the HAWC TeV γ-ray emission.

The composite spatial velocity-integrated map is shown in the top panel of Figure 4.3, for the region of the galactic plane detected by HAWC ($10° < \ell < 70°$) displayed on the bottom panel. The longitude and latitude profiles of both emissions are also plotted in between the two maps. The longitude profiles are normalised to the average value in the region with $66° < \ell < +68°$ where HAWC does not detect any sources. Removing all HAWC sources would be required to perform a proper comparison between them, but we can already see that they seem to follow the same trend (the dashed black curve on top of the longitude profiles in Figure 4.3 is drawn to guide the eye). It may support the idea that the galactic HAWC sources lie on a large scale γ-ray diffuse emission of galactic origin.

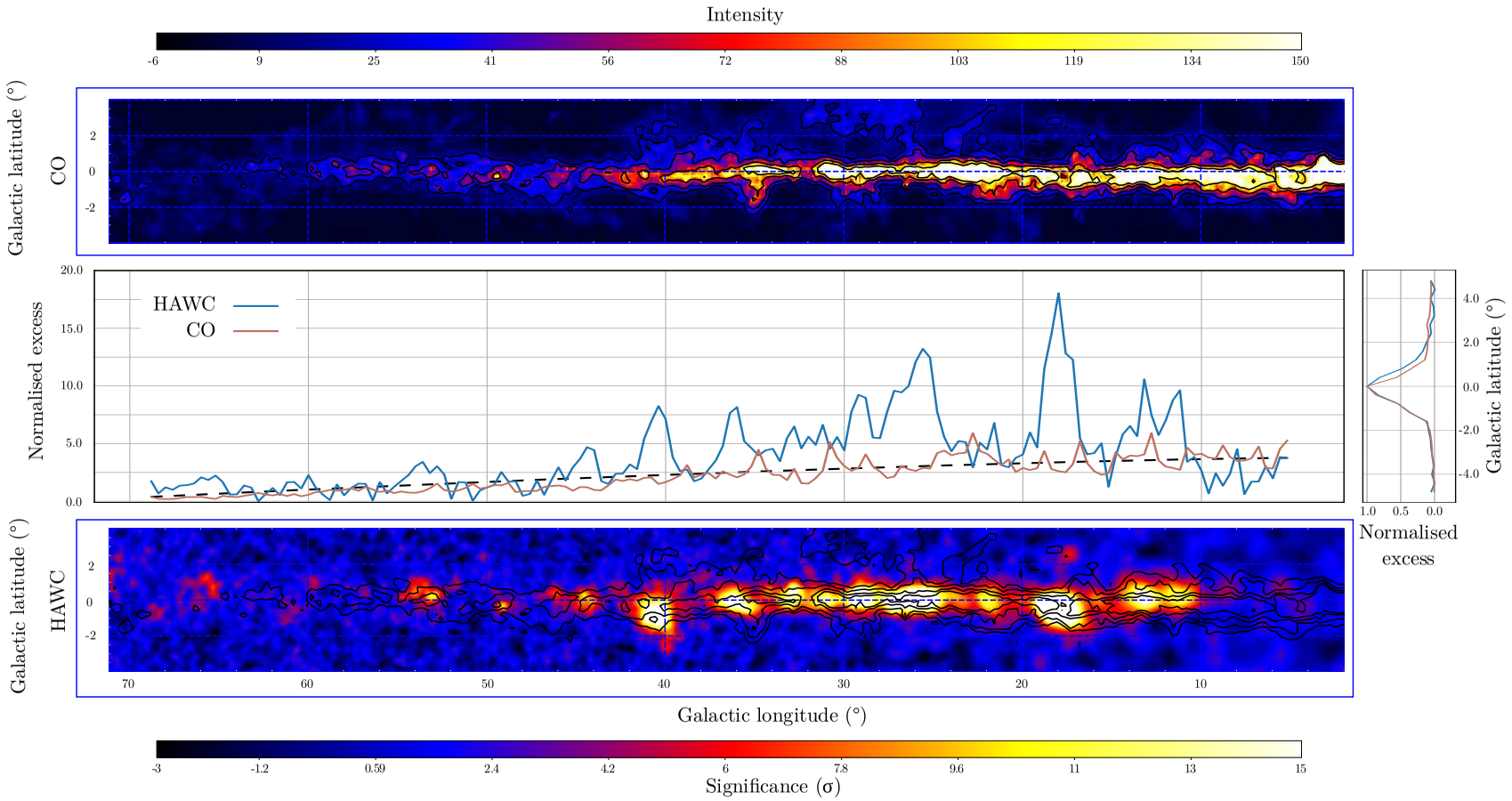

Figure 4.3: Comparison of HAWC γ-ray emission with the CO emission of the galactic plane. The top panel corresponds to the ^{12}CO map [38]. The bottom pannel is the HAWC significance map. The CO contours, in black, are superimposed to the HAWC map. The middle panel show the excesses longitude profiles of the ^{12}CO (brown) and the HAWC skymaps (blue) for $72° < l < 5°$ and integrated between $-1° < b < +1°$. They are normalised to the region with $66° < \ell < 68°$ where there are no HAWC sources. The latitude profiles (side panel) are performed for $-5° < b < +5°$ and integrated between $72° < l < 5°$. The profiles are using a binning of 0.4°. The HAWC profile is corrected for the acceptance. The dotted line highlight the general trend of the profiles.

4.4 Comparison of the galactic plane detected by HAWC and H.E.S.S.

Figure 4.4 shows the significance maps of the H.E.S.S. and the HAWC galactic planes. For a good visualisation of the part of the galaxy surveyed by both instruments and the overlapping region, Figure 4.16 at the end of this section shows their horizon for a 5σ detection of sources with luminosity of 10^{34} erg s^{-1}. This figure will be discussed in more details later. To study the synergies between the results obtained from the two different instruments, their skymaps were made as comparable as possible in terms of energy range, resolution and background estimation method.

4.4.1 Comparable maps in terms of energy

The first step is to make maps over a similar energy range. Since I use events belonging to the nHit bins 4 to 9 from HAWC as a compromise between enough statistics, good quality reconstruction, and reasonable PSF, I use from H.E.S.S. events above 1 TeV. ImPACT reconstruction is more suited for the highest energies than the standard reconstruction method used in most of H.E.S.S. publications, and in the HGPS paper in particular. All H.E.S.S. maps used in the analysis and displayed hereafter use events above 1 TeV reconstructed with ImPACT.

Hence, the maps of the galactic plane in Figure 4.4 are made over a similar energy range. The H.E.S.S. map uses a correlation radius of 0.1°, similarly to the published HGPS. At a first glance, they look quite different: the HAWC galactic plane appears broader than H.E.S.S. In some cases HAWC cannot resolve regions where H.E.S.S. detects several sources. For instance, the region around $\ell = 26°$ shown in Figure 4.5(a) is a good illustration: HAWC resolves only 3 sources while H.E.S.S. resolves 11 sources. On the other hand, HAWC detects some sources that have not been reported in the HGPS, as illustrated in Figure 4.5(b) when comparing the first and second rows. There are several reasons for that:

- Their sensitivity peaks at a different energy, higher for HAWC than for H.E.S.S.: above 10 TeV, HAWC achieves better sensitivity than long duration observations by H.E.S.S. [7]. Hence, HAWC is more sensitive than H.E.S.S. to detect sources that emit at higher energies. On the other hand, if they have a soft spectrum they may not emit any significant emission at high energy anymore and can only be seen by H.E.S.S.

- Because HAWC has such a large field of view, it is able to observe and to perform the analysis of very large sources, even of the scale of the whole sky like diffuse γ-ray emission. On the contrary, H.E.S.S. and IACTs in general are limited to sources of the size of their field of view.

- H.E.S.S. has an angular resolution almost an order of magnitude better than HAWC, so point-like sources appear more extended in the HAWC map since its PSF is wider.

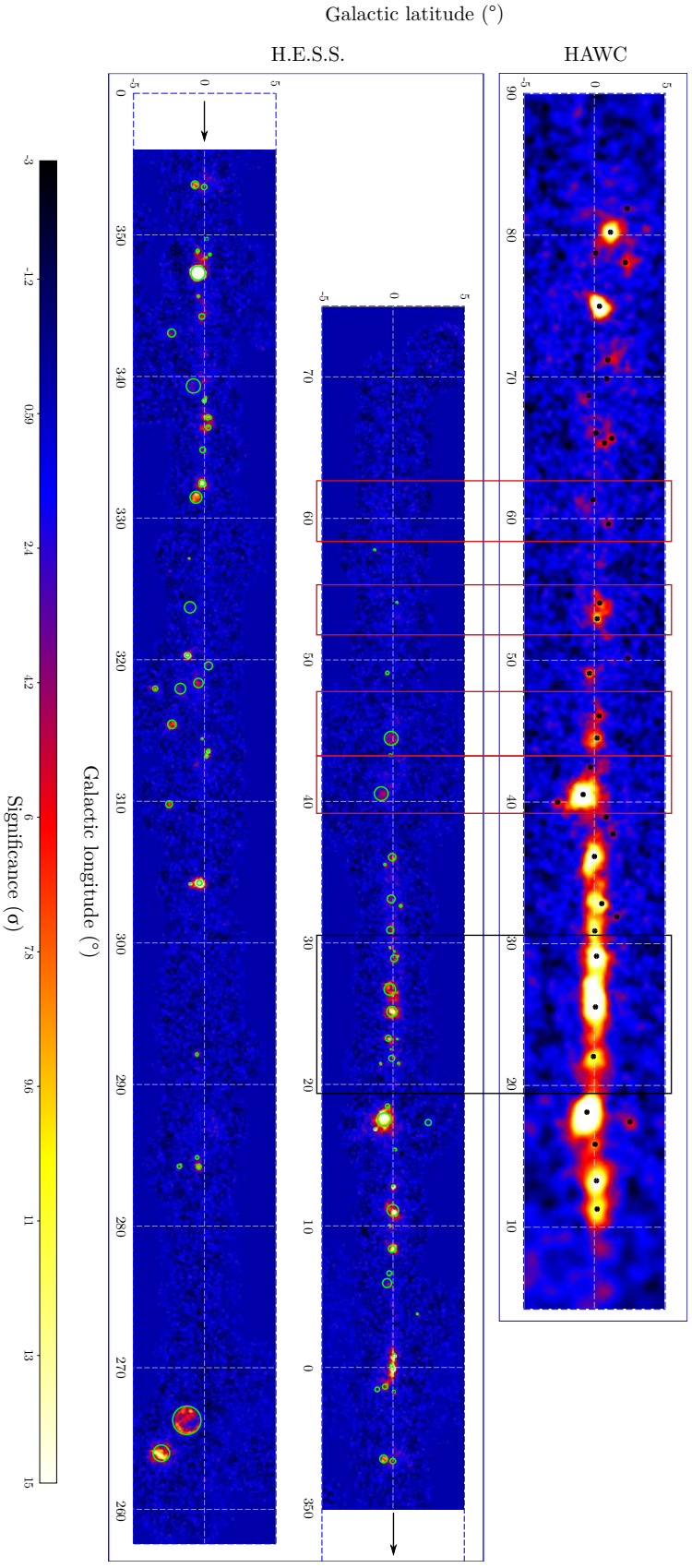

Figure 4.4: Top: HAWC significance map of the galactic plane with 1128 days of data and using events in nHit bins 4 to 9. The black dots are the location of the HAWC sources [7]. Bottom: HGPS for E > 1TeV, using ImPACT reconstruction and a correlation radius of 0.1°. The green circles are the 68% containment of the H.E.S.S. sources [47]. The regions in the black and red boxes are shown in more details in Figure 4.5(a) and (b) and in Figure 4.12.

- Their background estimation is adapted to the type of instrument that is considered. The H.E.S.S. ring background method is more suited for isolated point-like sources than extended sources: it tends to remove large scale emission around sources including the source itself if very extended, wrongly interpreted as background signal.

In total, for $72° < \ell < 0°$, H.E.S.S. detected 34 sources: for 27 of them HAWC detects significant emission, even though only 15 are resolved. Thus, 7 H.E.S.S. sources do not show any significant γ-ray emission in the HAWC map. On the other hand, HAWC detected 31 sources in the galactic plane for the same range of longitude. Only 15 of them have a counterpart in the H.E.S.S. map, the other 16 sources being present only in the HAWC map. This important discrepancy between the two catalogues will be further discussed in section 4.4.4.

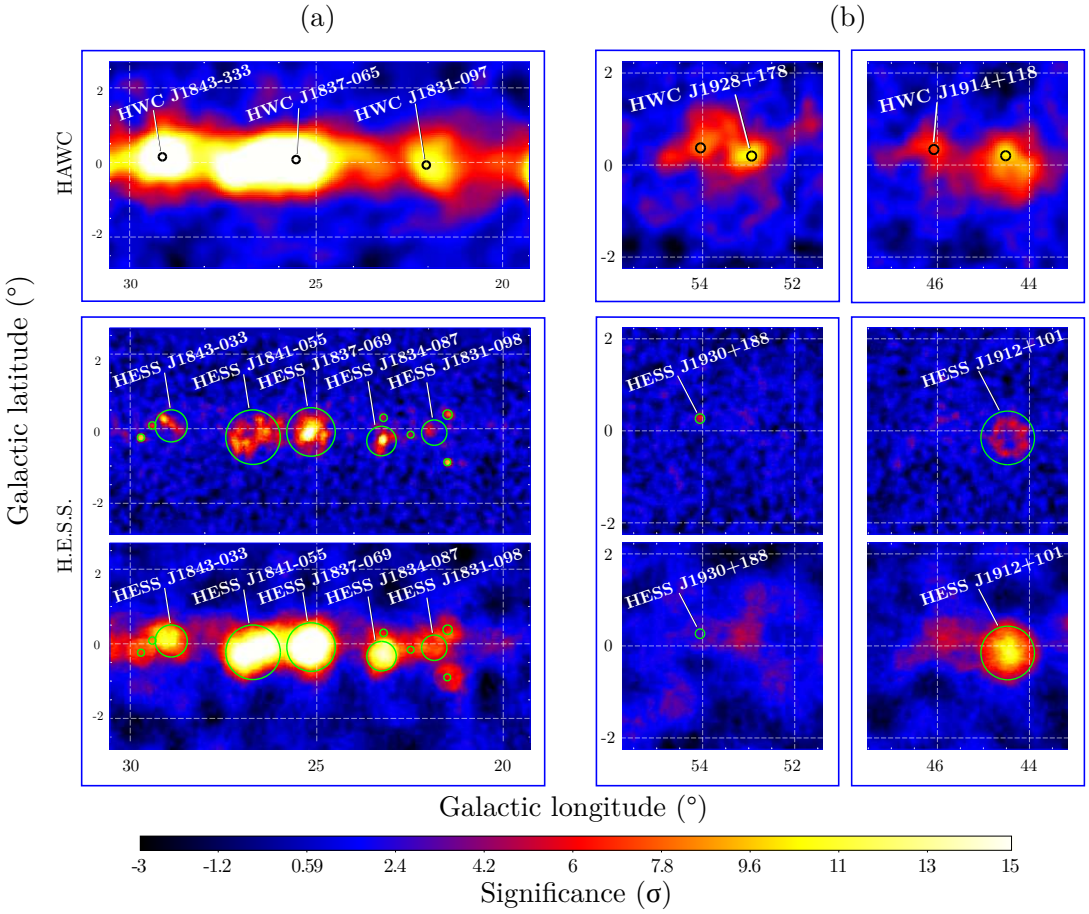

Figure 4.5: The top and middle map correspond to the HAWC and H.E.S.S. map from Figure 4.4. The bottom map is the same H.E.S.S. map using a correlation radius of 0.4°. (a) corresponds to the region in the black box of Figure 4.4. It illustrates the difference in angular resolution for both instruments in a region where HAWC cannot resolve the H.E.S.S. sources. In the bottom map, the H.E.S.S. sources are not resolved anymore, similarly to the HAWC ones. (b) corresponds to the region in the second and third red boxes of Figure 4.4. It shows 2 HAWC sources that are not present in the H.E.S.S. map (middle), but appear if a correlation radius of 0.4° is used (bottom map).

4.4.2 Comparable maps in terms of angular resolution

The resolution of H.E.S.S. is 0.06° at 1 TeV using ImPACT reconstruction. This is much better than the resolution of HAWC, which is 0.4° for nHit bin 4. To make the maps comparable, I degraded the H.E.S.S. resolution by applying a top hat function with a correlation radius of 0.4°, equivalent to the HAWC PSF extension at these energies. As seen in Figure 4.5, they look much more similar. Indeed, most of the structures can be found in both maps:

- H.E.S.S. sources close to each other by less than the correlation radius are merged, making them appearing unresolved like in the HAWC map. This is illustrated on the last row of Figure 4.5(a) where a correlation radius of 0.4° is applied to the H.E.S.S. map.
- It also reveals some extended hotspots close to sources detected by HAWC. For example, it is the case of the two sources depicted in Figure 4.5(b): significant emission appears in the H.E.S.S. map on third row less than 0.2° away from a HAWC source. Although it could also amplify background fluctuations, the fact that it is coincident with a rather bright source already detected by HAWC is a clear hint.

4.4.3 Comparable maps in terms of background estimation method

The previous section showed that making the maps comparable in terms of energy range and angular resolution leads to two very similar maps: HAWC and H.E.S.S. globally see the same sky. Nonetheless, the remaining differences between the maps may be due to the difference in sensitivity as a function of energy: sources with soft spectrum are favourable to H.E.S.S. while sources with hard spectrum are favourable to HAWC. The differences may also partially come from the data analysis and the map making process, described in Sections 2.1.2 and 2.1.3 for H.E.S.S. and Section 2.2.3 for HAWC. In that regard, the background estimation plays an important role. To assess this effect, I produced a map with the HAWC data, applying the H.E.S.S. ring background estimation, and a map with the H.E.S.S. data using a method equivalent to the HAWC direct integration background method. In both cases, an exclusion region is used to avoid any contamination from the galactic plane and the known TeV sources to the background estimation. It is defined by the known H.E.S.S. sources plus a band of 2° around the galactic plane, for -1° < b < +1° as illustrated in Figure 4.6, where most of the HAWC sources are located.

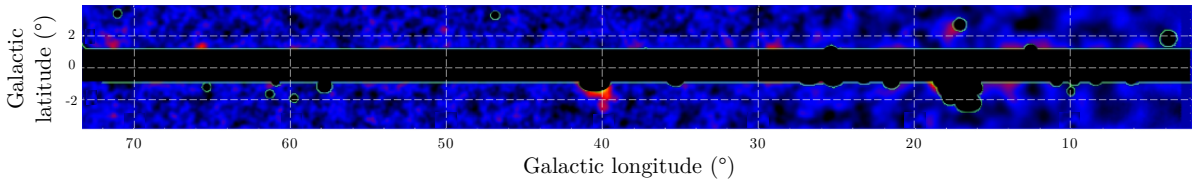

Figure 4.6: Exclusion regions used in this study, superimposed on the HAWC map.

HAWC map using H.E.S.S. background method

To be able to properly compare the HAWC and H.E.S.S. maps using the ring background method, the ring needs to be applied in a similar way and with the same parameters. Hence, I created a H.E.S.S. map where I first combined all the observation runs and then applied a fix ring with the same parameters on both H.E.S.S. and HAWC maps. It ensures that the same regions of the sky are used to estimate the background. I illustrate in Figure 4.7 the ring used to estimate the background on a very specific location in the sky, the location of the pulsar PSR J1928+1746 which is coincident with the HAWC source 2HWC J1928+177. This region will be studied in more detail in the next chapter.

I could evaluate that, when using an adaptive ring on the H.E.S.S. data with the 2° band as exclusion region, the average ring over all the observation runs ends up to have an inner radius of 1.1°. This is illustrated on Figure 4.7(b), showing the adaptive ring used to evaluate the background at the location of the pulsar. A fix ring can be given a slightly larger radius: it maximises its useful area outside the exclusion region. A larger ring has also the advantage of using regions further away from the galactic plane, and avoid considering galactic diffuse emission or signal from a source itself as background. On the other hand it cannot be too big

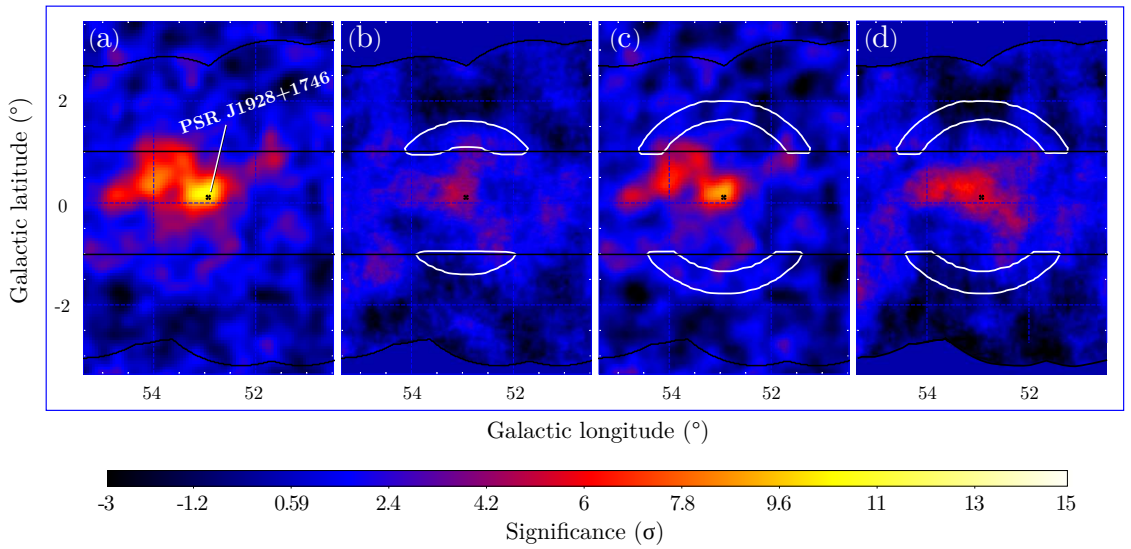

Figure 4.7: Illustration of the size of the ring for the background estimation at the location of PSR J1928+177, coincident with the HAWC source 2HWC J1928+177. The black lines represent the exclusion region and delimit the H.E.S.S. field of view. (a) is the HAWC map (1128 days of data, events in nHit bins 4 to 9) using its direct integration method for the background estimation. (b) is the H.E.S.S. map (E > 1 TeV, ImPACT reconstruction) with a correlation radius of 0.4° using the ring background method applied on each observation run separately, with an adaptive radius. (c) and (d) are the HAWC and H.E.S.S. maps using a fix ring with the same parameter (inner radius of 1.5° and 0.4° thickness); for H.E.S.S. it is applied after the combination of all observation runs

because of the limited H.E.S.S. field of view. As a compromise, a fix ring of inner radius 1.5° radius and 0.4° thickness is used, illustrated in Figure 4.7(c) and (d).

There are several comments to make by comparing the different maps of this figure for the different ways of applying the ring, and for the two different background methods:

- Looking only at H.E.S.S. maps: comparing the adaptive ring applied on H.E.S.S. data on each run separately (Figure 4.7(b)) and the fix ring applied on H.E.S.S. data after combining the runs (Figure 4.7(d)) shows on this particular region that there is more significant emission in the second case.
- Looking only at HAWC maps: the HAWC maps with the background estimated using a fix ring (Figure 4.7(c)) shows that the background is overestimated compared with the direct integration background method (Figure 4.7(a)) leading to a less significant signal.
- Comparing HAWC and H.E.S.S. using the same background method and the same ring parameters: more background has been subtracted to the HAWC map and less background has been subtracted to the H.E.S.S. map. They look closer (Figures 4.7(c) and (d)) than when using their respective background method (Figures 4.7(a) and (b))

The HAWC maps with two different background estimation methods are shown in Figure 4.8, namely the direct integration method on the top map and the ring method on the bottom map. Between the maps are plotted the longitude and latitude profiles. They highlight a systematic decrease of the excess of the order of 5-15% by using the ring method. It is a clear confirmation that the H.E.S.S. ring method tends to remove too much signal from extended sources or from an underlying large scale emission.

H.E.S.S. map using HAWC background method

The other way around is also possible: a map with H.E.S.S. events using the HAWC background estimation method. The closest method to the direct integration is to use the H.E.S.S. acceptance map as background estimation, also referred to as *field-of view background method* [23]. The acceptance is the expected events from cosmic-ray background. It is estimated by looking at regions of the sky at similar zenith angle, without known VHE γ-ray sources. It is normalised to the total number of events outside the exclusion regions, to account for differences in optical efficiency or observation time between runs [47]. Figure 4.9 gives an example of a given field of view without known sources. The events are accumulated to give the two-dimensional γ-ray acceptance map on the top left. The acceptance can be modeled by a one-dimensional curve as a function of the center of the camera, assuming it is radially symmetric. An example of such curves is shown on the right plot of the figure for different zenith angle ϕ_z and different energies. These curves can be used to produce a model acceptance map for the corresponding energy and zenith angle, as shown on the bottom left.

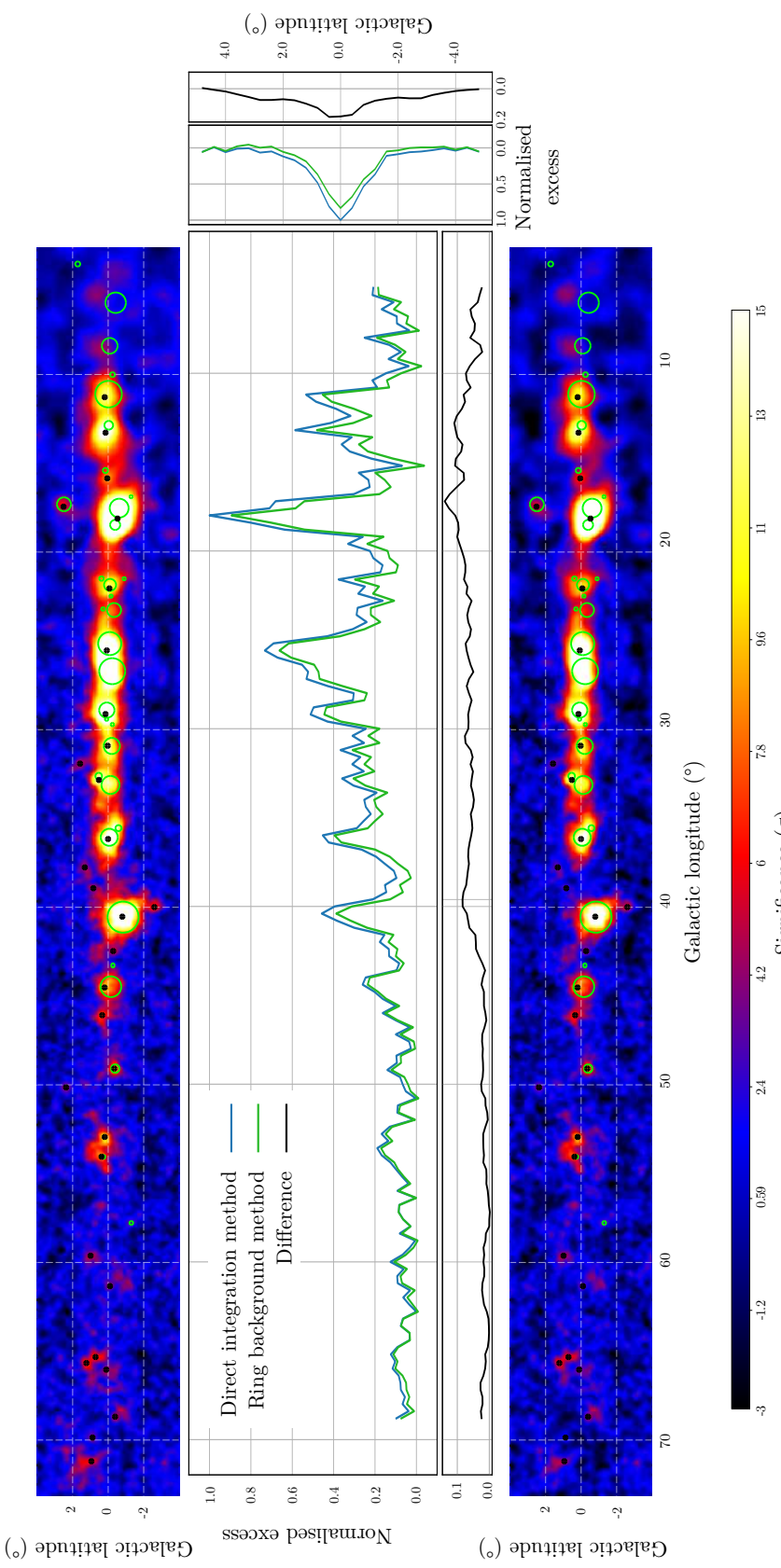

Figure 4.8: HAWC galactic plane using two different background estimations: top panel is the HAWC significance map using its traditional direct integration method to estimate the background. It corresponds to the blue excess profiles on the middle panel. Bottom panel is the HAWC significance map using the H.E.S.S. ring background method. It corresponds to the green excess profiles on the middle panel. The longitude profiles (middle panel) are done for $72° < l < 5°$ and integrated between $-1° < b < +1°$. The latitude profiles (side panel) are done for $-5° < b < +5°$ and integrated between $72° < l < 5°$. All profiles are using a binning of 0.4° and are corrected for the acceptance. They are normalised to the maximum value of the highest profile. The black curves are the difference between the two profiles.

It is not strictly identical to the direct integration method in the sense that the background map made with this method uses the data themselves integrated over 2h, and is constantly updated. However, using an average acceptance assumes that its shape does not change with time. It is not an instantaneous measurement and does not take into account the status of the instrument at the time of observation. Moreover, the normalisation step required to transform the one-dimensional acceptance curve into the actual expected background count map uses the number of events outside exclusion regions in the field of view, which has a limited size. Therefore, it can also take large scale emission as background.

Figure 4.11 shows the H.E.S.S. map using the two different background estimations: its traditional adaptive ring on the top map and the acceptance on the bottom map. To assess that the background is correctly evaluated, Figure 4.10 displays the distribution of the significance for both maps outside the exclusion regions. The fit of a gaussian function to each distribution gives a mean $\mu \simeq 0$ and $\sigma \simeq 1.1$ in both cases. It is slightly higher than 1, which would be the expected value for σ in the case of pure background. It means that there is likely some signal remaining or some small systematics in the background evaluation. Looking at the shape of the distributions, there is an offset to the gaussian around -6σ in the case of the background estimated using the ring, that almost disappear in the case of the field of view method. In any case, this should not have an important effect on the maps and the results presented here.

The longitude and latitude profiles of both maps are also shown in between the maps of Figure 4.11. Using the acceptance map as an estimation of the background increases the excess to 15% overall compared to the adaptive ring method. It increases up to 50% for example in the case of the 4 hotspots shown in more details in Figure 4.12. They appear less than 0.5° away from a known HAWC source: HWC J1947+249, HWC J1928+178, HWC J1914+118, HWC J1909+083*. All of them are new TeV sources detected by HAWC. In particular, HWC J1928+178 is a serious candidate for being associated with the pulsar PSR J1928+1746. This sources will be discussed in detail in the next chapter. These 4 potential sources are completely absent on the H.E.S.S. maps using the adaptive ring method, on the second raw. They appear already by using a correlation radius of 0.4°, visible on the third row, and they are very bright on the H.E.S.S. map using the acceptance map as background, on the fourth row, with a peak significance of more than 5σ.

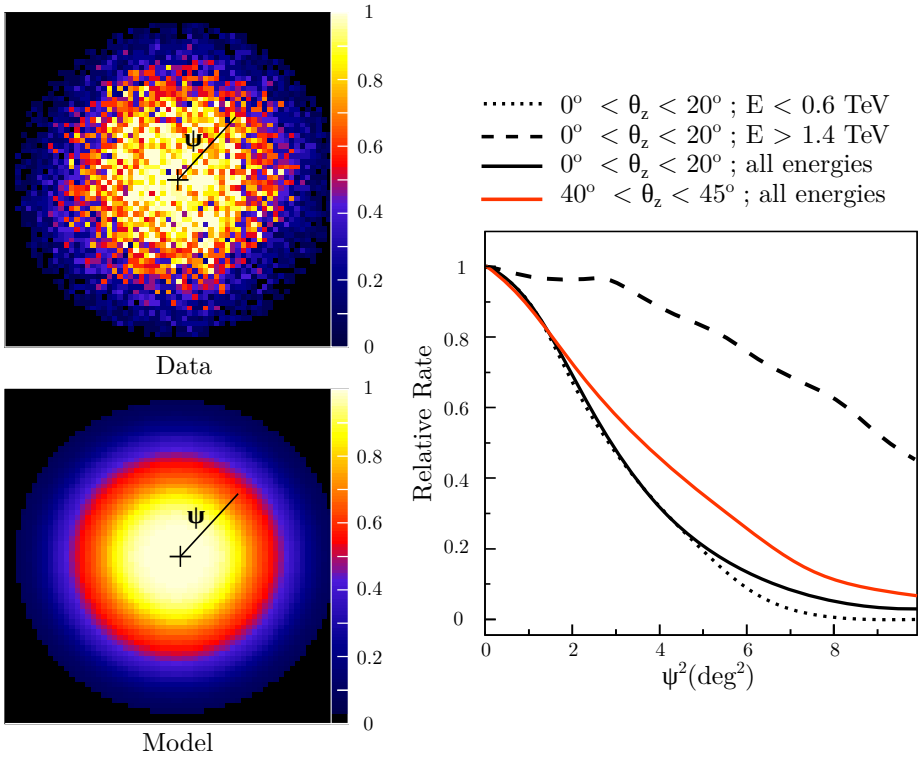

Figure 4.9: H.E.S.S. γ-ray acceptance map. The one-dimensional acceptance curves on the plot are made using the two-dimensional γ-ray acceptance map on the top left where γ-like events are accumulated. They depend on the zenith angle θ_z and the energy and assume that the acceptance is radially symmetric. These curves are used to make the model acceptance map on the bottom left for the relevant zenith angle and energy. Adapted from [23].

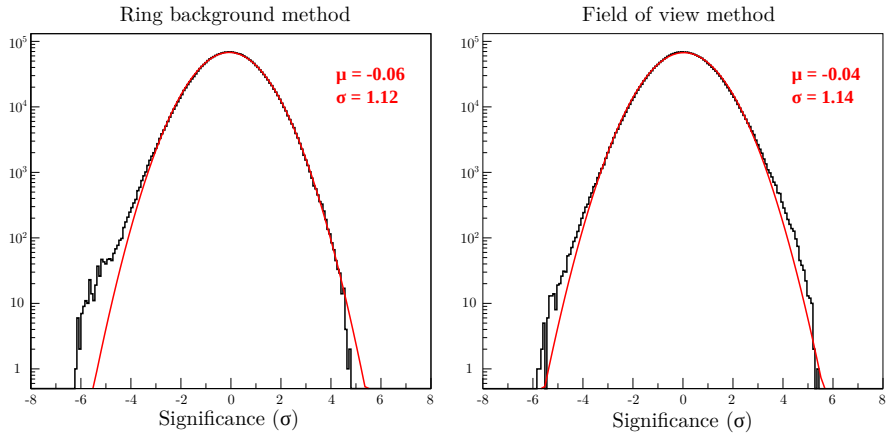

Figure 4.10: Distribution of the significance outside the exclusion regions for H.E.S.S. maps using two different background methods. The red curves are a fit with a gaussian function.

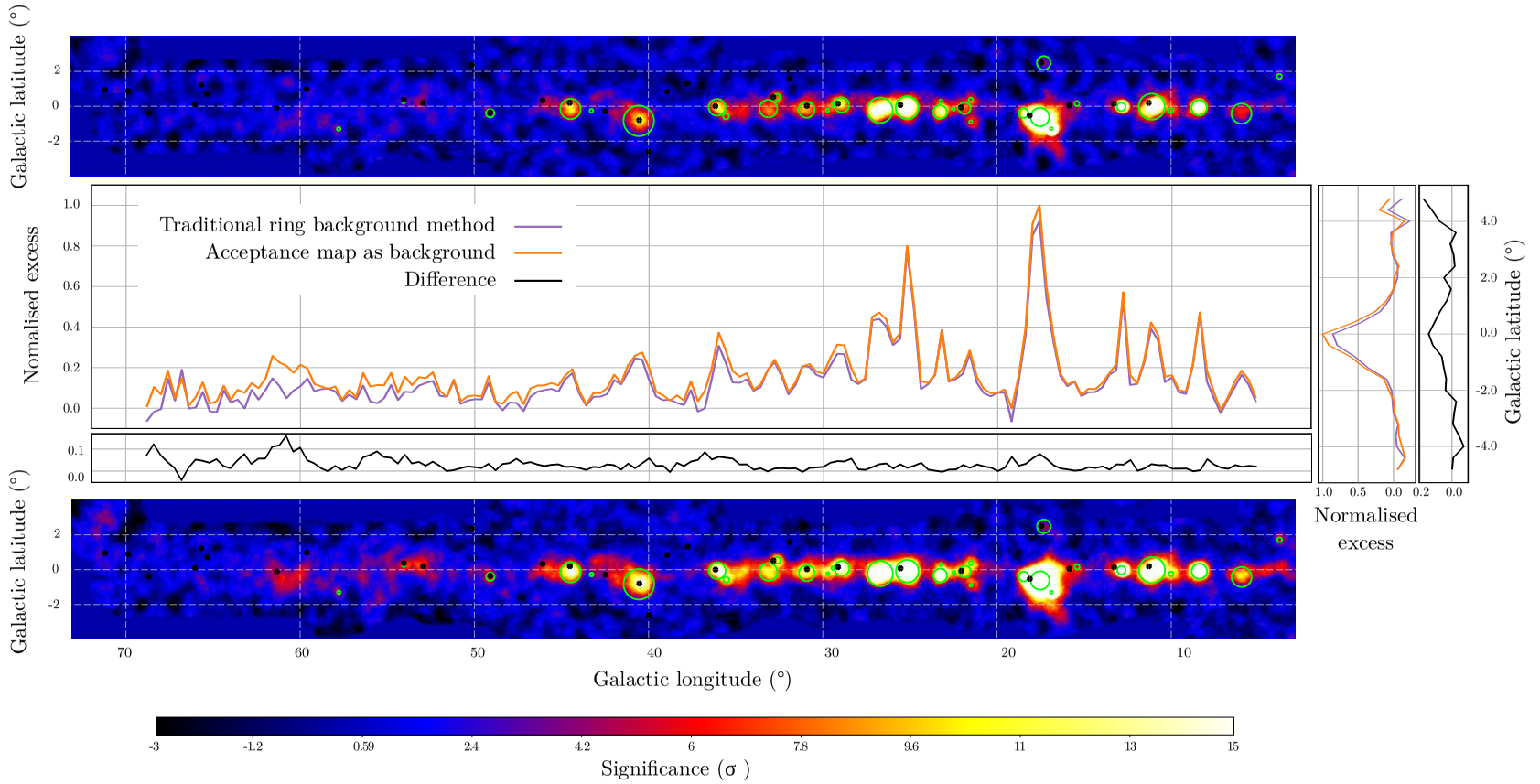

Figure 4.11: H.E.S.S. galactic planes using two different background estimations: top pannel is the H.E.S.S. significance map using its traditional adaptive ring background method. It corresponds to the orange excess profiles on the middle panel. Bottom panel is the H.E.S.S. significance map using the acceptance maps as background. It corresponds to the purple excess profiles on the middle panel. Both maps are using ImPACT reconstruction and a correlation radius of 0.4°. The longitude profiles (middle panel) are performed for 72° < l < 5° and integrated between -1° < b < +1°. The latitude profiles (side panel) are performed for -5° < b < +5° and integrated between 72° < l < 5°. All profiles are using a binning of 0.4° and are corrected for the acceptance. They are normalised to the maximum value of the highest profile. The black curves are the difference between the two profiles.

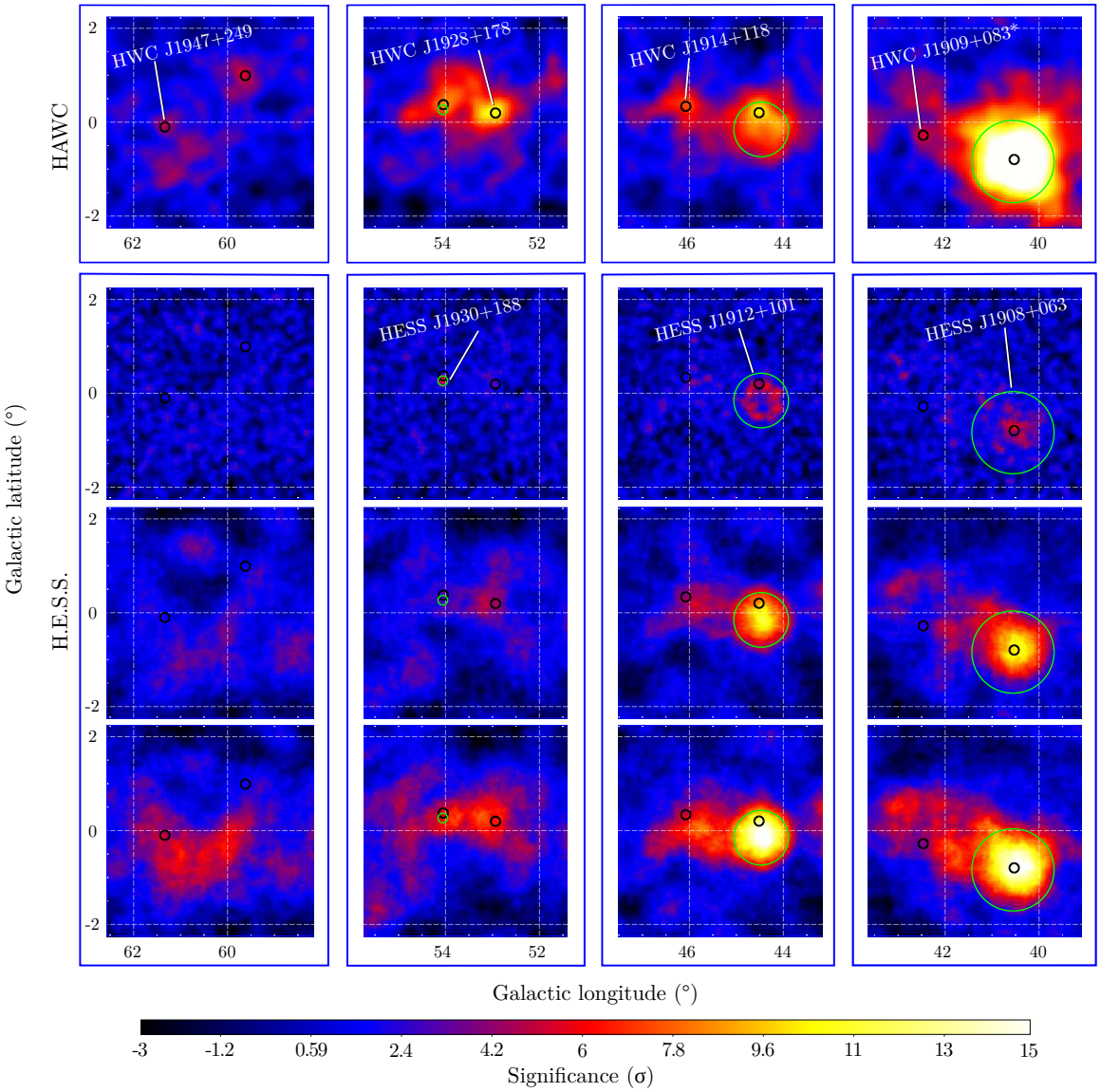

Figure 4.12: The maps on the first and second rows are the regions of the HAWC and the H.E.S.S. maps in the red boxes in Figure 4.4. A HAWC source, visible on the first row, has not been detected in the HGPS using the traditional background ring method as depicted on the second row (E > 1 TeV, using ImPACT reconstruction, 0.1° correlation radius). The maps on the third row are the same H.E.S.S. maps but using a correlation radius of 0.4°. In the fourth row, the same H.E.S.S. data are used but the background is estimated using the acceptance map (0.4° correlation radius).

4.4.4 Summary and discussion

Figure 4.14 gathers all the important maps from the different steps detailed earlier and Figure 4.15 presents the sensitivity curve for some of them. From top to bottom, in Figure 4.14:

- The first map shows the HAWC galactic plane with 1128 days of data and using events in nHit bins 4 to 9 and the direct integration method for the background estimation. The light brown curve in Figure 4.15 shows the HAWC sensitivity and the seven H.E.S.S. sources undetected by HAWC represented by the green dots. They lie way below the HAWC sensitivity curve: they are not detectable by HAWC.

- A map using the same HAWC data, but applying the ring method to estimate the background. It permits an assessment of the effect of the ring background method: a systematic decrease of 5 to 15% is observed when using the ring method, meaning that this method seems to overestimate the background.

- The third map is the H.E.S.S. galactic plane for E > 1 TeV, using ImPACT reconstruction and a correlation radius of 0.1° with the ring background method, using an adaptive ring applied on each observation run separately. The dark blue curve in Figure 4.15 shows the corresponding H.E.S.S. sensitivity at $b = 0$. There are 16 sources detected only by HAWC, represented by the orange dots. Apart from the ones around ~70° most of them are above the H.E.S.S. sensitivity curve (dark blue curve). It means that if they were of the order of 0.1° in size, H.E.S.S. would have detected them. Therefore they are likely more extended.

- For the sake of making the HAWC and H.E.S.S. maps comparable in terms of angular resolution, the previous map has been degraded using a correlation radius of 0.4° to give the fourth map. It already shows that it is more favourable to extended sources since some H.E.S.S. sources cannot be resolved any more and some extended emission appears that could be consistent with some HAWC sources

- The last map uses the same H.E.S.S. data with a correlation radius of 0.4° but takes the acceptance map as the background. The H.E.S.S. sensitivity curve for such a correlation radius and for this background estimation is the light blue curve in Figure 4.15. Six of the sources detected only by HAWC appear now above this sensitivity curve. They can be identified on the map in Figure 4.4 by the orange arrows and vertical dotted lines. However, only 3 of them actually show some significant emission close to a HAWC source: HWC J1928+178, HWC J1914+118, HWC J1909+083*. Amongst the three others, HWC 1913+050* is the well known binary system SS 433 [6]. Some hint of emission is already visible at 3σ in the H.E.S.S. above 2.5 TeV, as shown in Figure 4.13 using the HAWC analysis presented here. More observations on the region could be a key factor. The 2 remaining ones, HWC 1859+057 and HWC 1843-001 do not show any significant emission

in the H.E.S.S. maps. Note however that this sensitivity curve is done at $b = 0$ and these sources are offset by more that 1.5°.

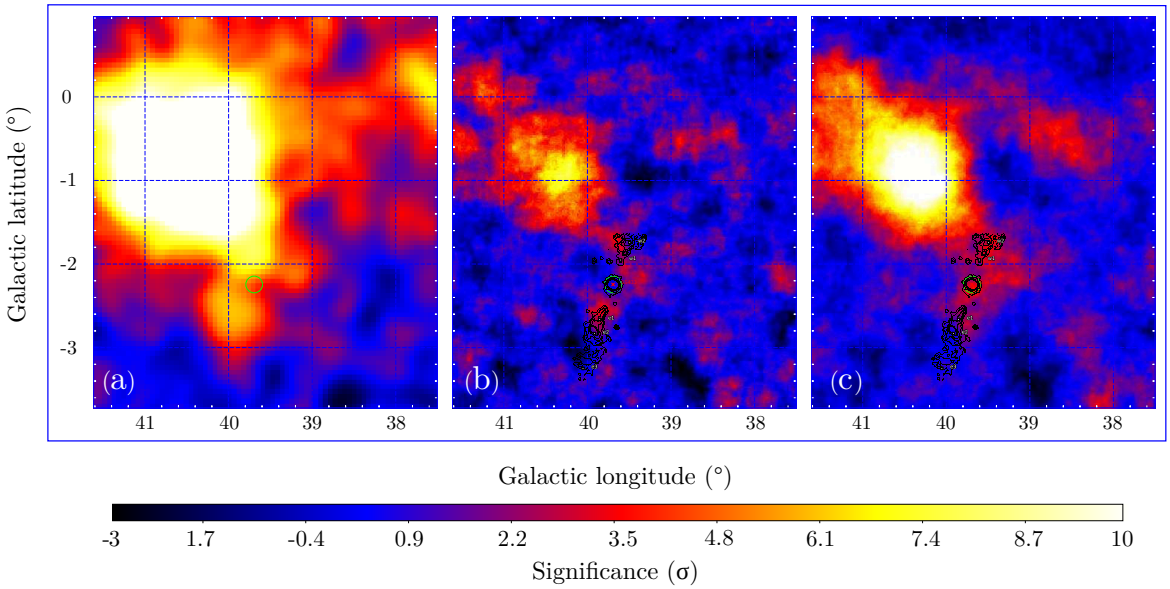

Figure 4.13: HAWC and H.E.S.S. Maps of the region of SS 433. (a) is the HAWC map for bins 4 to 9. (b) and (c) and H.E.S.S. maps above 2.5 TeV using ImPACT reconstruction using HAWC background method, with a correlation radius of 0.2° and 0.4° respectively. Contours are X-ray data from ROSAT [29].

Figure 4.14: HAWC and H.E.S.S. galactic planes using different background estimations. From top to bottom:
1 - HAWC galactic plane with 1128 days of data and using events in nHit bins 4 to 9 and the direct integration method for the background estimation.
2 - Same HAWC data but using the H.E.S.S. ring background method.
3 - H.E.S.S. galactic plane for E > 1 TeV, using ImPACT reconstruction and a correlation radius of 0.1°; the ring background method is applied on each observation run separately, with an adaptive radius.
4 - Same H.E.S.S. data but using a correlation radius of 0.4°
5 - Same H.E.S.S. data but using the acceptance map as the background
The green circles are the 68% containment of the H.E.S.S. sources and the black dots are the location of the HAWC sources. The green arrow and vertical dotted line point to some H.E.S.S. sources undetected by HAWC. The orange arrow and vertical dotted line point to some HAWC sources undetected by H.E.S.S. and that are above the sensitivity curve of H.E.S.S. in case 5 (light blue curve on Figure 4.15).

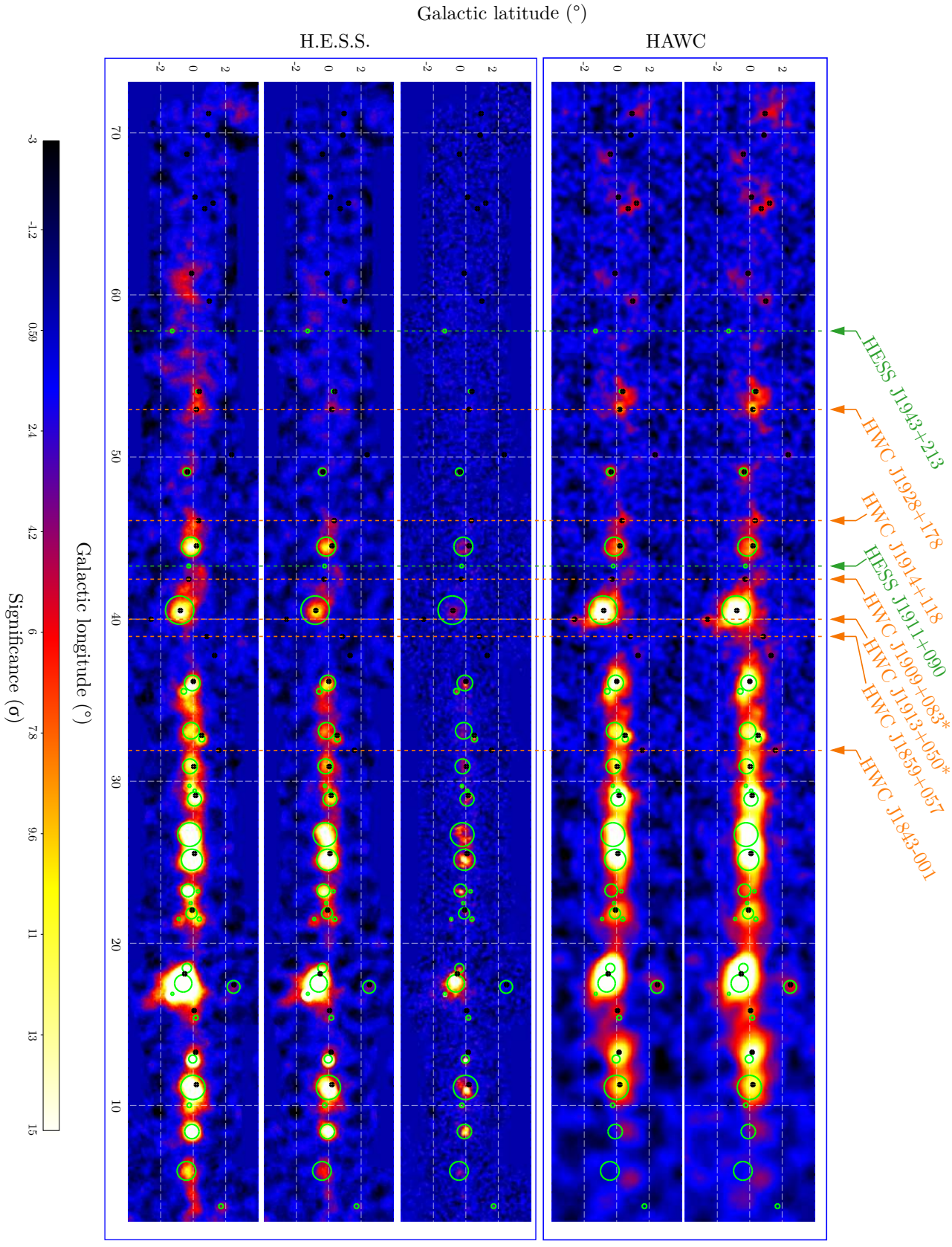
Galactic latitude (°)
H.E.S.S.
HAWC
Galactic longitude (°)
Significance (σ)
HESS J1943+213
HWC J1928+178
HWC J1914+118
HESS J1911+090
HWC J1909+083*
HWC J1913+050*
HWC J1859+057
HWC J1843-001

The sensitivity curves of Figure 4.15 are used to plot the horizons to detect a source with 5σ significance that have a γ-ray luminosity of 10^{34} erg s^{-1} in Figure 4.16. The very irregular shape of the H.E.S.S. curves is due to the very inhomogeneous exposure time along the galactic plane. The sources detected by H.E.S.S. and HAWC respectively for which a distance is known are also plotted with green and orange markers respectively.

The first and the last maps of Figure 4.14 are made in the most comparable situation: they have similar energy range, similar resolution and use the same background estimation method, here the HAWC method. Figure 4.17 shows the longitude and latitude profiles for these two comparable cases superimposed. They are normalised to the source HWC J1912+103/HESS J1912+101 at $\ell = 44.5°$ which is isolated, bright and extended. Moreover, the integrated flux above 1 TeV estimated by HAWC for HWC J1912+103 is $2.18.10^{-12}$ cm^{-2} s^{-1}. It is similar to the integrated flux above 1 TeV estimated by H.E.S.S. for HESS J1912+101 which is $2.49.10^{-12}$ cm^{-2} s^{-1}. Looking at the difference between the profiles, it seems well balanced around 0. There seems to be a good overall agreement. Nevertheless, looking at some sources or regions individually, there are some large differences: for $28° < \ell < 15°$ HAWC detects more emission than H.E.S.S.. For the regions $50° < \ell < 65°$, or for sources like HESS J1837-069 or HESS J1825-137, it is H.E.S.S. that detects more emission. They would require deeper study.

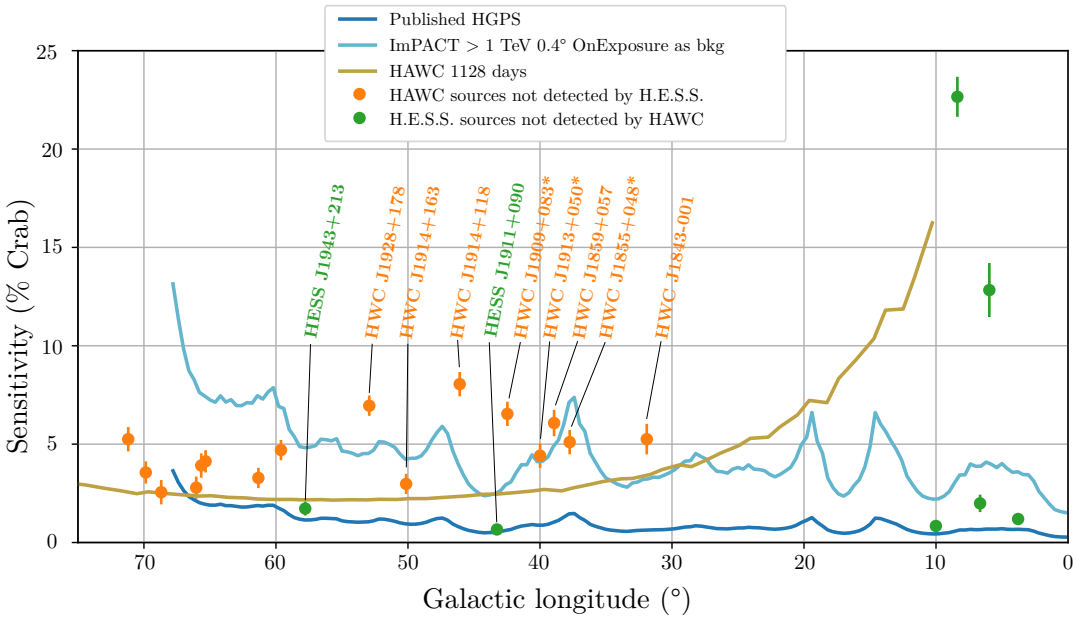

Figure 4.15: Sensitivity curves at $b = 0$ for HAWC (light brown) and H.E.S.S. in two different cases: the dark blue curve is the published HGPS sensitivity for a point-like source (identical to the bottom plot of Figure 4.1) ; the light blue curve is the sensitivity for energy above 1 TeV, with ImPACT reconstruction and using the acceptance map as background.

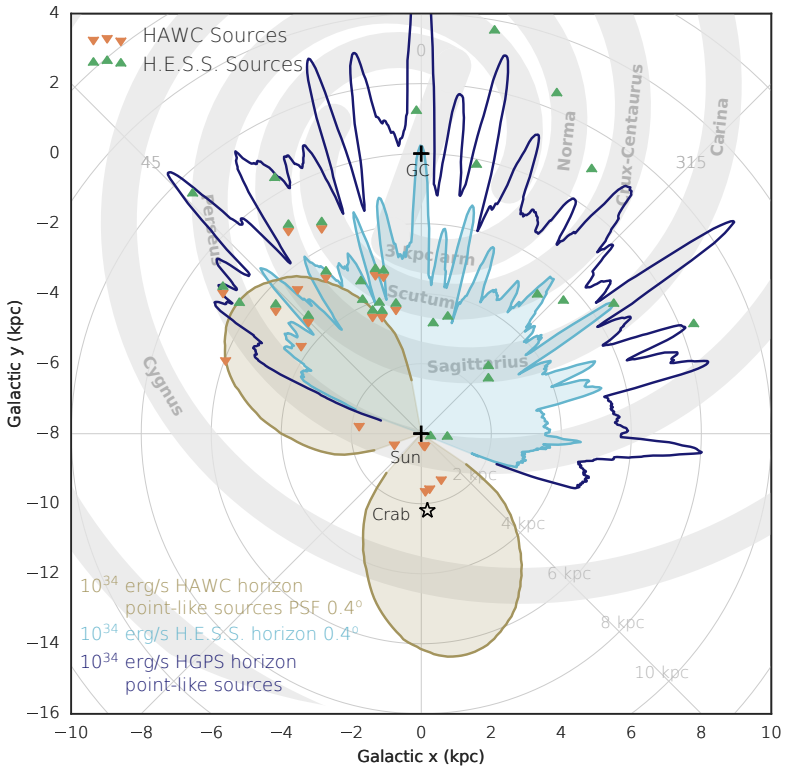

Figure 4.16: Face-on view of the galaxy. The HGPS horizon for a 5σ detection of a point-like source is depicted in dark blue. The H.E.S.S. horizon using ImPACT and a correlation radius of 0.4° is depicted in light blue and the HAWC horizon in light brown. All horizon are performed using the sensitivity curves from Figure 4.15 for source luminosity of 10^{34} erg s^{-1}, for a 5σ detection. The spiral arms of the galaxy [91] are schematically drawn as grey bars. The green and orange triangles represent the sources detected by H.E.S.S. and HAWC respectively for which a distance is known (credit: adapted from the HGPS paper [47] by Axel Donath, MPIK Heidelberg)

4.5 Conclusion

I presented in this chapter a new analysis of the H.E.S.S. galactic plane by using a large correlation radius of 0.4° and applying different method to estimate the background. H.E.S.S. and HAWC maps have been made as comparable as possible in terms of energy range, angular resolution, and by using the same background estimation method: a HAWC map has been made using the H.E.S.S. ring method and a H.E.S.S. map has been produced using the HAWC background estimation method. This study shows the effect of applying the ring background method: it tends to overestimate the background by taking into account extended emission or large scale emission.

Hence, I have been able to present a fair comparison of the galactic plane from both instruments. One main conclusion is that applying the HAWC analysis, favourable to extended sources, on H.E.S.S. data reveals some of the HAWC extended sources in the H.E.S.S. map. So far, only

the part of the H.E.S.S. galactic plane shared with HAWC was presented. It is interesting to look now at the other part of the galactic plane seen only by H.E.S.S.. Figure 4.18 shows the complete H.E.S.S. galactic plane with its original analysis and using the HAWC analysis. A few interesting regions identified by white boxes in this figure show some bright extended emission after the HAWC analysis. They are displayed in Figure 4.19. They show 5 potential candidates for extended sources. Pulsars with $\dot{E} > 10^{35}$ from the ATNF catalogue [69] and SNR from the Green catalogue [46] coincident with significant extended emission are also plotted in these three regions, shown with blue dots and white circles respectively:

- In the first panel, there is significant extended emission above HESS J1646-458. This source is not reported in the published HGPS but this region is known to be a young massive stellar cluster called Westerlund 1 [12]. Next to it, significant emission can be seen close to the SNR G342.0-0.2 and G341.9-0.3. Next to HESS J1702-420, the emission seems to extend toward the pulsar PSR J1702-4310.

- In the second panel, the two sources HESS J1420-607 and HESS J1418-609 are known as the Kookaburra region. Next to it, extended emission is visible coincident to the SNR G312.40-0.4. This SNR was reported to emit γ rays by EGRET [32]. There are also many powerful pulsars in this region coincident with the γ-ray emission.

- In the last panel, there is significant emission in a region of ~2°. Two pulsars are located on the edge.

Each of these regions would definitely deserve a dedicated study to determine if they may be the sources of this extended TeV γ-ray emission.

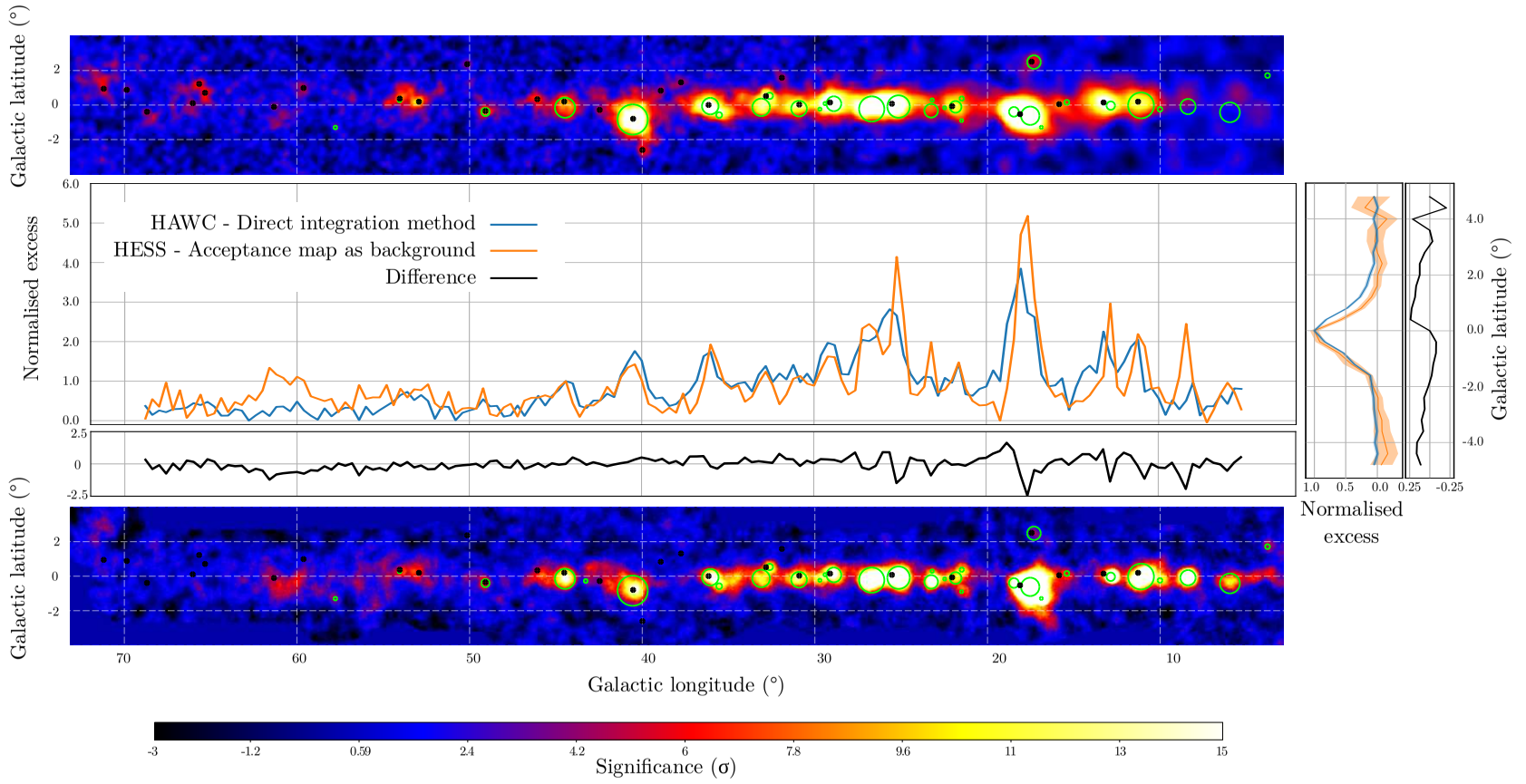

Figure 4.17: Comparison between HAWC and H.E.S.S. galactic planes using an equivalent background estimation: top panel is the HAWC significance map using direct integration method. It corresponds to the blue excess profiles on the middle panel. Bottom panel is the H.E.S.S. significance map using the acceptance maps as background. It corresponds to the orange excess profiles on the middle panel. The longitude profiles (middle panel) are performed for $72° < l < 5°$ and integrated between $-1° < b < +1°$. The latitude profiles (side panel) are performed for $-5° < b < +5°$ and integrated between $72° < l < 5°$. All profiles are using a binning of 0.4° and are corrected for the acceptance. They are normalised to the source W51, a well known SNR at $\ell = 49°$ which is isolated and for which the measured flux by HAWC and H.E.S.S. is very similar. The black curves are the difference between the two profiles.

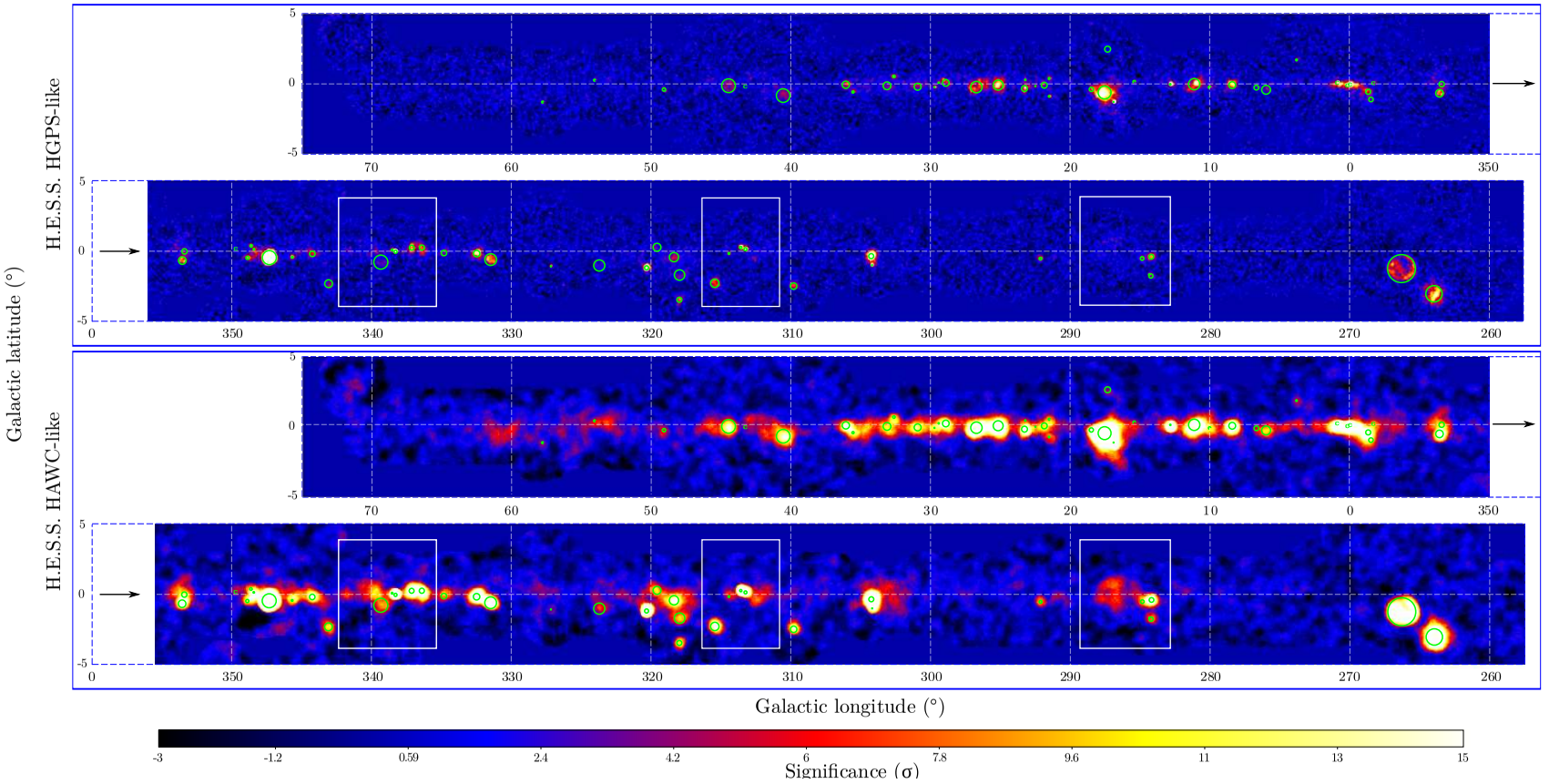

Figure 4.18: Top panel: HGPS for E > 1 TeV, using ImPACT reconstruction and a correlation radius of 0.1° and using the adaptive ring background estimation. Bottom panel: HGPS for E > 1 TeV, using ImPACT reconstruction and a correlation radius of 0.4° and using HAWC direct integration method for the background estimation. The green circles are the 68% containment of the H.E.S.S. sources. The regions in the white boxes show some extended emission highlighted by the HAWC analysis. They are shown in more details in Figure 4.19

Figure 4.19: Zoom on the regions in the white boxes from the map on Figure 4.18. Top panel: HGPS for E > 1 TeV, using ImPACT reconstruction and a correlation radius of 0.1° and using the adaptive ring background estimation. Bottom panel: HGPS for E > 1TeV, using ImPACT reconstruction and a correlation radius of 0.4° and using HAWC direct integration method for the background estimation. The green circles are the 68% containment of the H.E.S.S. sources. The blue dots are pulsars from the ATNF catalogue [69] with $\dot{E} > 10^{35}$ and the white circles are SNRs from the Green catalogue [46].

CHAPTER 5

STUDY OF THE COMPLEX REGION SURROUNDING 2HWC J1928+177

The differences between the galactic plane observed by HAWC and H.E.S.S. have been highlighted in the previous chapter and I reported the sources detected by one instrument and not the other. One complex region is of particular interest at galactic longitude $52° < \ell < 55°$. HAWC detected two sources in the point-like catalogue search [7] with 507 days of data, 2HWC J1930+188 and 2HWC J1928+177. The first one is associated with a known TeV source, the supernova remnant SNR G054.1+00.3. It has been discovered by VERITAS [14], was detected by H.E.S.S. and identified as a composite SNR [47]. However, the source 2HWC J1928+177 discovered by HAWC, coincident with the pulsar PSR J1928+1746, has not been detected by any IACT despite their long exposure on the region. Moreover, there is one more source in this region showing significant γ-ray emission in the most recent HAWC data (1128 days), coincident with the pulsar PSR J1932+1916. In this chapter, I present a multi-component fit of the HAWC data of this region and try to unveil the origin of the VHE γ-ray emission.

5.1 Multiwavelength and multi-experiment observations

HAWC significance map of the region for 1128 days of data, produced under the hypotheses of a point-like source and a spectral index of -2.7, is shown in Figure 5.1. The left map is integrated for nHit bins from 1 to 9 (left map), the middle map is restricted to bins 4 to 9, which is the bin selection used in all this study. The map on the right side of Figure 5.1, for bins 8 and 9 only, shows the highest energy emission. Two sources, 2HWC J1930+188 and 2HWC J1928+177, are reported in the 2HWC catalogue [7]. Only the latest one shows emission above 5σ in the highest energy map. A third one, that would be called HWC J1932+192, shows significant emission but

has not been reported in the catalogue.

2HWC J1930+188 is a known TeV source. It was first detected with 6.8σ significance by VERITAS in 2010 with a total observation time of 36.6 hours [14] and identified as VER J1930+188. It is associated with the γ-ray emission of the SNR G54.1+0.3, located at 6.2 kpc. Studies on the X-ray emission using *XMM-Newton* and *Suzaku* data inferred that the SNR would be ~ 2000 years old [26]. It is not resolved by VERITAS, that has an angular resolution of 0.08° at 1 TeV. With 16 additional hours of observation in 2015-2016, there is now a total of 46 hours of effective observation from VERITAS on this region. Figure 5.2 shows the latest VERITAS excess map of the region with a zoom on each HAWC source [11]. The H.E.S.S. collaboration also reported the detection of this source in the HGPS [47] catalogue. VER J1930+188 and HESS J1930+188 are associated with the PWN surrounding the pulsar at the origin of this SNR, PSR J1930+1852. This pulsar was discovered in 2002 by the Arecibo radio telescope with a period of 136 ms. With a derived spin-down power of $\dot{E}$ = 1.2.10^{37} erg s^{-1} and a characteristic age of ~ 2900 years [31], it is amongst the youngest and most energetic known pulsars. Observations of the X-ray emission by the *Chandra* X-ray observatory during 81 hours reveal the pulsar and the PWN. In addition, infrared observations by the *Spitzer* space telescope and the *Herschel* space observatory show a shell of gas and dust, debris from the supernova explosion, surrounding the PWN. The shell contains IR compact sources arranged in a ring-like structure. They may be young stellar objects whose formation would have been triggered by the wind of the progenitor star [62]. They could also be ejecta dust heated by early type stars belonging to the stellar cluster in which the star exploded [88]. Both *Chandra* X-ray and *Spitzer* IR are visible on the composite image on the left part of Figure 5.2. A morphological association with a molecular cloud detected from CO observations was suggested [64] but no evidence for interaction with this cloud was found [65]. A ^{12}CO map (rotation emission line J=1→0 at 115 GHz) [38] and a radio map from the GaLactic and Extragalactic All-sky MWA (GLEAM) survey [96] are shown in Figure 5.3 where HAWC significance contours have been superimposed. This source will be referred to as J1930 hereafter. The characteristics of this source are summarised in Table 5.2.

2HWC J1928+177 is located about one degree away from 2HWC J1930+188. It has not been detected by an IACT, despite the 46 hours and 36 hours of observations by VERITAS and H.E.S.S. respectively, although excess emission is seen when making the map in a HAWC-like way. However, it is very bright in the HAWC map, with a significance of more than 12σ. Unlike 2HWC J1930+188 and most of the galactic sources detected by HAWC, it shows emission above 7σ significance in the map using the nHit bin 8 and 9 (right map in Figure 5.1) which represent the highest energy. It is likely associated with the pulsar PSR J1928+1746 located 0.03° away, one of the pulsars discovered at radio wavelength in 2006 in a long-term pulsar survey of the galactic plane using the Arecibo L-band Feed Array (ALFA) [37]. It is described as a young isolated pulsar located at a distance of 4.3 kpc. It has a period of 68.7 ms, a spin-

down power of $\dot{E}$ = 1.6.10^{36} erg s^{-1} and a characteristic age of 82 kyr. No detection in X-ray by *Chandra* or NuSTAR has been reported as depicted by the bottom right part of Figure 5.2. The unidentified Fermi source 3FGL J1928+1739 is also located nearby, within 0.1°. However the spectra measured by HAWC and Fermi do not seem to match [68], suggesting that the Fermi spectrum is likely coming from the pulsar emission while the HAWC spectrum would come from a different component. This source will be referred to as J1928 hereafter. The characteristics of this source are summarised in Table 5.1.

HWC J1932+192 is a region of significant emission in the latest data coincident with the pulsar PSR J1932+1916. This pulsar has been discovered by the *Fermi* LAT in 2013 [76] and qualified as radio-quiet. It has a period of 208 ms, a spin-down power $\dot{E}$ = 4.07.10^{35} erg s^{-1} and a characteristic age of 35.4 kyr. It has also been observed in X-ray by *Suzaku* and by the *Swift* X-ray telescope and an extended X-ray emission was reported [60]. The emission was modeled with two gaussians: a narrow one with FWHM ≤0.5' that could be associated with the pulsar, and a broad one with full width at half maximum (FWHM) of ~ 4.5' that could be interpreted as the PWN emission. Using these observations, its distance is estimated between 2 and 6 kpc [60]. This emission is located near the edge of the supernova remnant SNR G54.4-0.3. It is clearly visible on the right map of Figure 5.3 in the shape of a circular feature with the pulsar on the edge. Moreover, a CO structure was reported to be in morphological coincidence with the radio emission, with an evidence for the interaction of the SNR with the surrounding CO shell [59]. For this SNR the distance has been estimated to 6.6 kpc. This source will be referred to as J1932 hereafter. The characteristics of this source are summarised in Table 5.3.

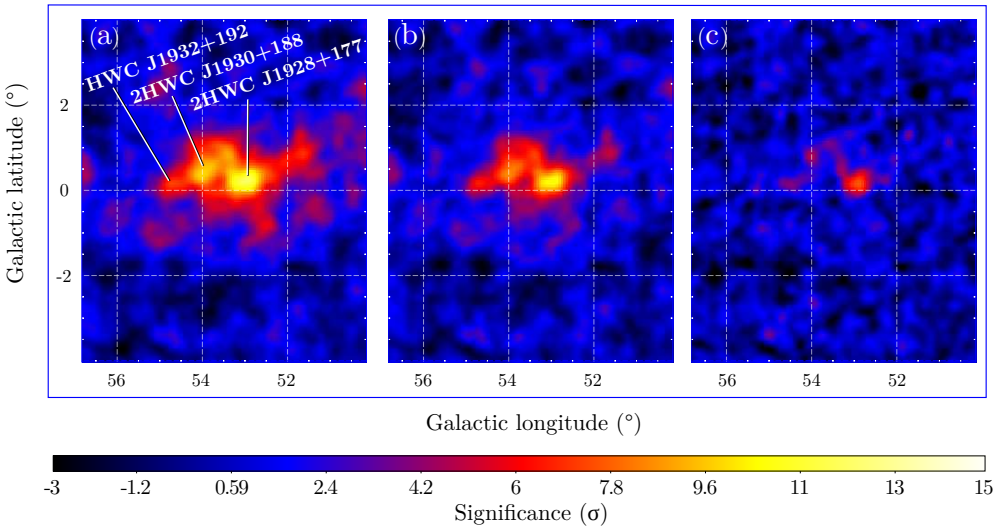

Figure 5.1: HAWC map of the region surrounding 2HWC J1928+177 for different nHit bins: 1 < nHit < 9 (a), 4 < nHit < 9 (b) and 8 < nHit < 9 (c).

	component	observations		parameter	value	comments
J1930	pulsar PSR J1930+1852	radio	Arecibo	period P (ms)	137	
				$\dot{P}$	$7.5.10^{-13}$	
				$\dot{E}$ (erg s^{-1})	12.10^{36}	
				age (kyr)	2.9	
				surf. B field (G)	$1.0.10^{13}$	
		X-ray	*chandra*	size (°)	$7.3.10^{-4}$	pulsar, ring and diffuse elongated PWN
				F (0.3-10 keV)	$2.1.10^{-12}$	
				index	-1.44 ± 0.04	
	PWN G54.1+0.3			size (°)	0.03×0.02	
				F (0.3-10 keV)	$1.18.10^{-12}$	
				index (°)	1.2 ± 0.04	
				distance (kpc)	6.2	
		radio	Effelsberg	size (°)	0.025	
		γ-rays	VERITAS	flux > 1 TeV)	9.10^{-13}	
				index	-2.18 ± 0.2	
			H.E.S.S.	flux > 1 TeV	$5.1.10^{-13}$	
				index	-2.59 ± 0.26	
				size (°)	0.02 ± 0.025	
			HAWC	flux > 1 TeV	$1.8.10^{-12}$	
				index	-2.56 ± 0.14	
	shell SNR G54.1+0.3	radio	VLA	size (°)	0.5×0.43	not associated with the PWN
		IR	GLIMPSE	distance (kpc)	7.3	
		sub-mm	*Herschel*	size (°)	0.05	using an associated CO cloud
		IR	*spitzer*	distance (kpc)	6.2	
				dust mass ($M_\odot$)	0.08-0.9	
		X-ray	*XMM* *Suzaku*	size (°)	0.1	
				age (kyr)	1.8-2.4	

Table 5.1: Characteristics of the components associated with J1930. Fluxes are in erg cm^{-2} s^{-1}

	component	observations		parameter	value	comments
J1928	pulsar PSR J1928+1746	radio	Arecibo	period P (ms)	68.7	
				$\dot{P}$	$1.32.10^{-14}$	
				$\dot{E}$ (erg s^{-1})	$1.6.10^{36}$	
				age (kyr)	82	
				distance (kpc)	4.3	
				surf. B field (G)	$9.6.10^{-11}$	
		γ-ray	*Fermi*	flux (0.1-100 GeV)	$2.2.10^{-11}$	no pulsation
				index, β	-2.6, 0.4	Log parabola
	PWN	γ-ray	EGRET	flux > 100 MeV	157.10^{-8}	(ph cm^{-2} s^{-1})
				index	-2.23	
			HAWC	flux > 1 TeV	$9.3.10^{-13}$	No observation at any other wavelength
				index	-2.56±0.14	
			VERITAS	flux > 1 TeV	< $2.6.10^{-13}$	

Table 5.2: Characteristics of the components associated with J1928. Fluxes are in erg cm^{-2} s^{-1}.

	component	observations		parameter	value	comments
J1932	pulsar PSR J1932+1916	γ-ray	*Fermi*	period P (ms)	208	radio-quiet
				$\dot{E}$ (erg s^{-1})	$4.07.10^{35}$	
				age (kyr)	35.4	
				flux > 100 MeV	$7.8.10^{-11}$	
				cut-off energy (GeV)	1.2	
				index	-1.7±0.1	
				surf. B field (G)	$4.5.10^{-12}$	
		X-ray		distance (kpc)	2-6	based on IS extinction
			Swift	size (°)	< 0.008	from morphological and spectral fit
				flux (0.5-5 keV)	$1.3.10^{-13}$	
				index	-1.4±1.0	
	PWN		*Suzaku*	size (°)	0.075	
				flux (0.5-5 keV)	$1.2.10^{-12}$	
				index	1.8± 0.4	
	shell SNR G54.4-0.3	radio	VLA	distance (kpc)	6.6	association with CO cloud
				size (°)	0.67	
			Arecibo	dynamical age (kyr)	95	2.7 × larger than PSR age

Table 5.3: Characteristics of the components associated with J1932. Fluxes are in erg cm^{-2} s^{-1}

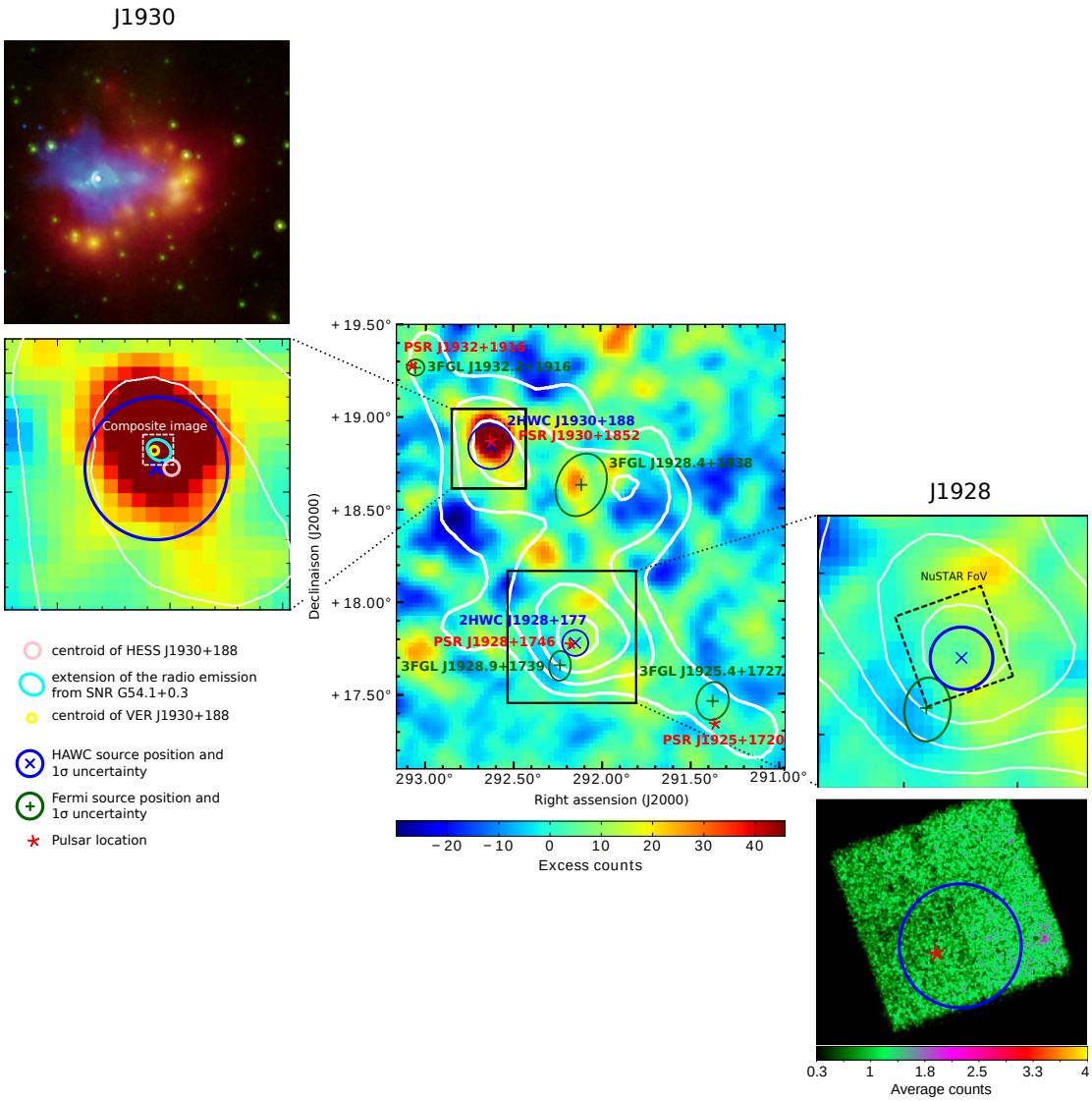

Figure 5.2: Multiwavelength view of the region surrounding 2HWC J1928+177. The middle map is the VERITAS excess map of the region. Superimposed are the location and the 1σ uncertainty on the location for the HAWC sources (blue) and the Fermi 3FGL sources (green) as well as the location of the pulsars (red). The white contours are HAWC significance contours for 5,6, 7 and 8σ from the published map with 507 days [7]. The top source 2HWC J1930+188 is detailed on the zoomed view on the left. The location of the counterpart detected by VERITAS (yellow) and H.E.S.S. (pink) are represented. The extension of the radio emission is also shown (cyan). The dashed white box represents the size of the composite image at the top (3 arcminutes - 0.05°). It depicts the X-ray emission of the pulsar (bright white star) and the PWN detected by *Chandra* (blue) as well as the infrared emission detected by *Spitzer* (green is 8μ and red is 24μ) revealing the dusty remains of a collapsed star. The bottom source 2HWC J1928+177 is detailed on the zoomed image on the right. The dashed black box represents the NuSTAR count map shown at the bottom. (Credit: VERITAS map adapted from [11]; *Chandra* X-ray: NASA/CXC/SAO/T.Temim et al.; *Spitzer* IR: NASA/JPL-Caltech; NuSTAR map: Eugenio Bottacini, INFN Padova).

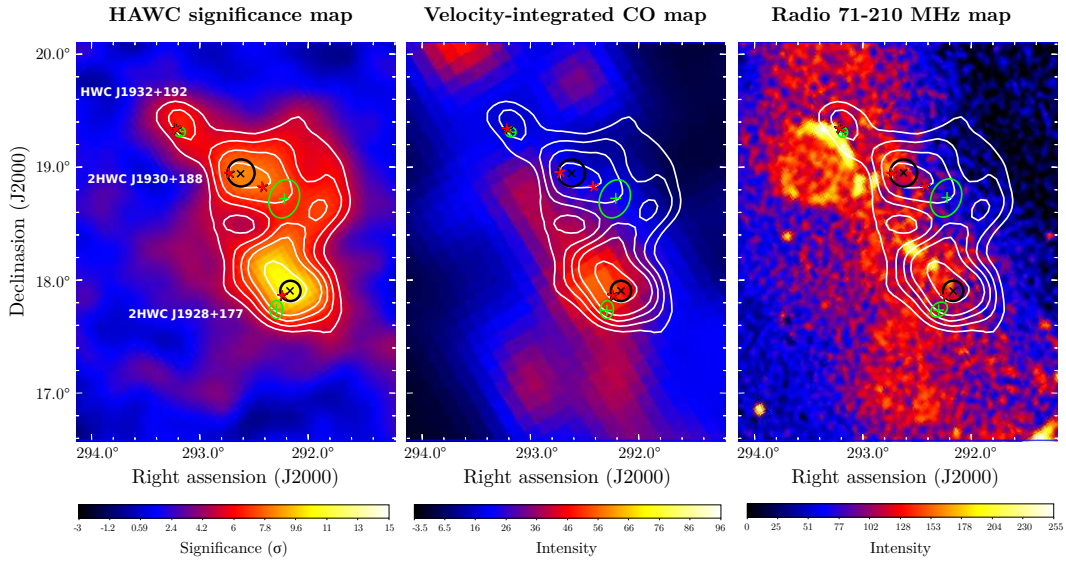

Figure 5.3: The left map is HAWC significance map for 1128 days using nHit bins 4 to 9. The middle map is the velocity integrated CO map and the right map is the 71-210 MHz radio map. Superimposed are the HAWC contours for 5, 6, 7, 8, and 10σ. The location and the 1σ uncertainty of the HAWC sources are represented by the black cross and the black circle. The location and uncertainty of the Fermi 3FGL sources are in green. The red stars represent the pulsars. (Credit: the CO map is from CO survey by [38]. The radio map comes from the GLEAM survey [96].).

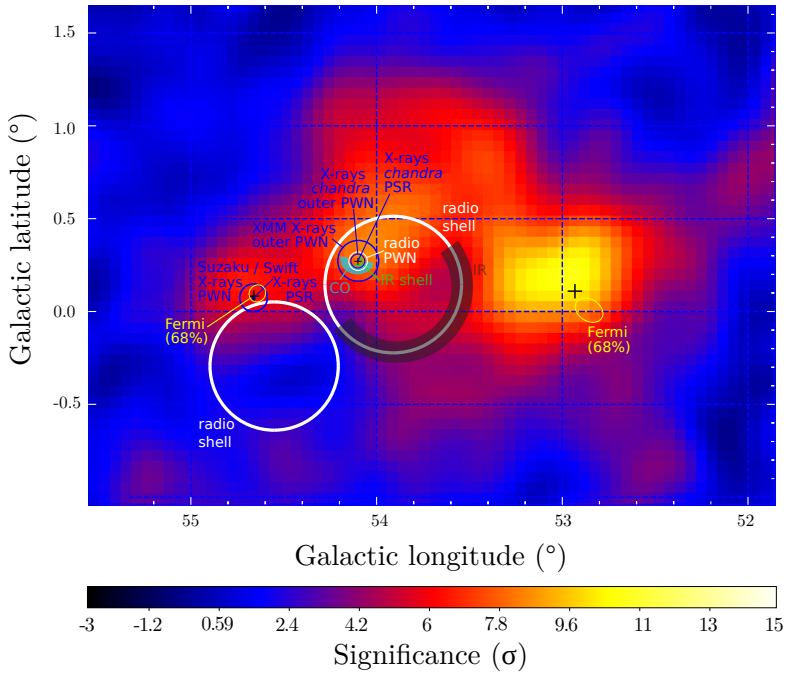

Figure 5.4: Multiwavelength components of the region surrounding 2HWC J1928+177 superimposed on the HAWC significance map for 1128 days using nHit bins 4 to 9.

5.2 H.E.S.S. maps of the region using different background estimation

As discussed in the previous section, H.E.S.S. and VERITAS did not detect the TeV source 2HWC J1928+177. One reason may be that these instruments and their analysis chains are adapted for point-like sources. Hence they can easily miss faint extended sources, especially if they have a hard spectrum. In the previous chapter, I explained how the background estimation plays a crucial role. Figure 5.5 shows the region seen by H.E.S.S. using the different possible background estimations. It shows again that there is no hint for a source at the location of 2HWC J1928+177 in the map with a traditional correlation radius of 0.1°, but as soon as a correlation radius of 0.4° is used, significant emission appears, visible on the maps and on the profiles. Moreover, it is interesting to note that the position of the maximum emission seen in the H.E.S.S. maps for 2HWC J1928+177 is slightly offset by 0.2°.

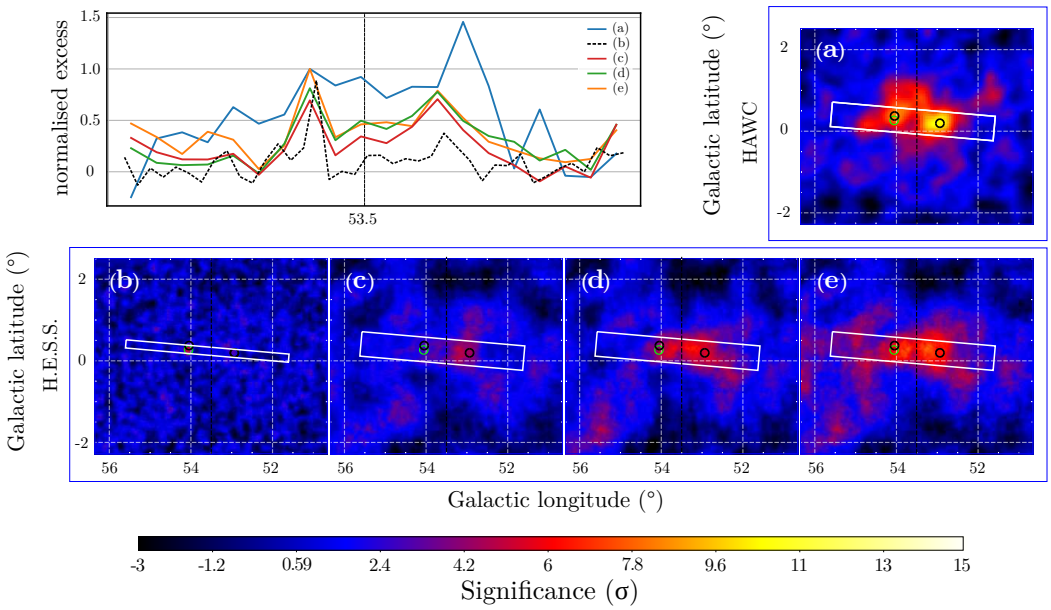

Figure 5.5: HAWC and H.E.S.S. maps of the region at 51° < l < 56° and -2° < b < 2° using different background estimations. The green circle is the 68% containment of HESS J1930+188. The black circles are the location of the HAWC sources 2HWC J1930+188 (left) and 2HWC 1928+178 (right). The white boxes represent the region where the excess profiles are derived, using a binning of 0.05° for map (b) and 0.2° for the others. The profiles are normalised at the location of HESS/HWC J1930+188
(a) - HAWC significance map with 1128 days of data using events falling in nHit bins 4 to 9. The direct integration method is used for the background estimation.
(b) - H.E.S.S. significance map for E > 1 TeV, using ImPACT reconstruction and a correlation radius of 0.1°; here the ring background method is applied on each observation run separately, with an adaptive radius.
(c) - Same H.E.S.S. data and same background estimation method, using a correlation radius of 0.4°.
(d) - Same H.E.S.S. data with the ring applied after the combination of all the observation runs; the size of the ring is fixed to 1.5° inner radius and 0.4° thickness; the correlation radius is 0.4°.
(e) - Same H.E.S.S. data. The acceptance map is used as background. It is comparable to the HAWC map (a).

5.3 Modelling of the region and fit of the HAWC data

Modelling this region is not trivial because it requires to disentangle the different sources. I describe hereafter an attempt to represent this complex region with several components for which the parameters are fitted all together using the Multi-Mission Maximum Likelihood framework (3ML) [93]. It is based on a maximum likelihood approach, in which a model representing a particular region of the sky, here made of several components, is convolved with the instrument response and compared to the corresponding experimental data.

First step: initial model A

I define an initial model for the region based on our current knowledge:

1. VERITAS and H.E.S.S. detected the PWN of the pulsar PSR J1930+1852 as a point source. Hence I define the source 2HWC J1930+188 as a point source initialised at the location of the pulsar. This component will be simply called J1930.

2. A significant hint of TeV emission is coincident with the pulsar PSR J1932+1916, 0.6° away from PSR J1930+1852. Regarding the extension of the emission in HAWC, it seems compatible with a point source. Thus, I add a point source initialised at the location of the pulsar. Later, I will also check if an extended source would be a better representation for this source. This component will be simply called J1932.

3. The source 2HWC J1928+177 has not been detected by any IACT, favouring the hypothesis that this sources is extended. From H.E.S.S. upper limits the size of the source may be of the order of 0.4° [68]. Moreover, the study in the previous chapter showed that this source appears in the H.E.S.S. map when using a correlation radius of 0.4°. Hence, it is represented by an extended component with the shape of a symmetric gaussian with initial location the position of the pulsar PSR J1928+1746 and with an initial size of σ = 0.4°. This component will be simply called J1928.

These are the three components of the initial model. All of them have free position and size. To keep the model simple, the spectra of all components are assumed to follow a single power law with free index initialised at -2.5, and free differential flux at 10 TeV with an initial value of 1.10^{-14} TeV^{-1} cm^{-2} s^{-1}.

Figure 5.6(a) shows the significance map of the region for a point like source hypotheses and for a power law spectrum with an index of -2.7, which are the standard parameters used to produce HAWC maps. The blue dots and circle represent the initial position of the three components and the green dots and circles show their best position after the fit. The width of the green circle represent the 1σ uncertainty on the size of the gaussian. The final results of the fit are summarised in the first part of Table 5.4. J1928 is represented by a very extended

source of size σ = 0.69°, likely representing some larger scale emission. A map of the model is shown in 5.6(b). The residual map and its significance distribution are also shown in (c). The orange line is a fit to the distribution with a gaussian function. The results of the fit are given on the plot. The distribution for pure background should be centred at a mean value $\mu = 0$ with $\sigma = 1$. An excess of 4σ significance is visible at the location of J1928, as well as on the significance distribution. Panel (d) displays the spectrum for the best fit model and it lies systematically below the data. It means that this model does not represent the data very well, probably due to the fact that J1928 is not well represented by this very big extended source, as shown by the excess at its location in the residual map. Panel (e) shows the energy spectra of all the components for the energy range 3.5 - 51 TeV, corresponding to the median energies of bin 4 and 9.

Second step: model B

To account for the significant remaining excess at the location of J1928, I add to the model an extended source initialised at the maximum significance of this excess and with initial size σ = 0.1°. This is the new component for J1928. The other extended source (source 1) is given as initial position and size the output from the previous fit. Position, size, index and flux normalisation are the free parameters. A fit is performed again with the four components. The output of the fit are summarised in the second part of Table 5.4 and the corresponding maps and plots are displayed in Figure 5.7. The component representing J1928 is now found to have a size of σ = 0.13°, while the other extended source is even bigger than before with σ = 0.91°. Panel (d) shows that this model fits better the data. An excess of 2.5σ significance remains at the top of the region of interest, visible on the map (c) of Figure 5.7. The TS value when comparing this model with the previous one is 34.

Third step: model C

I add a last extended source (source 2), initialised at the maximum significance of the remaining excess with initial size 0.1°, with free index and flux normalisation. The other extended components are given as initial position and size the output of the previous fit. The five components are fitted together and the output is summarised in the third part of Table 5.4. The corresponding maps and plots are displayed in Figure 5.8. Source 2 seems well represented with an extended source of size σ = 0.3°, while J1928 is now represented by a source slightly bigger of size σ = 0.17° and the very big extended source previously of size σ = 0.91° (source 1) is now even bigger with a size of σ = 1.3°, shifted towards the bottom of the region. It probably tries to account for some large scale diffuse emission. Indeed, the region of interest is located in the galactic plane, and it is known that there is a γ-ray diffuse emission component, for example from Fermi [3] or H.E.S.S. analysis [13] [47]. Moreover, the significance maps in Figures 5.6(a), 5.7(a) and 5.8(a) show almost no negative excess in the region of interest, while it would be expected to have positive as well as

negative fluctuations. The residual maps in Figure 5.8 (c) does not show any significant excess anymore and is nicely distributed around 0 as shown by the distribution of the residuals on the same figure, although $\sigma < 1$. The TS value when comparing this model with the previous one is 20.

Discussion of the results

Table 5.4 gathers the results of each step. For all of them, the parameters obtained for the two point sources J1930 and J1932 are consistent. Note that having a point source representing J1932 improves significantly the fit with respect to having no component for this source: the TS value is 26 between a model that represents J1932 by a point source and a model that has no component for J1932. Moreover, if J1932 is represented by an extended source, the fitted size is $\sigma = 0.08°$ and the fit is not improved compared to the point source hypotheses. Hence J1932 seems to be well represented by a point source and helps in the representation of the whole region.

The TS value between the models with 4 and 5 components is 20. It may not be significant when considering the addition of an extended source. However, if I remove the very extended source of 1.3° (source 1) from the last model and perform a fit again with J1928 and source 2 only, it has now the same number of components as model B. The TS value between them is 20 in favour of model B. Hence, in model C, source 1 seems to play a role.

The results of the fit for the component representing J1928 is very similar in the 2 models B and C with either 4 or 5 components: the position, the size and the spectral parameters are consistent within the error bars. I will use the results of the last fit with 5 components for the study of J1928 in the next sections. However, using the output of one or the other would not change the conclusions.

This analysis has been made under the assumption that the extended sources are well represented by a symmetric gaussian. Of course, it may not be the case and an improvement would be to test asymmetric gaussians. Moreover, the spectrum was assumed to follow a single power law. It would be interesting to test if a power law with an exponential cutoff spectrum would improve the fit. However, it has been reported [11] that for the case of J1930, the HAWC data could be explained with either a single power law or a power law with an exponential cutoff.

Model A	J1930	J1932	J1928
hypothesis	point-like	point-like	extended
pos_i	PSR J1930	PSR J1932	PSR J1928
pos_f (ra °)	292.52 $\pm$ 0.08	293.09 $\pm$ 0.06	292.17 $\pm$ 0.07
(dec °)	18.94 $\pm$ 0.12	19.40 $\pm$ 0.06	18.19 $\pm$ 0.08
$size_i$ (°)	-	-	0.40
$size_f$ (°)	-	-	0.69 $\pm$ 0.06
$index_i$	-2.5	-2.5	-2.5
$index_f$	-2.99 $\pm$ 0.34	-2.73 $\pm$ 0.25	-2.49 $\pm$ 0.07
$flux_i$	10.0	10.0	10.0
$flux_f$	$1.7^{+0.7}_{-0.5}$	$2.2^{+0.6}_{-0.5}$	$24.4^{+3.1}_{-2.7}$

Model B	J1930	J1932	J1928	source 1
hypothesis	point-like	point-like	extended	extended
pos_i	PSR J1930	PSR J1932	(292.07,17.78)	(292.17,18.19)
pos_f (ra °)	292.48 $\pm$ 0.013	293.06 $\pm$ 0.07	292.14 $\pm$ 0.04	292.26 $\pm$ 0.13
(dec °)	18.88 $\pm$ 0.06	19.37 $\pm$ 0.018	17.85 $\pm$ 0.05	18.37 $\pm$ 0.12
$size_i$ (°)	-	-	0.10	0.69
$size_f$ (°)	-	-	0.13 $\pm$ 0.04	0.91 $\pm$ 0.12
$index_i$	-2.5	-2.5	-2.5	-2.5
$index_f$	-2.89 $\pm$ 0.3	-2.61 $\pm$ 0.3	-2.16 $\pm$ 0.25	-2.59 $\pm$ 0.1
$flux_i$	10.0	10.0.	10.0	10.0
$flux_f$	$1.9^{+0.7}_{-0.5}$	$1.7^{+0.7}_{-0.5}$	$2.8^{+1.6}_{-1.0}$	$25.8^{+4.0}_{-3.5}$

Model C	J1930	J1932	J1928	source 1	source 2
hypothesis	point-like	point-like	extended	extended	extended
pos_i	PSR J1930	PSR J1932	(292.14,17.85)	(292.26, 18.37)	(291.75, 18.53)
pos_f (ra °)	292.54 $\pm$ 0.07	293.05 $\pm$ 0.06	292.14 $\pm$ 0.04	292.29 $\pm$ 0.5	291.86 $\pm$ 0.1
(dec °)	18.88 $\pm$ 0.021	19.37 $\pm$ 0.06	17.86 $\pm$ 0.04	18.01 $\pm$ 0.34	18.82 $\pm$ 0.09
$size_i$ (°)	-	-	0.13	0.91	0.1
$size_f$ (°)	-	-	0.17 $\pm$ 0.04	1.3 $\pm$ 0.4	0.3 $\pm$ 0.07
$index_i$	-2.5	-2.5	-2.5	-2.5	-2.5
$index_f$	-2.89 $\pm$ 0.27	-2.56 $\pm$ 0.29	-2.24 $\pm$ 0.17	-2.79 $\pm$ 0.15	-2.21 $\pm$ 0.23
$flux_i$	10.0	10.0	10.0	10.0	10.0
$flux_f$	$2.1^{+0.6}_{-0.5}$	$1.9^{+0.7}_{-0.5}$	$4.4^{+1.6}_{-1.2}$	$26^{+1.2}_{-0.8}$	$4.1^{+1.2}_{-0.8}$

Table 5.4: Input values and fitted values for each component of the models representing the region surrounding 2HWC J1928+177. The fit is done in three steps. The basic model has three components representing J1928, J1930 and J1932 (first table). After each step an extended source is added at the location of significant excess in the residual map (second and third tables) until there is no significant excess anymore. For each parameter, the subscripts i and f stand for *initial* and *final* respectively. The normalisation flux is given at 10 TeV in units of 10^{-15} TeV^{-1} cm^{-2} s^{-1}. The position of the pulsars PSR J1930+1852, PSR J1932+1916 and PSR J1928+1746 are (202.18,17.77), (292.62,18.88) and (293.08,19.27) respectively.

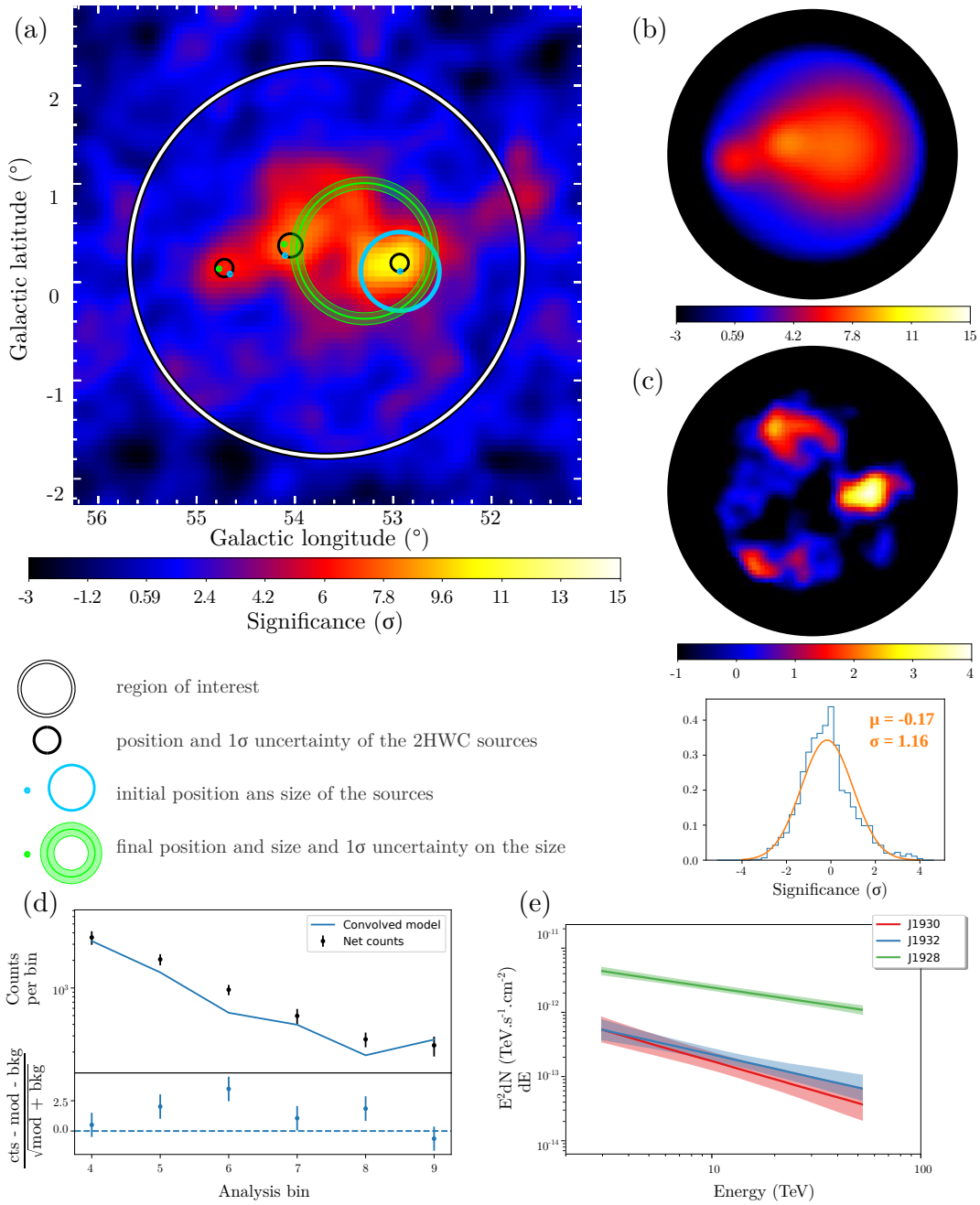

Figure 5.6: Initial model A. The significance map (a) shows the region of interest and the three components for J1928, J1930 and J1932. Blue dots and circle show their initial position and size. The green dots and circles show the fitted results. The width of the green circle represent the 1σ uncertainty on the size of the gaussian. Map (b) shows the model. Map (c) is the residual map and its significance distribution with a gaussian fit. Panel (d) shows the data and best fit model spectrum and the residuals. Panel (e) shows the energy spectra of all the components of the model.

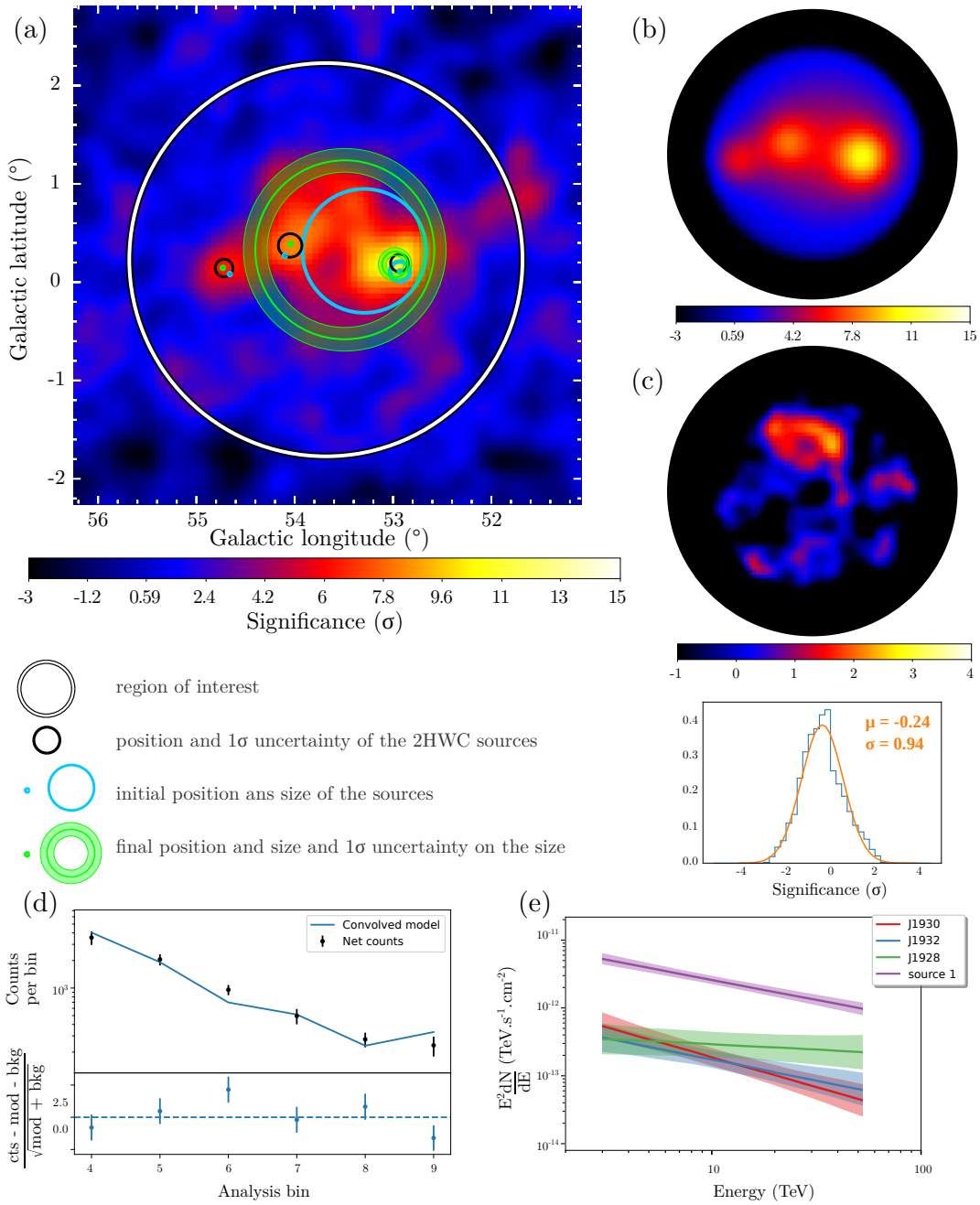

Figure 5.7: Model B. The significance map (a) shows the region of interest and the three components for J1928, J1930 and J1932 plus one extended source to account for the excess in the residual of the previous fit. Blue dots and circles show their initial position and size. The green dots and circles show the fitted results. The width of the green circle represent the 1σ uncertainty on the size of the gaussian. Map (b) shows the model. Map (c) is the residual map and its significance distribution with a gaussian fit. Panel (d) shows the data and best fit model spectrum and the residuals. Panel (e) shows the energy spectra of all the components of the model.

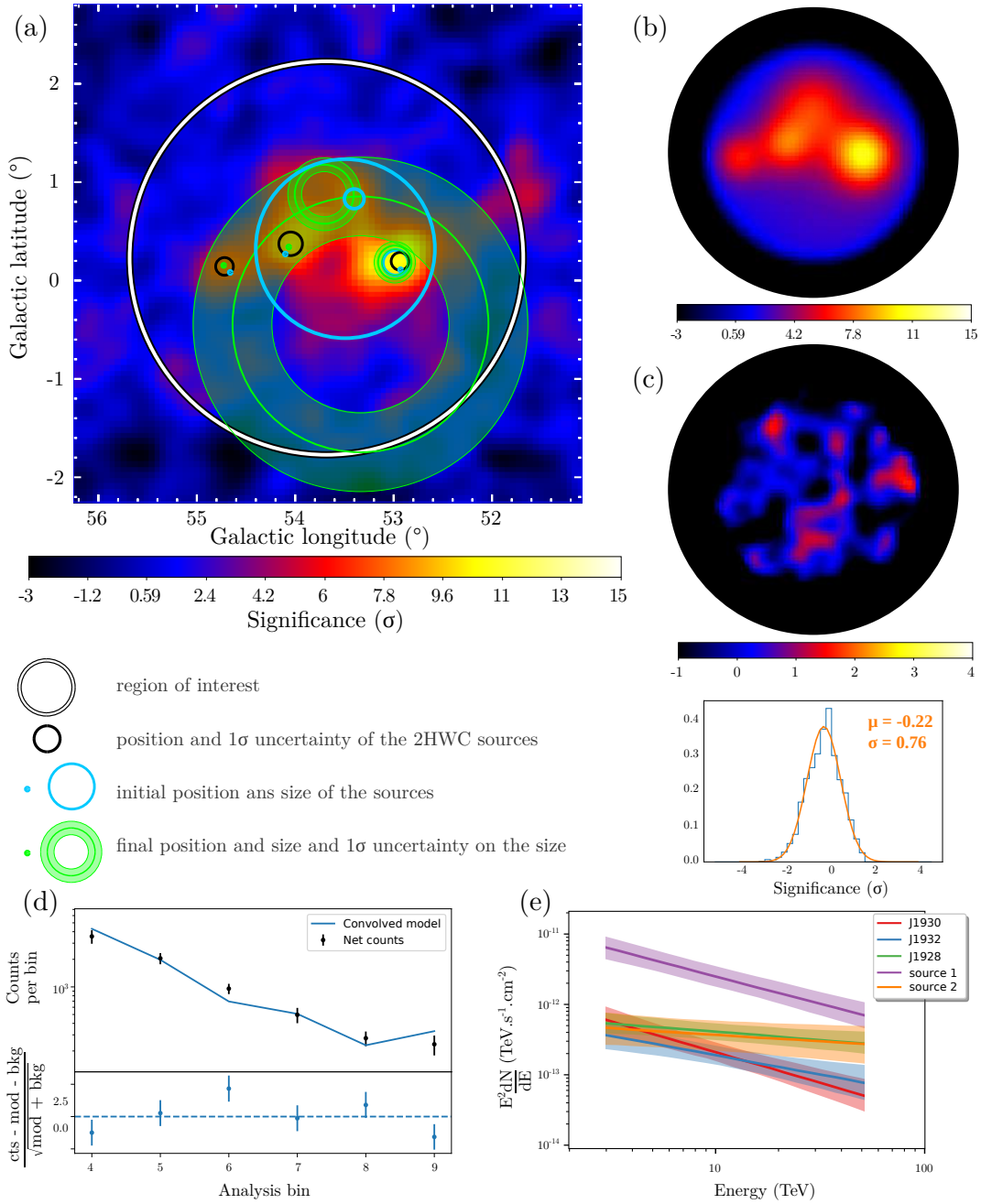

Figure 5.8: Model C. The significance map (a) shows the region of interest and the three components for J1928, J1930 and J1932 plus two extended sources to account for the excesses in the residual of the previous fits. Blue dots and circles show their initial position and size. The green dots and circles show the fitted results. The width of the green circle represent the 1σ uncertainty on the size of the gaussian. Map (b) shows the model. Map (c) is the residual map and its significance distribution with a gaussian fit. Panel (d) shows the data and best fit model spectrum and the residuals. Panel (e) shows the energy spectra of all the components of the model.

5.4 Energy spectrum of 2HWC J1930+188

The spectrum of the source J1930 resulting from the fit of the last model described in the previous section can be compared with published results. From the published HAWC catalogue [7], using 507 days of data and energy bins 1 to 9, and for a point-like source hypothesis, the spectrum was described by a single power law, with a normalisation flux at 7 TeV of $(9.8 \pm 1.5).10^{-15}$ TeV^{-1} cm^{-2} s^{-1} and an index of -2.74 ± 0.12. Hence the flux at 10 TeV is $3.7.10^{-15}$ TeV^{-1} cm^{-2} s^{-1}, slightly higher that the value found for this component in the fit of $2.1.10^{-15}$ TeV^{-1} cm^{-2} s^{-1}. This is illustrated by the red and green spectra in Figure 5.9.

In a paper written between the HAWC, VERITAS and *Fermi* collaborations [11], it has been compared with VERITAS data at lower energies. Figure 5.9 also shows the VERITAS spectrum (black), together with the spectrum derived for the HAWC catalogue (red) and the spectrum coming out of the fit using 3ML (green). The energy range for the later spectrum has been chosen considering the median energies of bin 4 and bin 9, 3.5 TeV and 51 TeV respectively [7]. This new spectrum is in better agreement with VERITAS spectrum. This may be explained by the fact that the model proposed here decompose the emission at the location of J1928 into two components, a small source (J1928) and a very large one (source 2), while the catalogue consider only one source. Hence the component for J1928 proposed here has a slightly lower flux.

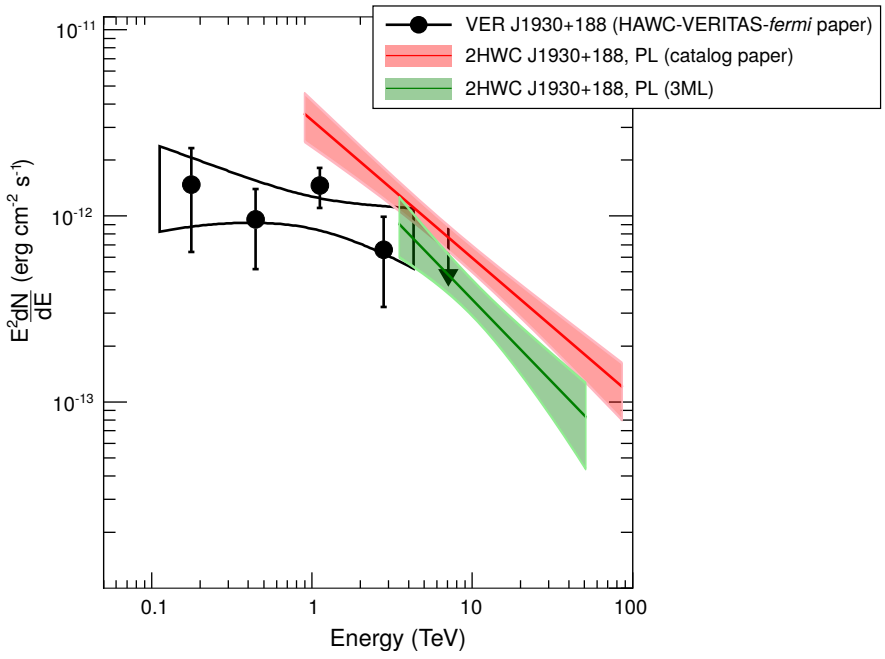

Figure 5.9: Energy spectrum of 2HWC J1930+188. The black dots are derived by VERITAS which found this source to be point-like [11]. The red spectrum uses parameters from the HAWC catalogue [7] assuming only one point source. The green spectrum is resulting from the fit of the model assuming two point sources and three extended sources as a good representation for the region.

5.5 Energy spectrum of the new source HWC J1932+192

In this section, I present briefly the new TeV γ-ray source candidate J1932, potentially associated with the pulsar PSR J1932+1916, and discuss if the observed emission could come from the acceleration of particles in its PWN. All characteristics of this system were gathered earlier in section 5.1, Table 5.3. The spectrum derived with 3ML under the point-like hypotheses is plotted in Figure 5.10. Similarly to J1930, the energy range for this spectrum has been chosen considering the median energies of bin 4 and bin 9, 3.5 TeV and 51 TeV. H.E.S.S. did not detect this source, but provides upper limits at a confidence level of a 99%, assuming a point-like source and a power law with an index of -2.6. The spectrum seems consistent with these upper limits for E > 3 TeV as shown in the figure.

Table 5.5 gathers the parameters calculated hereafter. From the best fit, the differential flux at 10 TeV was found to be $1.9.10^{-15}$ TeV^{-1} cm^{-2} s^{-1}. With a spectral index equal to -2.56, the integrated energy flux above 1 TeV $F_{\gamma>1\mathrm{TeV}}$ is given by

$$\int_{E_1}^{\infty} E\,\Phi_0\left(\frac{E}{E_0}\right)^{-\Gamma} dE \longrightarrow \Phi_0 E_0^2 \frac{1}{\Gamma-2}\left(\frac{E_1}{E_0}\right)^{-\Gamma+2} \tag{5.1}$$

with $E_1 = 1$ TeV $= 1.6$ erg and $\Gamma < -2$. It gives $F_{\gamma>1\mathrm{TeV}} = 2.10^{-12}$ erg cm^{-2} s^{-1}.
The γ-ray luminosity is given by:

$$L_\gamma = 4\pi D^2 F_{\gamma>1\mathrm{TeV}} \tag{5.2}$$

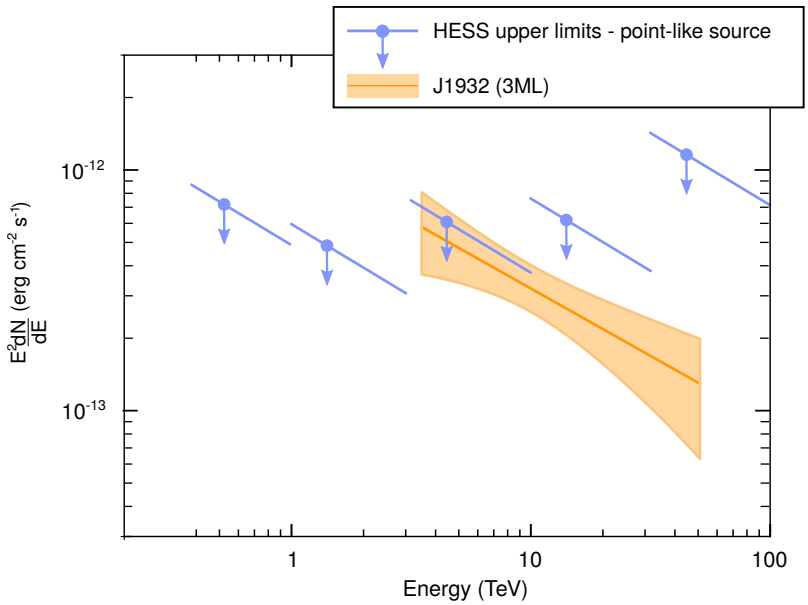

Figure 5.10: Energy spectrum of the new source HWC J1932+192 resulting from the fit of the component for this source, assuming a point-like source. The upper limits derived by H.E.S.S. for a point-like source in different energy bands are shown in blue (credit: H.E.S.S. upper limits: Vincent Marandon, MPIK Heidelberg).

No distance has been reported for this pulsar. However, if it is associated with the SRN G54.4-0.3, the distance would be 3 - 4 kpc. Under this assumption, $L_\gamma \sim 3.10^{33}$ erg s^{-1}. The associated pulsar has a spin-down power of $\dot{E} = 4.10^{35}$ erg s^{-1}. It means that a bit less than 1% of the pulsar energy is needed to accelerate particles producing this γ-ray emission.

	J1932
morphology hypotheses	point-like
distance D (pc)	3500
integrated energy flux $F_{\gamma>1TeV}$ (erg cm^{-2} s^{-1})	2.10^{-12}
γ-ray luminosity L_γ (erg s^{-1})	3.10^{33}

Table 5.5: Summary of the properties of the new source J1932 in the hypotheses where IC scattering is the dominant radiation process.

5.6 Morphology and energy spectrum of 2HWC J1928+177

In this section, I focus on the source J1928. The best fit of the data gives a source of size σ = 0.17°. Note that for a 2D gaussian shape like it is the case here, 1σ represents 39% containment. The 68% containment would give a size of 0.26°. With a flux of $4.4.10^{-15}$ TeV^{-1} cm^{-2} s^{-1} at 10 TeV and a spectral index of -2.24, as reported in Table 5.4, it corresponds to an integrated flux above 1 TeV of $6.2.10^{-13}$ cm^{-2} s^{-1}, which is $\sim$ 3% crab. The sensitivity of H.E.S.S. at the location of 2HWC J1928+177 for a 0.2° integration region is 2% crab. Hence it seems at the limit of being detectable by H.E.S.S.

In order to estimate the relevant energy range for the fit, I fitted a simple power law multiplied with a step function: $f(x) = 1$ for $E_{low} < x < E_{up}$, and $f(x) = 0$ otherwise. The lower and upper bounds E_{low} and E_{up} are the free parameters of the fit. The output of the fit gives an energy range of 11 TeV < E < 94 TeV. For comparison, in the ICRC proceeding [68], similarly to the HAWC catalogue paper [7], the central 75% of energies contributing to the TS of the source is used to define a valid energy range of 1 TeV < E < 86 TeV.

I first compare it with the spectrum published in the ICRC proceeding in 2017 [68] using 760 days of data and the energy bins 4 to 9. The source was assumed point-like and the spectrum was described by a single power law, with a normalisation flux at 7 TeV of $(1.07 \pm 0.12).10^{14}$ TeV^{-1} cm^{-2} s^{-1} and an index of -2.60 $\pm$ 0.09. This is the red curve in Figure 5.11. The green curve represents the spectrum fitted for the model and shows higher flux at 10 TeV. That is expected since it assumes an extended source of 0.17°, it consequently integrates more flux than a point source. The spectral index for the model (-2.24 $\pm$ 0.17) is lower than the one in the published proceeding (-2.60 $\pm$ 0.09) but is within the 2σ error.

Then, I compare it with upper limits derived by H.E.S.S., which did not detect this source. This is illustrated in Figure 5.12. On this Figure are plotted the H.E.S.S. upper limits at a confidence level of a 99%, assuming a gaussian of size σ = 0.17° and a power law with an index of -2.56. We can see that the spectrum derived here for J1928 is compatible with the H.E.S.S. upper limits. Note that these limits are very conservative: the component associated with J1928 sits on another very extended source, and the H.E.S.S. upper limit does not make the difference: it integrates all the signal in a region of σ = 0.17°.

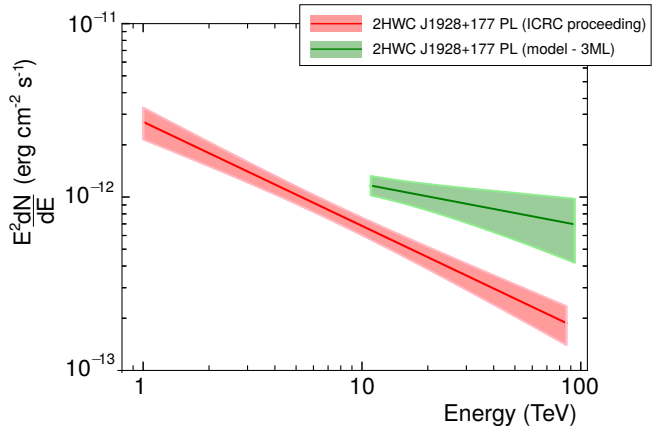

Figure 5.11: Energy spectrum of 2HWC J1928+177. The red spectrum was obtained with 760 days of data using the energy bin 4 to 9 and assuming a point-like source [68]. The green spectrum results from the fit of the model assuming an extended source with a gaussian shape.

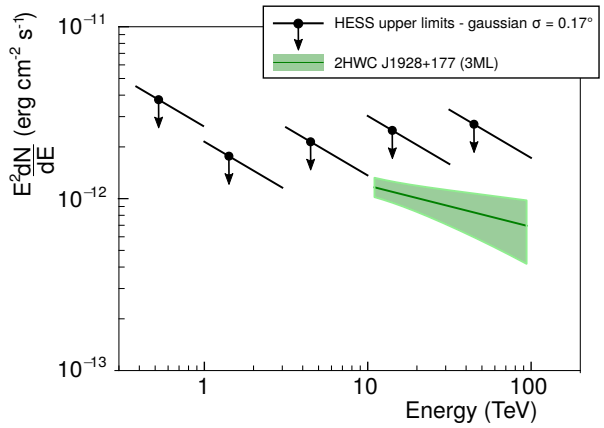

Figure 5.12: Energy spectrum of 2HWC J1928+177 and H.E.S.S. upper limits at a confidence level of 99%: The plot displays the spectrum of 2HWC J1928+177 fitted with 3ML (green) where the extended source was found to have a size of σ = 0.17°. The upper limits derived by H.E.S.S. for a gaussian of σ = 0.17° in different energy bands are shown in black (credit: H.E.S.S. upper limits: Vincent Marandon, MPIK Heidelberg).

5.7 Origin of the γ-ray emission of J1928

Two scenarios could explain the observed TeV γ-ray emission of 2HWC J1928+177: one is that the electrons accelerated in the PWN associated with the pulsar PSR J1928+1746 produce γ rays via inverse Compton scattering on ambient photons. The other is that the interaction of cosmic ray protons and electrons with a molecular cloud would produce γ rays from neutral pion decay or bremsstrahlung respectively.

5.7.1 Inverse Compton scattering of the electrons from the PWN

Gamma-ray emission

From the best fit of the region obtained in the previous section, the component for J1928 was found to be a gaussian of angular size $\sigma = 0.17°$. All the properties derived hereafter are summarised in Table 5.6. The diameter d and volume V assuming a spherical geometry can be calculated using

$$d \simeq 2\sigma D \qquad \text{and} \qquad V = \frac{4}{3}\pi\left(\frac{d}{2}\right)^3 \tag{5.3}$$

The pulsar being located at a distance of $D = 4.3$ kpc, 39% and 68% of the emission is contained in a region of size $d \simeq 25$ pc and 38 pc respectively. Moreover, from the best fit, the differential flux at 10 TeV was found to be $4.4.10^{-15}$ TeV^{-1} cm^{-2} s^{-1} with a spectral index equal to -2.24. Under the assumption that this is valid at E < 10 TeV, the integrated energy flux above 1 TeV is then $F_{\gamma>1\text{TeV}} = 4.5.10^{-12}$ erg cm^{-2} s^{-1} .
The γ-ray luminosity is given by equation 5.2. In the case of our fitted component for J1928 $L_\gamma = 1.0.10^{34}$ erg s^{-1}.

The emission observed in PWN at TeV energies is dominated by radiation processes involving electrons scattering on ambient photons: Inverse Compton scattering (IC). In the Thomson regime, the γ-ray spectral energy distribution of electrons with energy E_e peaks at:

$$E_\gamma \simeq 33 E_e^2 k_B T \quad \text{TeV} \tag{5.4}$$

with E_γ and E_e in TeV, k_B the Boltzmann constant, T the temperature of the photon field and $k_B T$ in eV [52]. The relation between the energy of the electrons and the γ rays produced via IC scattering is:

$$E_e \simeq 11\sqrt{E_\gamma} \quad \text{TeV} \tag{5.5}$$

Hence, a 1 TeV γ-ray photon is produced by an electron of energy ~ 10 TeV. The electron cooling time for IC scattering in the Thomson regime is given by:

$$\tau_{\text{IC}} = \frac{E_e}{dE_e/dt} \simeq 3.1.10^5 \frac{1}{U_{\text{rad}}} \frac{1}{E_e} \quad \text{yr} \tag{5.6}$$

with E_e in TeV and U_{rad} the radiation energy density in eV cm^{-3} [52]. For electrons of energy E_e = 10 TeV scattering on photons from the Cosmic Microwave Background (CMB),

$k_B T = 2.35.10^{-4}$ eV and $U_{\rm rad} = 0.26$ eV cm^{-3}, so the electron cooling time is $\tau_{\rm IC} \simeq 120$ kyr. For Far Infrared photons (FIR), $k_B T = 3.10^{-4}$ eV and $U_{\rm rad} = 0.3$ eV cm^{-3}, so $\tau_{\rm FIR} \simeq 100$ kyr.
The total energy given by:

$$W = \tau \, L_\gamma \tag{5.7}$$

is then equal to $W_{\rm IC} \simeq 3.8.10^{46}$ erg, using $\tau_{\rm IC}$ from equation 5.6.
Finally, dividing by the volume, the energy density is simply:

$$\epsilon_{\rm W} = \frac{W}{V} \tag{5.8}$$

Assuming a spherical geometry, the energy density is then $\epsilon_{\rm IC} \simeq 0.03$ eV cm^{-3}. This is slightly smaller than the energy density of the ISM $\epsilon_{\rm ISM} \simeq 1$ eV cm^{-3}, but given the age of the pulsar, it is consistent with an old PWN where the electrons started to cool and diffuse away from their source. Table 5.6 summarises all the parameters.

	J1928
angular size θ (°)	0.17 (39%) 0.26 (68%)
distance D (pc)	4300
size (68%) d (pc)	38
volume V (pc^3)	3.10^4
γ-ray luminosity L_γ (erg s^{-1})	$1.0.10^{34}$
total energy $W_{\rm IC}$ (erg)	$3.8.10^{46}$
energy density $\epsilon_{\rm IC}$ (eV cm^{-3})	0.03

Table 5.6: Summary of the properties of the fitted source J1928 in the hypotheses where IC scattering is the dominant radiation process.

Parent particle population

The parent population of electrons responsible for the observed γ-ray emission can be obtained using the *naima*[1] python package [101]. It provides models for non thermal radiative emission from homogeneous distributions of relativistic particles. The contributions of non thermal radiative processes, IC scattering in this case, can be computed given a shape for the particle energy distribution, and the model can be used to fit observed non thermal spectra through

[1]The documentation and code for naima is available at: https://naima.readthedocs.io/en/latest and https://github.com/zblz/naima

a Markov chain Monte Carlo procedure. In the present case, the emission is assumed to be produced by electrons upscattering CMB photons, with temperature T = 2.72 K and energy density of 0.261 eV cm^{-3}, and FIR photons, with temperature T = 20 K and energy density of 0.3 eV cm^{-3}. Since the γ-ray spectrum of J1928 has been represented by a power law, the population of electrons is also chosen to follow a single power law. The fit is performed using this model for the electrons, the γ-ray spectrum from HAWC observation from the best fit with 3ML, and H.E.S.S. upper limits for a gaussian source of size σ = 0.17°. The best fit for the energy distribution of electrons is displayed in Figure 5.13(a), with the differential energy distribution at 1 TeV $F_{1\mathrm{TeV}} = (6.1^{+3}_{-2}).10^{46}$ erg and an index of -2.67 ± 0.1. This population of electrons would produce the γ-ray spectrum plotted in red in Figure 5.13(b).

The total energy in electrons above 1 TeV is $W_e = 9.10^{46}$ erg. The spin-down of the pulsar being $\dot{E} = 1.6.10^{36}$ erg s^{-1}, assuming that it is constant over the life of the pulsar which is 82 kyr old gives a lower limit for the total energy released by the pulsar of $4.1.10^{48}$ erg. Hence an upper limit of ~ 2% can be set on the amount of energy that the pulsar could have transferred to electrons above 10 TeV.

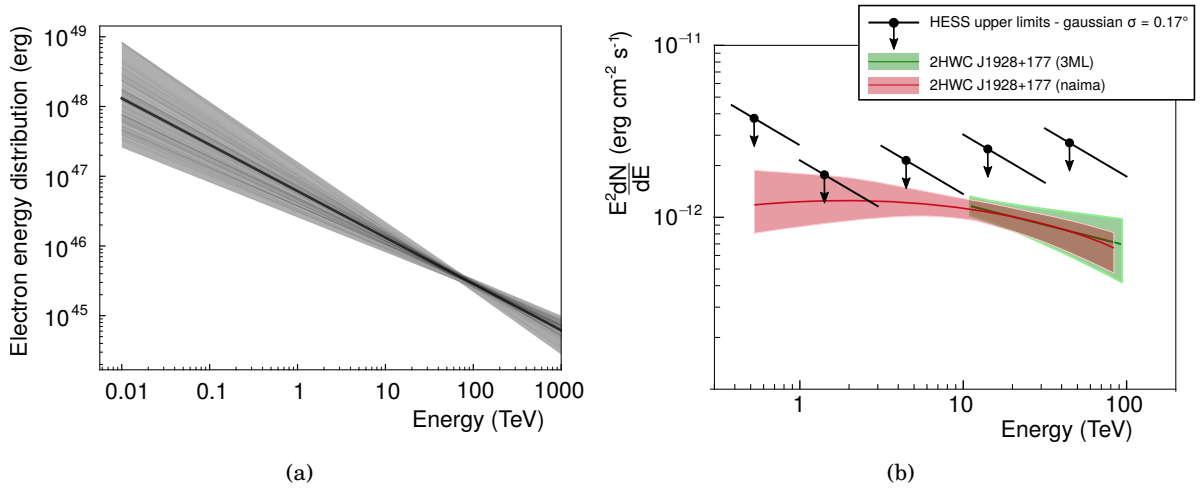

(a) (b)

Figure 5.13: (a) shows the spectrum of the electron population that would produce the observed γ-ray for 2HWC J1928+177. (b) shows the γ-ray spectrum of 2HWC J1928+177: the green spectrum comes from the best fit using 3ML. The red spectrum comes from the best fit with *naima*. The shaded regions represent the 1σ uncertainty. The upper limits derived by H.E.S.S. for a gaussian of σ = 0.17° in different energy bands are shown in black (credit: H.E.S.S. upper limits: Vincent Marandon, MPIK Heidelberg).

5.7.2 Association with a molecular cloud

Hypotheses for this association

The second possible hypotheses is that the TeV γ-ray source J1928 could be associated with a molecular cloud. Different candidates may contribute to the cosmic-ray population needed for this interaction. The following scenarios are considered:

1. The PWN associated with the pulsar PSR J1928+1746 produces electrons and positrons that could interact with the molecules of the cloud and produce γ rays via bremsstrahlung.

2. The atoms constituting the molecular cloud, mainly hydrogen, could be a target for relativistic protons, producing neutral pions during the interaction that emit the observed γ rays. The question is what could be the accelerator responsible for these cosmic rays ? The SNR associated with the pulsar PSR J1928+1746 would be a natural candidate but has not been detected at any wavelength. The fact that it is an old pulsar of 82 kyr could explain that the SNR is not visible anymore. Since it is so old, the SNR is unlikely to accelerate particles anymore. Several other hypothesis can be considered to explain the origin of the relativistic protons:

    - The ambient sea of cosmic rays: the interaction of the molecules of the clouds with the ambient cosmic rays filling the interstellar medium could simply be responsible for this emission. I will compare the cosmic-ray energy density of the cloud with the ambient cosmic ray density.
    - The pulsar PSR J1928+1746 and its PWN: they do not have counterpart in X-ray, which is unexpected for such a close pulsar of spin-down power $\dot{E} = 1.6.10^{36}$ erg s^{-1}. I will compare the energy radiated by the pulsar with the energy needed to produce the observed γ-ray luminosity.
    - Some unknown local accelerator: for example a nearby SNR, not detected yet. I will estimate the distance of such accelerator to the cloud in that scenario.

CO as a tracer for molecular clouds

As described in section 4.3, the main component of molecular clouds is molecular hydrogen H_2, followed by carbon monoxide CO. However, H_2 is almost impossible to observe directly, in contrast with CO, which is the most easily observed molecular line, found in all molecular clouds. The isotopes commonly used are ^{12}CO and ^{13}CO, the first one being optically thick while the second one is optically thin. Hence, ^{13}CO can probe deeper in the cloud without saturating, and provides more accurate velocity and kinematic distances because of the narrower line. Therefore, ^{13}CO is more suited to derive the column density of the cloud, under the hypothesis of local thermodynamic equilibrium. It is both a good quantitative and qualitative tracer of molecular

gas, being related to the column density of H_2. The emission line corresponding to the CO de-excitation gives the mean velocity of the CO molecules in the cloud and the width of this line gives the velocity dispersion associated with the cloud. Under the Virial equilibrium hypotheses, and assuming uniform density within the cloud, the width of the line scales linearly with the size of the cloud.

I use the ^{13}CO (rotation emission line J=1→0 at 110 GHz) data from the Galactic Ring Survey (GRS[2]) [56] obtained using the SEQUOIA multi pixel array on the Five College Radio Astronomy Observatory (FCRAO) 14 m telescope located in New Salem, Massachusetts, between December 1998 and March 2005. Three molecular clouds can be found at the location of the HAWC TeV emission. Figure 5.14(a) shows the HAWC significance map, where I define a region corresponding to the 5σ emission. From this region is extracted the velocity distribution as a function of the brightness temperature averaged over this region, visible in Figure 5.14(b). Three maxima can be highlighted at ~ 4.5 km s^{-1}, ~ 22 km s^{-1} and ~ 46 km s^{-1}. The ^{13}CO maps corresponding to each velocity are also displayed in Figure 5.14(c). I study in more details the more intense one, at ~ 22 km s^{-1}. Note that it seems to be the one that accounts for most of the emission seen in the velocity integrated ^{12}CO map, shown earlier on the middle panel of Figure 5.3.

Detailed study of the brightest cloud

The cloud at ~ 22 km s^{-1} has a very complicated and elongated shape. I restrain the study to the portion of the cloud within the 5σ γ-ray emission of 2HWC J1928+177, represented by the big green box in Figures 5.14 and 5.15. In this region, I decompose the cloud into two parts that could be interpreted as 2 clumps of the cloud. They are represented by the two smaller green boxes labeled 1 and 2 in Figure 5.15. The ^{13}CO map for the peak velocity and the velocity distribution are also shown for both of them on the right hand side of the same figure. I can now derive some basic properties like the column density, the mass and the volume of these clumps, to estimate the total cosmic-ray energy and energy density that would be needed to explain the γ-ray emission observed.

To do so, I assume as a very simple approximation that they have a spherical shape. The most probable distance[3] for this cloud is D = 4 kpc [80], which would be compatible with the distance of the pulsar. With their angular size θ, their diameter d and volume V can be calculated using equation 5.3. The clumps 1 and 2 have a diameter of ~ 12 and ~ 18 pc respectively. They are smaller than the source representing J1928 which was found to contain 68% of the emission within $\simeq 38$ pc. For each clump, the ^{13}CO column density $N(^{13}\mathrm{CO})$ is determined using the brightness temperature T_{mb}, in K, and the FWHM of the velocity distribution peak Δv, in km s^{-1}, as explained in [83]:

$$N(^{13}\mathrm{CO}) = 8.75.10^{14} T_{mb} \Delta v \tag{5.9}$$

[2]GRS data available at : https://www.bu.edu/galacticring/new_data.html

[3]The distance is derived using http://bessel.vlbi-astrometry.org/bayesian with a prior P_{far} = 0.1

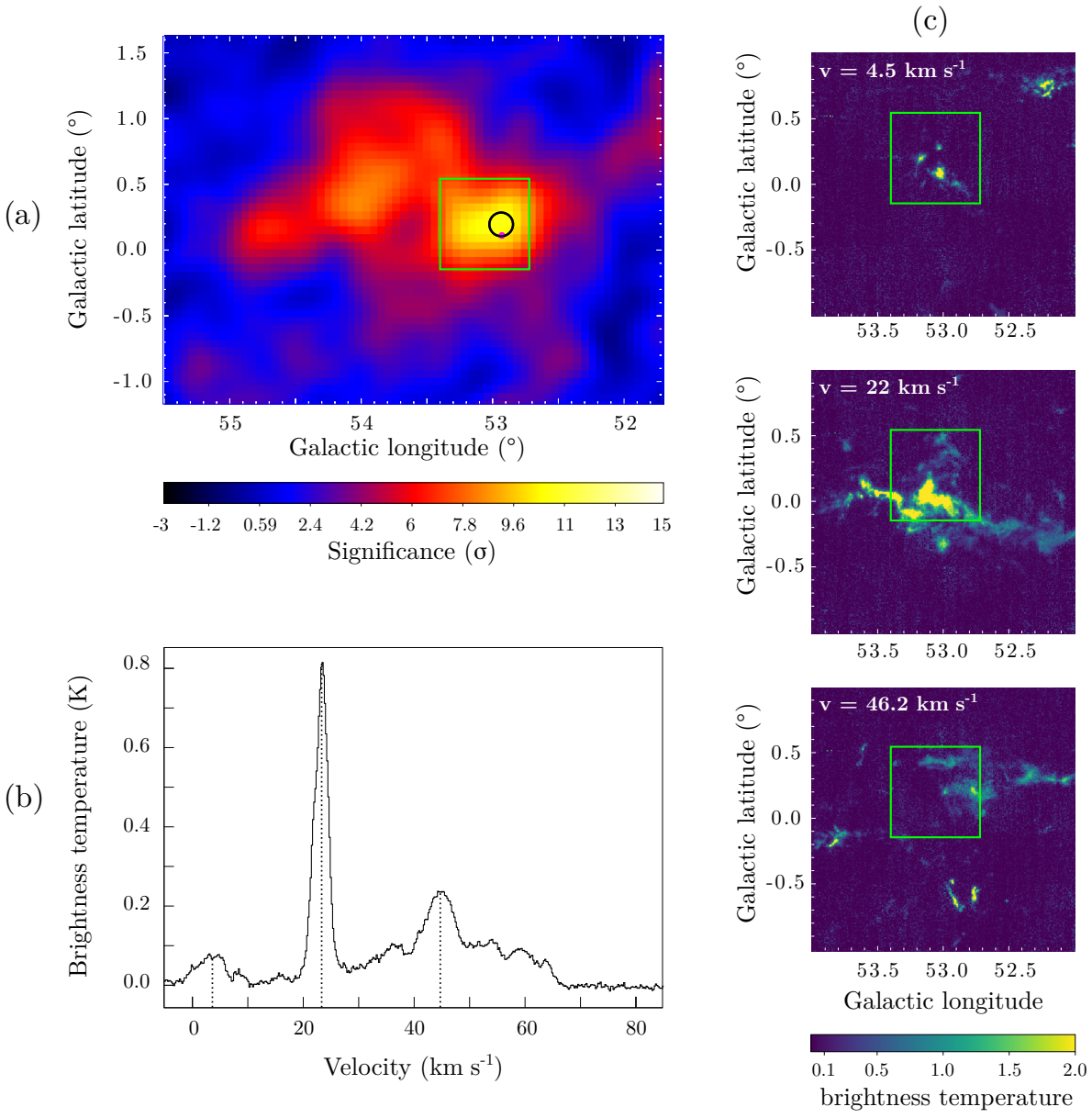

Figure 5.14: The HAWC significance map is shown in (a). The black circle is the location and 1σ uncertainty of the HAWC source. The magenta dot is the location of the pulsar. The green box is the region corresponding to the 5σ γ-ray emission of 2HWC J1928+177, where the velocity dispersion is averaged and plotted in (b) as a function of the brightness temperature. For the three peaks at ~ 4.5 km s^{-1}, ~ 22 km s^{-1} and ~46 km s^{-1}, the ^{13}CO map are shown in (c).

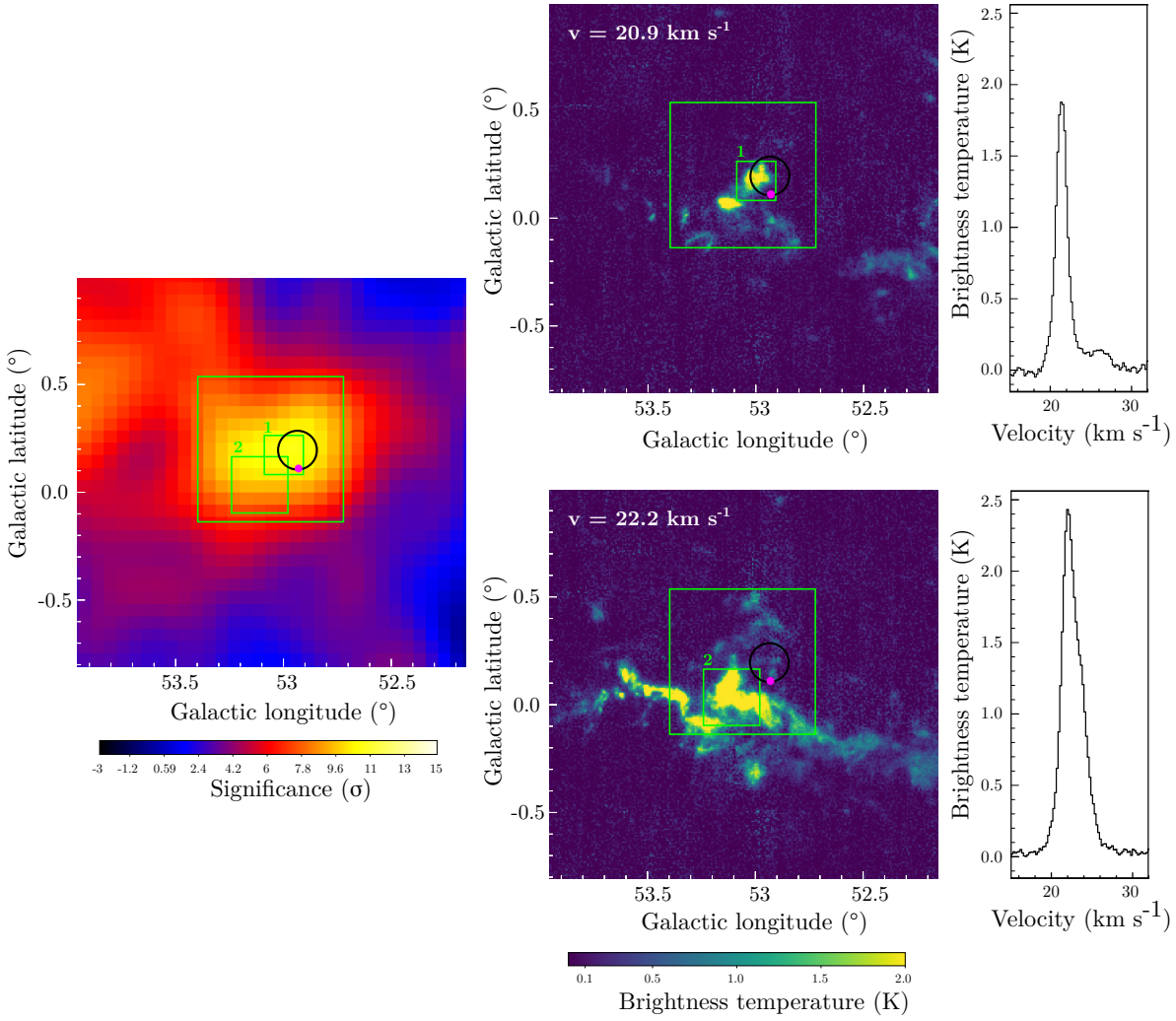

Figure 5.15: Molecular clouds at 22 km s^{-1} located within the 5σ γ-ray emission of 2HWC J1928+177. The black circle is the location and 1σ uncertainty of the HAWC source. The magenta dot is the location of the pulsar. The big green box is the region corresponding to the 5σ γ-ray emission of 2HWC J1928+177. The two smaller green boxes correspond to the two clumps considered here. The velocity map corresponding to each of them is shown on the right hand side, together with the velocity dispersion.

The clump mass M, in unit of solar masses, is given by:

$$M = 3.05.10^{-25} N(^{13}\mathrm{CO})\, \theta_x \theta_y D^2 \quad \mathrm{M}_\odot \tag{5.10}$$

where θ_x and θ_y are the half axes of the clump in arcseconds and D the distance to the cloud in pc, here assumed to be 4 kpc. Using the mass and the volume, the density of particles in the cloud, which are potential targets for cosmic rays, can be calculated using:

$$n = \frac{M}{\mu m_{\mathrm{H}} V} \tag{5.11}$$

where μm_{H} is the mean mass of an atom in the interstellar medium, with $\mu \simeq 1.4$ and m_{H} the mass of an hydrogen atom.

Moreover, using the best fit value for the flux found using 3ML, the luminosity L_γ above 1 TeV was calculated in the previous section using equation 5.2 to be $L_\gamma \simeq 1.10^{34}$ erg s^{-1}. Considering that at TeV energies the spectral energy distribution of the secondary γ rays peaks at about one tenth of the energy of the primary proton and does not vary significantly with the energy [52], a 1 TeV photon has been produced by a 10 TeV proton. The total energy of cosmic rays above 10 TeV in the cloud is similar to equation 5.7, $W_{\mathrm{p}} = \tau_{\mathrm{p}} L_\gamma$, where τ_{p} is now the characteristic cooling time for relativistic protons. It is derived using the proton-proton interaction cross section σ_{pp}, the speed of light c and the density n:

$$\tau_{\mathrm{p}} = \frac{1}{f \sigma_{\mathrm{pp}} c n} \tag{5.12}$$

In this relation, f stands for the fact that a proton looses about half of its energy per interaction, and only a third of it produces π^0. Hence, using typical values like $\sigma_{\mathrm{pp}} \simeq 35$ mb for very high energy protons [52] and $f = 1/6$ it results in a lifetime $\tau_{\mathrm{p}} \simeq 1.8.10^8 n^{-1}$ yr.
Finally, similarly to equation 5.8, the energy density is simply:

$$\epsilon_{\mathrm{p}} = \frac{W_{\mathrm{p}}}{V} = \frac{5.7.10^{15} L_\gamma \mu m_{\mathrm{H}}}{M} \tag{5.13}$$

For the cloud considered here, the total energy is then $W_{\mathrm{p}} = 1.1.10^{48}$ erg and the energy density $\epsilon_{\mathrm{p}} \simeq 6$ eV cm^{-3}. The different parameters calculated for each clump and for the total cloud are gathered in Table 5.7.

	clump 1	clump 2
angular size θ (°)	0.172	0.252
distance D (pc)	4000	4000
size d (pc)	12.0	17.6
volume V (pc^3)	906	2851
average brightness temperature T_{mb} (K)	1.875	2.44
FWHM of the velocity distribution peak Δv (km s^{-1})	1.5	2.56
column density $N(^{13}\mathrm{CO})$ (cm^{-3})	$2.46.10^{15}$	$5.47.10^{15}$
mass M ($\mathrm{M}_\odot$)	1151	5482
total energy W_p (erg)	$1.5.10^{48}$	$9.7.10^{47}$
energy density ϵ_p (eV cm^{-3})	34	7

	total cloud
mass M ($\mathrm{M}_\odot$)	6633
volume V (pc^3)	3757
density n (particles cm^{-3})	54
total energy W_p (erg)	$1.1.10^{48}$
energy density ϵ_p (eV cm^{-3})	6

Table 5.7: Summary of the properties of the CO cloud

Conclusions

From the study performed in this section we can conclude on the different hypotheses presented at the beginning of this section:

1. The interaction of electrons and positrons from the PWN with the molecules of the cloud producing γ-rays via bremsstrahlung.

Adding up the two clumps gives a mass for the cloud of $\sim 6600 M_\odot$, and a density of ~ 50 particles per cm^3. However, around 1 TeV γ-ray emission, IC scattering of electrons on the CMB dominates for medium densities lower than ~ 240 particles per cm^3 [52]. Hence bremsstrahlung does not play a significant role here : the observed emission cannot be explained by the electrons and positrons from the PWN interacting with the atoms of the cloud via bremsstrahlung.

2. The interaction of relativistic protons from the pulsar with the molecular cloud producing γ-rays via proton-proton interaction.

The total energy in cosmic rays in the cloud derived from the observed γ-ray luminosity is calculated to be $1.1.10^{48}$ erg, leading to an energy density of ~ 6 eV cm^{-3}. It is four orders of magnitude higher than the energy density of the sea of galactic cosmic rays above 10 TeV, which is $\sim 1.10^{-3}$ eV cm^{-3} [41]. Hence these cosmic rays cannot explain the TeV emission observed by HAWC by interacting with the cloud.

The furthest edge of clump 2 is 22 pc away from the pulsar. Considering a sphere of radius 22 pc centered on the pulsar, it contains both clumps. The volume of this sphere is 15 times the sum of the volume of both clumps together. Since the total energy in the cloud is $1.1.10^{48}$ erg, the energy in the sphere centered on the pulsar should be given by:

$$\frac{R^3}{r^3} = 15 = \frac{W_R}{1.1.10^{48}} \qquad \Rightarrow \qquad W_R = 1.7.10^{49}\text{erg} \tag{5.14}$$

Dividing by the spin-down power of the pulsar $\dot{E} = 1.6.10^{36}$ erg s^{-1} gives ~ 300 kyr, which is much higher than the age of the pulsar. Under this assumption, which assumes that all the energy of the pulsar goes to protons, the energy density provided by the pulsar is not enough to illuminate this cloud. However this calculation also assumed that the spin-down power $\dot{E}$ is constant over time, meaning that the pulsar released all his life time a constant amount of rotational energy E_{ROT}. Although this assumption may be reasonable as a first approximation, the real scenario is that the pulsar releases most of its energy at the beginning of its lifetime and decreases steadily its spin-down power afterwards, as described by equation 1.7. It has been argued that up to 20% of a pulsar energy could accelerate ions [30]. Assuming as a reasonable value that 10% of the pulsar energy was used to accelerate protons, it means that it must have released $10 \times W_R = 1.7.10^{50}$ erg. Considering that this is equal to the difference in rotational

energy between now and when the pulsar was born:

$$\Delta \mathrm{E} = 1.7.10^{50} = \frac{I}{2}(\Omega_0^2 - \Omega^2) \qquad \text{with} \qquad \Omega_0 = \frac{2\pi}{P_0} \quad \text{and} \quad \Omega = \frac{2\pi}{P} \tag{5.15}$$

The pulsar considered here has a period of $P = \sim 70$ ms. It gives a birth period of $P_0 = \sim 10$ ms. The maximum total energy that a pulsar with a birth period of 1 ms can release during its life is $\mathrm{E_{ROT}} = 1.10^{53}$ erg, for a pulsar with a typical mass of 1.4 $\mathrm{M_\odot}$ and a typical radius of 10 km [61]. Our result is consistent with this upper limit. Moreover, integrating equation 1.7 from birth ($t = 0$) until now ($t = T$) with the braking index $n = 3$ gives:

$$\Delta E = \dot{E}_0 \frac{T}{1 + \frac{T}{\tau_0}} = \dot{E} \left(1 + \frac{T}{\tau_0}\right) T \tag{5.16}$$

Using equation 1.4:

$$\tau_0 = \frac{\dot{E}\ \tau_c^2}{\Delta E + \dot{E}\tau_c} \tag{5.17}$$

With $\Delta E = 1.7.10^{50}$ erg, the spin-down of the pulsar $\dot{E} = 1.6.10^{36}$ erg $\mathrm{s^{-1}}$ and the characteristic age of the pulsar $\tau_c = 82600$ yr, the critical age at birth $\tau_0 = 1976$ year. Its true age would be 80624 yr. Finally its spin-down power at birth would be $\dot{E}_0 = 2.7.10^{39}$ erg $\mathrm{s^{-1}}$. It seems reasonable when comparing with the Crab for which $\dot{E}_0 \simeq 10^{39}$ erg $\mathrm{s^{-1}}$. To conclude, this would be a possible scenario.

Finally, the remaining hypotheses is that a local accelerator, for example an SNR, undetected yet, is producing the detected VHE γ-ray emission. It is commonly assumed that an SNR releases $\sim 10^{51}$ erg of kinetic energy in the interstellar medium, and 10% of it, that is $\sim 10^{50}$ erg, is used into cosmic-ray acceleration. Assuming a cosmic-ray spectrum between 1 GeV and 1 PeV with an energy dependence $\mathrm{E^{-2}}$, 33% of them have an energy above 10 TeV, that makes $\sim 3.3.10^{49}$ erg. Similarly to equation 5.14, the ratio of the volume around the SNR, filled with cosmic rays, and the volume of the cloud scales like the ratio of the energy contained in each volume :

$$\frac{D^3}{r^3} = \frac{3.3.10^{49}}{1.1.10^{48}} \simeq 30 \qquad \Rightarrow \qquad D = (30 r^3)^{1/3} \tag{5.18}$$

where $r = 10$ pc is approximately the radius of the cloud and D is the distance from the SNR to the further edge of the clump. Thus, an SNR located within a distance of ~ 30 pc from the cloud would be able to account for the cosmic rays producing the observed TeV emission by interaction with the molecules of the cloud.

5.8 Conclusion

This chapter gave a detailed description and a multiwavelength overview of this complex region of the galactic plane at longitude $52° < \ell < 55°$. One source, J1930, was already known, and

2 sources, J1928 reported in the HAWC catalogue and J1932 new in this study, are detected for the first time at TeV energies. I presented a multi-component fit using 3ML, assuming point-like sources, extended sources with symmetric gaussian shapes, and single power laws.

- J1930 is represented by a point-like source. The spectrum derived is in better agreement with the VERITAS spectrum.
- J1932, in agreement with H.E.S.S. upper limits, is represented by a point-like source. Its spectrum is described by a flux at 10 TeV of $1.9.10^{-15}$ TeV^{-1} cm^{-2} s^{-1} and a spectral index of -2.56
- J1928 is represented by an extended source of angular size $\sigma = 0.17°$ (39% containment). It has a hard spectrum with an index of -2.24, which would explain the emission visible in the highest energy HAWC map, and the fact that HAWC is more sensitive to detect it than H.E.S.S.. I studied different hypotheses for the possible origin of the observed γ-ray emission and concluded that 3 scenarios would be possible:

  1. electrons from the PWN who started to cool and diffuse away from it, producing γ rays via IC scattering on ambient photons
  2. cosmic ray protons produced by the pulsar interacting with a nearby molecular cloud and producing γ rays via proton-proton interaction
  3. another unknown accelerator, like a nearby SNR, located within $\sim$ 30 pc. However, no hint of such a SNR has been observed at any wavelength.

  More complex morphological and spectral analysis would need to be assumed to maybe help distinguishing the remaining scenarios. Going further would also require better energy and angular resolution. Energy estimator are being developed to make HAWC energy maps, which would allow to better study the energy dependency of the spectral and morphological parameters. A better angular resolution would permit to make profiles in different directions around the pulsar, in particular along the cloud location and perpendicular to it, to see any asymmetry in the γ-ray emission. Two other components were also found in the best fit of the region: an extended source of angular size $\sigma = 0.3°$ and a very large one of size $\sigma = 1.3°$. Deeper analysis would be required to determine if they can be related to the existing sources, come from other sources, or from the large scale γ-ray galactic emission for example.

CHAPTER 6

CONCLUSION

This thesis was dedicated to the very high energy γ-ray domain and to the associated ground based detection techniques. Produced by the interaction of relativistic charged particles with radiation field or matter, γ rays probe non thermal physics processes, the sources of these cosmic rays and their environment. Gamma rays are detected either directly from space with satellites or from the ground thanks to the air showers and their Cherenkov light emission. The focus of this thesis was placed on the galactic plane, very rich in γ-ray sources. A lot of data from different instruments are available in the γ-ray domain: all-sky data from the *Fermi*-LAT in the 10 MeV - 400 GeV energy range have been taken for 10 years. Data on dedicated regions have been taken over the past 15 years by IACTs in the 100 GeV - 10 TeV energy range. All-sky data have been taken by the HAWC observatory for 3 years in the TeV energy range.

One of the main aspects of this thesis was to reconcile data from two very different instruments: an IACT, H.E.S.S., and a WCD, HAWC. They have very different characteristics, very different operation philosophy and their reconstruction and analysis chains are adapted to each type of instrument. However, they have a part of the sky in common, they share part of their energy range and they can learn from each other and constrain each other. Their complementarity was deeply exploited in this thesis. HAWC and H.E.S.S. maps were constructed as comparable as possible, by smoothing their instrumental differences and applying the reconstruction and analysis method of one instrument to the other. This led to a presentation of the first fair comparison of such a large part of the sky, the galactic plane.

One major outcome of the galactic plane comparison was that in overall both instruments definitely see the same sky: both maps look very similar, and the same structures are found in

both of them. In particular, sources that were detected only by HAWC can be found in the new version of the H.E.S.S. map. One such source belonging to a very complex region was studied in details in this thesis, 2HWC J1928+177. A multi-component morphological and spectral fit was preformed to try to decompose the region into different components. The best fit model gave 5 components: one point-like component for the source 2HWC J1930+188, already well known from H.E.S.S. and VERITAS observations. Its spectrum is described by a single power law with a flux at 10 TeV of $3.7.10^{-15}$ TeV^{-1} cm^{-2} s^{-1} and a spectral index of -2.89. One point-like component for a new source HWC J1932+192. Its spectrum is described by a single power law with a flux at 10 TeV of $1.9.10^{-15}$ TeV^{-1} cm^{-2} s^{-1} and a spectral index of -2.56. One extended source of angular size $\sigma = 0.17°$ was found for our source of interest 2HWC J1928+177. Its spectrum is described by a single power law with a flux at 10 TeV of $4.4.10^{-15}$ TeV^{-1} cm^{-2} s^{-1} and a spectral index of -2.24. An exploration of the different hypotheses that could explain the observed γ-ray emission was performed. The standard scenario of electrons from the PWN interacting via IC scattering with the ambient radiation field is a plausible scenario. However, regarding the old age of the pulsar, these electrons would have started to cool down and to diffuse away from the PWN, which would explain the extended nature of this source. Another hypotheses was formulated because of the presence of a molecular cloud at a distance that could be consistent with the pulsar distance. Hence, the emission of γ rays by neutral pions produced by cosmic ray protons accelerated by the pulsar with protons of the cloud is also possible. Two extra extended components were also found: the first one of size $\sigma = 0.3°$ in the north of the region, and a very extended one of size $\sigma = 1.3°$ on top of the region that could account for large scale diffuse emission. For a deeper analysis of this very interesting region, energy dependent morphology studies could be performed. More complex morphological and spectral hypothesis could be tested, although it might not help in the case of the region as presented here which is already very complex. Finally, applying the same analysis on VERITAS data could be done to help in our understanding of the region.

In total, 8 potential new H.E.S.S. source candidates are visible along the whole galactic plane. Each of them would require more investigations in a future work such as looking for counterparts at other wavelengths, looking for energy dependency, or trying to model the corresponding regions.

From the instrument point of view, the deployment of the outrigger array around the HAWC observatory has been implemented to improve its performances at the highest energies, above 10 TeV. My contribution to this upgrade, and the other main part of this thesis, concerns the calibration of the charge and time reconstruction of the PMTs of the new array. The calibration method was explained and it was shown that the achieved performance is in agreement with most of the requirements. The outrigger array is now fully deployed and operational. The outriggers are calibrated, currently taking data and they are continuously monitored. Merging of the outrigger data with the main array data is also implemented. The next step is to use the core reconstruction method developed for the outriggers [58] for these merged events, and to develop a direction

reconstruction algorithm. More data from HAWC, which is continuously taking data, with the help of the outriggers and improved reconstruction methods can be used for future work.

On longer time scale, the next generation of instruments is already under preparation: CTA, the next generation of IACTs is being developed [35] and the first telescope prototype of this array of IACTs is under commissioning. On the WCD side, a wide field of view γ-ray observatory in the southern hemisphere is under design [20]. Both instruments will have a complementary sky coverage, complementary energy range, a better sensitivity and resolution than any such instruments before.

BIBLIOGRAPHY

[1] ABBOTT, B. P. *et al.* – *Multi-messenger Observations of a Binary Neutron Star Merger*, The Astrophysical Journal Letters **848** (2017), p. L12.

[2] ABDO, A. A. *et al.* – *Fermi Large Area Telescope First Source Catalog*, The Astrophysical Journal Supplement **188** (2010), p. 405–436.

[3] ABDO, A. A. *et al.* – *Fermi Large Area Telescope Measurements of the Diffuse Gamma-Ray Emission at Intermediate Galactic Latitudes*, Physical Review Letters **103** (2009), no. 25, p. 251101.

[4] ABEYSEKARA, A. U. *et al.* – *Daily Monitoring of TeV Gamma-Ray Emission from Mrk 421, Mrk 501, and the Crab Nebula with HAWC*, The Astrophysical Journal **841** (2017), p. 100.

[5] ABEYSEKARA, A. U. *et al.* – *Extended gamma-ray sources around pulsars constrain the origin of the positron flux at Earth*, Science **358** (2017), p. 911–914.

[6] ABEYSEKARA, A. U. *et al.* – *Very-high-energy particle acceleration powered by the jets of the microquasar SS 433*, Nature **562** (2018), p. 82–85.

[7] ABEYSEKARA, A. U. *et al.* – *The 2HWC HAWC Observatory Gamma-Ray Catalog*, The Astrophysical Journal **843** (2017), p. 40.

[8] ABEYSEKARA, A. U. *et al.* – *Observation of the Crab Nebula with the HAWC Gamma-Ray Observatory*, The Astrophysical Journal **843** (2017), p. 39.

[9] ABEYSEKARA, A. U. *et al.* – *Search for Very High-energy Gamma Rays from the Northern Fermi Bubble Region with HAWC*, The Astrophysical Journal **842** (2017), p. 85.

[10] ABEYSEKARA, A. U. *et al.* – *The HAWC Real-time Flare Monitor for Rapid Detection of Transient Events*, The Astrophysical Journal **843** (2017), p. 116.

[11] ABEYSEKARA, A. U. *et al.* – *VERITAS and Fermi-LAT Observations of TeV Gamma-Ray Sources Discovered by HAWC in the 2HWC Catalog*, The Astrophysical Journal **866** (2018), p. 24.

[12] ABRAMOWSKI, A. *et al.* – *Discovery of extended VHE γ-ray emission from the vicinity of the young massive stellar cluster Westerlund 1*, Astronomy and Astrophysics **537** (2012), p. A114.

[13] ABRAMOWSKI, A. *et al.* – *Diffuse Galactic gamma-ray emission with H.E.S.S.*, Physical Review D: Particles, Fields, Gravitation and Cosmology **90** (2014), no. 12, p. 122007.

[14] ACCIARI, V. A. *et al.* – *Discovery of Very High Energy γ-ray Emission from the SNR G54.1+0.3*, The Astrophysical Journal Letters **719** (2010), p. L69–L73.

[15] ACKERMANN, M. *et al.* – *VizieR Online Data Catalog: The second Fermi-LAT > 50GeV catalog (2FHL)*, VizieR Online Data Catalog **222** (2016).

[16] AHARONIAN, F. *et al.* – *Calibration of cameras of the H.E.S.S. detector*, Astroparticle Physics **22** (2004), p. 109–125.

[17] AHARONIAN, F. *et al.* – *Observations of the Crab nebula with HESS*, Astronomy and Astrophysics **457** (2006), p. 899–915.

[18] ALBERT, A. *et al.* – *Dark Matter Limits from Dwarf Spheroidal Galaxies with the HAWC Gamma-Ray Observatory*, The Astrophysical Journal **853** (2018), p. 154.

[19] ALBERT, A. *et al.* – *Search for dark matter gamma-ray emission from the Andromeda Galaxy with the High-Altitude Water Cherenkov Observatory*, Journal of Cosmology and Astroparticle Physics **6** (2018), p. 043.

[20] ALBERT, A. *et al.* – *Science Case for a Wide Field-of-View Very-High-Energy Gamma-Ray Observatory in the Southern Hemisphere*, arXiv e-prints (2019).

[21] ALEKSIĆ, J. *et al.* – *Measurement of the Crab Nebula spectrum over three decades in energy with the MAGIC telescopes*, Journal of High Energy Astrophysics **5** (2015), p. 30–38.

[22] ALFARO, R. *et al.* – *Search for Very-high-energy Emission from Gamma-Ray Bursts Using the First 18 Months of Data from the HAWC Gamma-Ray Observatory*, The Astrophysical Journal **843** (2017), p. 88.

[23] BERGE, D., FUNK, S. AND HINTON, J. – *Background modelling in very-high-energy γ-ray astronomy*, Astronomy and Astrophysics **466** (2007), p. 1219–1229.

[24] BIGNAMI, G. F. *et al.* – *The COS-B experiment for gamma-ray astronomy*, Space Science Instrumentation **1** (1975), p. 245–268.

[25] BLOEMEN, H. – *Diffuse Galactic gamma-ray emission*, Annual Review of Astronomy and Astrophysics **27** (1989), p. 469–516.

[26] BOCCHINO, F., BANDIERA, R. AND GELFAND, J. – *XMM-Newton and SUZAKU detection of an X-ray emitting shell around the pulsar wind nebula G54.1+0.3*, Astronomy and Astrophysics **520** (2010), p. A71.

[27] BOLMONT, J. *et al.* – *The camera of the fifth H.E.S.S. telescope. Part I: System description*, Nuclear Instruments and Methods in Physics Research A **761** (2014), p. 46–57.

[28] BOTHE, W. AND KOHLÖRSTER, W. – *Das Wesen der Höhemstahlung (The nature of cosmic radiation)*, Zeitschrift für Physik **56** (1929), p. 751–777.

[29] BRINKMANN, W., ASCHENBACH, B. AND KAWAI, N. – *ROSAT observations of the W 50/SS 433 system.*, Astronomy and Astrophysics **312** (1996), p. 306–316.

[30] BUCCIANTINI, N., ARONS, J. AND AMATO, E. – *Modelling spectral evolution of pulsar wind nebulae inside supernova remnants*, Monthly Notices of the Royal Astronomical Society **410** (2011), p. 381–398.

[31] CAMILO, F. *et al.* – *Discovery of a 136 Millisecond Radio and X-Ray Pulsar in Supernova Remnant G54.1+0.3*, The Astrophysical Journal Letters **574** (2002), p. L71–L74.

[32] CASE, G. AND BHATTACHARYA, D. – *On the Nature of the Discrete Gamma-Ray Sources in the Vicinity of the Supernova Remnant G312.4-0.4*, The Astrophysical Journal **521** (1999), p. 246–254.

[33] CAWLEY, M. F. *et al.* – *Application of imaging to the atmospheric Cherenkov technique*, International Cosmic Ray Conference **3** (1985).

[34] CHANDRASEKHAR, S. – *The Maximum Mass of Ideal White Dwarfs*, The Astrophysical Journal **74** (1931), p. 81.

[35] CHERENKOV TELESCOPE ARRAY CONSORTIUM *et al.* – *Science with the Cherenkov Telescope Array*, 2019.

[36] COMPTON, A. H. – *Nature of Cosmic Rays*, Nature **131** (1933), p. 713–715.

[37] CORDES, J. M. *et al.* – *Arecibo Pulsar Survey Using ALFA. I. Survey Strategy and First Discoveries*, The Astronomical Journal **637** (2006), p. 446–455.

[38] DAME, T. M., HARTMANN, D. AND THADDEUS, P. – *The Milky Way in Molecular Clouds: A New Complete CO Survey*, The Astrophysical Journal **547** (2001), p. 792–813.

[39] DERDEYN, S. M. *et al.* – *SAS-B digitized spark chamber gamma ray telescope.*, Nuclear Instruments and Methods **98** (1972), p. 557–566.

[40] FICHTEL, C. – *EGRET overview: Achievements in the light of expectations.*, Astronomy and Astrophysics Supplement **120** (1996), p. 23–29.

[41] GABICI, S., AHARONIAN, F. A. AND CASANOVA, S. – *Broad-band non-thermal emission from molecular clouds illuminated by cosmic rays from nearby supernova remnants*, Monthly Notices of the Royal Astronomical Society **396** (2009), p. 1629–1639.

[42] GAENSLER, B. M. AND SLANE, P. O. – *The Evolution and Structure of Pulsar Wind Nebulae*, Annual Review of Astronomy and Astrophysics **44** (2006), p. 17–47.

[43] GALBARAITH, W. AND JELLEY, J. V. – *Light pulses from the night sky associated with cosmic rays*, Nature **171** (1953), p. 349–350.

[44] GALBRAITH, W. AND JELLEY, J. V. – *Light Pulses from the Night Sky associated with Cosmic Rays*, Nature **171** (1953), p. 349–350.

[45] GÓRSKI, K. M. *et al.* – *HEALPix: A Framework for High-Resolution Discretization and Fast Analysis of Data Distributed on the Sphere*, The Astrophysical Journal **622** (2005), p. 759–771.

[46] GREEN, D. A. – *VizieR Online Data Catalog: A catalogue of Galactic supernova remnants (Green, 2014)*, VizieR Online Data Catalog **7272** (2014).

[47] H. E. S. S. COLLABORATION *et al.* – *The H.E.S.S. Galactic plane survey*, Astronomy and Astrophysics **612** (2018), p. A1.

[48] HAHN, J. *et al.* – *Impact of aerosols and adverse atmospheric conditions on the data quality for spectral analysis of the H.E.S.S. telescopes*, Astroparticle Physics **54** (2014), p. 25–32.

[49] HEGER, A. *et al.* – *How Massive Single Stars End Their Life*, The Astrophysical Journal **591** (2003), p. 288–300.

[50] HESS, V. – *Beobachtung der durchdringenden Strahlung bei Sieben Freiballonfahrten (Observation in the low level radiation during seven free balloon flights)*, Physikalische Zeitschrift **13** (1912), p. 1084–1091.

[51] HILLAS, A. M. – *Cerenkov light images of EAS produced by primary gamma*, International Cosmic Ray Conference **3** (1985).

[52] HINTON, J. A. AND HOFMANN, W. – *Teraelectronvolt Astronomy*, Annual Review of Astronomy and Astrophysics **47** (2009), p. 523–565.

[53] HOFFMAN, C. M. *et al.* – *Gamma-ray astronomy at high energies*, Reviews of Modern Physics **71** (1999), p. 897–936.

[54] HUNTER, S. D. *et al.* – *EGRET Observations of the Diffuse Gamma-Ray Emission from the Galactic Plane*, The Astrophysical Journal **481** (1997), p. 205–240.

[55] ICECUBE COLLABORATION *et al.* – *Multimessenger observations of a flaring blazar coincident with high-energy neutrino IceCube-170922A*, Science **361** (2018).

[56] JACKSON, J. M. *et al.* – *The Boston University-Five College Radio Astronomy Observatory Galactic Ring Survey*, The Astronomical Journal Suplement **163** (2006), p. 145–159.

[57] JOSHI, V., JARDIN-BLICQ, A. AND HAWC COLLABORATION – *HAWC High Energy Upgrade with a Sparse Outrigger Array*, International Cosmic Ray Conference **35** (2017), p. 806.

[58] JOSHI, V. – *Reconstruction and analysis of highest energy gamma-rays and its application to pulsar wind nebulae*, Thèse, Heidelberg, 2019.

[59] JUNKES, N., FUERST, E. AND REICH, W. – *G54.4-0.3: CO shell and star formation region surrounding a shell-type supernova remnant. I - Properties of the CO shell*, Astronomy and Astrophysics, Supplement **96** (1992), p. 1–21.

[60] KARPOVA, A. *et al.* – *Observations of the γ-ray pulsar J1932+1916 in X-rays*, Monthly Notices of the Royal Astronomical Society **466** (2017), p. 1757–1763.

[61] KHANGULYAN, D. *et al.* – *On the Anomalously Large Extension of the Pulsar Wind Nebula HESS J1825-137*, The Astrophysical Journal **860** (2018), p. 59.

[62] KOO, B.-C. *et al.* – *A Massive-Star-forming Infrared Loop around the Crab-like Supernova Remnant G54.1+0.3: Post-Main-Sequence Triggered Star Formation?*, The Astronomical Journal Letters **673** (2008), p. L147.

[63] LATTIMER, J. M. AND PRAKASH, M. – *The Physics of Neutron Stars*, Science **304** (2004), p. 536–542.

[64] LEAHY, D. A., TIAN, W. AND WANG, Q. D. – *Distance Determination to the Crab-Like Pulsar Wind Nebula G54.1+0.3 and the Search for its Supernova Remnant Shell*, The Astronomical Journal **136** (2008), p. 1477–1481.

[65] LEE, J.-W., KOO, B.-C. AND LEE, J.-E. – *CO J=2-1 Line Observations Toward the Supernova Remnant G54.1+0.3*, Journal of Korean Astronomical Society **45** (2012), p. 117–125.

[66] LI, T.-P. AND MA, Y.-Q. – *Analysis methods for results in gamma-ray astronomy*, The Astrophysical Journal **272** (1983), p. 317–324.

[67] LUCAS, R. AND LISZT, H. – *Interstellar isotope ratios from mm-wave molecular absorption spectra*, Astronomy and Astrophysics **337** (1998), p. 246–252.

[68] LÓPEZ-COTO, R. *et al.* – *Morphological and spectral measurements of 2HWC J1928+177 with HAWC and H.E.S.S.*, Proceedings of the 35th ICRC, Busan, Korea (2017).

[69] MANCHESTER, R. N. *et al.* – *VizieR Online Data Catalog: ATNF Pulsar Catalogue (Manchester+, 2005)*, VizieR Online Data Catalog **1** (2016).

[70] MILLIKAN, R. A. – *High frequency rays of cosmic origins*, Nature **116** (1925), p. 823–825.

[71] MORRISON, P. – *On Gamma-Ray Astronomy*, il Nuovo Cimento **7** (1958), p. 858–865.

[72] PARSONS, R. D. AND HINTON, J. A. – *A Monte Carlo template based analysis for air-Cherenkov arrays*, Astroparticle Physics **56** (2014), p. 26–34.

[73] PETRY, D. *et al.* – *Detection of VHE γ-rays from MKN 421 with the HEGRA Cherenkov Telescopes.*, Astronomy and Astrophysics **311** (1996), p. L13–L16.

[74] PITTORI, C. *et al.* – *First AGILE catalog of high-confidence gamma-ray sources*, Astronomy and Astrophysics **506** (2009), p. 1563–1574.

[75] PLANCK COLLABORATION *et al.* – *Planck 2015 results. I. Overview of products and scientific results*, Astronomy and Astrophysics **594** (2016), p. A1.

[76] PLETSCH, H. J. *et al.* – *Einstein@Home Discovery of Four Young Gamma-Ray Pulsars in Fermi LAT Data*, The Astronomical Journal Letters **779** (2013), p. L11.

[77] PUEHLHOFER, G. *et al.* – *FlashCam: a fully-digital camera for the medium-sized telescopes of the Cherenkov Telescope Array*, in *34th International Cosmic Ray Conference (ICRC2015)*, International Cosmic Ray Conference, vol. 34, 2015, p. 1039.

[78] PUNCH, M. *et al.* – *Detection of TeV photons from the active galaxy Markarian 421*, Nature **358** (1992), p. 477.

[79] PUNCH, M. AND H.E.S.S. COLLABORATION – *The HESS project camera, tests, and status*, International Cosmic Ray Conference **7** (2001), p. 2814.

[80] REID, M. J. *et al.* – *A Parallax-based Distance Estimator for Spiral Arm Sources*, The Astronomical Journal **823** (2016), p. 77.

[81] SANDOVAL, A. – *HAWC Upgrade with a Sparse Outrigger Array*, arXiv e-prints (2015).

[82] IMAGING SENSORS, P. – *Photomultiplier tubes - principles and applications*, Photonis imaging sensors, 2002.

[83] SIMON, R. *et al.* – *The Structure of Four Molecular Cloud Complexes in the BU-FCRAO Milky Way Galactic Ring Survey*, The Astronomical Journal **551** (2001), p. 747–763.

[84] SMITH, A. J. – *A Survey of Fermi Catalog Sources using data from the Milagro Gamma-Ray Observatory*, ArXiv e-prints (2010).

[85] SMITH, S. W. – *Scientist and engineer's guide to digital signal processing*, California Technical Publishing, 1997.

[86] SWANENBURG, B. N. *et al.* – *Second COS B catalog of high-energy gamma-ray sources*, The Astrophysical Journal Letters **243** (1981), p. L69–L73.

[87] TANIMORI, T. *et al.* – *Detection of Gamma Rays of up to 50 TeV from the Crab Nebula*, The Astrophysical Journal Letters **492** (1998), p. L33–L36.

[88] TEMIM, T. *et al.* – *Deep Chandra Observations of the Crab-like Pulsar Wind Nebula G54.1+0.3 and Spitzer Spectroscopy of the Associated Infrared Shell*, The Astronomical Journal **710** (2010), p. 309–324.

[89] THOMPSON, D. J. *et al.* – *The Second EGRET Catalog of High-Energy Gamma-Ray Sources*, The Astrophysical Journal Supplement **101** (1995), p. 259.

[90] VACANTI, G. *et al.* – *Gamma-ray observations of the Crab Nebula at TeV energies*, The Astrophysical Journal **377** (1991), p. 467–479.

[91] VALLÉE, J. P. – *Catalog of Observed Tangents to the Spiral Arms in the Milky Way Galaxy*, The Astronomical Journal Suplement **215** (2014), p. 1.

[92] VANDENBROUCKE, J. AND FERMI LAT COLLABORATION – *Physics and astrophysics with gamma-ray telescopes*, Nuclear Physics B Proceedings Supplements **229** (2012), p. 258–264.

[93] VIANELLO, G. *et al.* – *The Multi-Mission Maximum Likelihood framework (3ML)*, Proceedings of the 34th ICRC, The Hague, Netherlands (2015).

[94] WAKELY, S. AND HORAN, D. – *TeVCat version 3*, (2010).

[95] WATSON, M. G. *et al.* – *The XMM-Newton serendipitous survey. V. The Second XMM-Newton serendipitous source catalogue*, Astronomy and Astrophysics **493** (2009), p. 339–373.

[96] WAYTH, R. B. *et al.* – *GLEAM: The GaLactic and Extragalactic All-Sky MWA Survey*, Publications of the Astronomical Society of Australia **32** (2015), p. e025.

[97] WEEKES, T. C. – *Very high energy gamma-ray astronomy.*, Physics Reports **160** (1988), p. 1–121.

[98] WEEKES, T. C. *et al.* – *Observation of TeV gamma rays from the Crab nebula using the atmospheric Cerenkov imaging technique*, The Astrophysical Journal **342** (1989), p. 379–395.

[99] WIELEBINSKI, R. – *The Characteristics of (Normal) Pulsars*, in *Neutron Stars, Pulsars, and Supernova Remnants* (Becker, W., Lesch, H. and Trümper, J., éds.), 2002, p. 167.

[100] WULF, T. – *Über die in der Atmosphäre vorhandene Strahlung von hoher Durchdringungsfähigkeit (On the radiation of high penetrating power that exist in the atmosphere)*, Physikalische Zeitschrift **11** (1909), p. 152–157.

[101] ZABALZA, V. – *Naima: a Python package for inference of particle distribution properties from nonthermal spectra*, in *34th International Cosmic Ray Conference* (Borisov, A. S. *et al.*, éds.), International Cosmic Ray Conference, vol. 34, 2015, p. 922.